A Measurement of the Diffractive Reduced Cross-Section $\sigma_r^{D(3)}$ at Low Q^2 in Deep Inelastic Scattering with the H1 Detector

Yves Coppens

A thesis submitted to

The University of Birmingham

for the degree of

DOCTOR OF PHILOSOPHY

School of Physics and Astronomy
University of Birmingham
September 2004

Abstract

A new high precision measurement of the diffractive deep inelastic scattering process $ep \rightarrow eXY$ is presented, where Y is a proton or a low mass excitation and X represents the dissociation products of the photon coupled to the electron. The results are obtained from a dedicated data sample of 2.68 pb^{-1}, taken by the H1 experiment at HERA, with unbiased triggers. The measurement is presented in the form of a 3-dimensional reduced cross-section $\sigma_r^{D(3)}(\beta, Q^2, x_{I\!\!P})$ which is integrated over the region $M_Y < 1.6$ GeV and $|t| < 1$ GeV^2. The kinematic range covered is $1.5 < Q^2 < 45$ GeV^2 and $0.01 < y < 1$. Through the use of the Backward Silicon Tracker in the electron identification and vertex determination, this analysis considerably extends the kinematic coverage at low Q^2 and low y compared with previous published and preliminary measurements by H1. The low values of y attained result in unprecedented high statistics at high $x_{I\!\!P}$ ($x_{I\!\!P} \lesssim 0.03$). Good agreement is generally observed in the region of overlap with a previous H1 measurement. In most of the phase space for $Q^2 > 3.5$ GeV^2, the data are well described by predictions derived from a fit to higher Q^2 data based on QCD hard scattering factorisation for semi-inclusive processes and the DGLAP evolution equations. The measurement thus confirms the dominance of a gluon distribution extending to large fractional momenta in the diffractive exchange. The data presented in this thesis are expected to greatly help to provide more accurate diffractive parton distribution functions and to identify areas where the diffractive factorisation approach fails.

Acknowledgments

A Note on Units

In this work, a system of natural units will be used, whereby $\hbar = c = 1$.

Contents

List of Figures

List of Tables

Introduction

The first Deep Inelastic Scattering (DIS) experiments were performed at SLAC [1,2] where high energy electrons were collided with fixed nuclear targets. The reaction proceeded via the exchange of a photon between the electron and the target proton or nucleus, and a final state system of hadrons was produced. The measured cross-section exhibited only a weak dependence on the squared four-momentum transfer carried by the photon. This behaviour, known as scaling, was interpreted as being evidence for the scattering of the electron from point-like particles or partons, later identified with the quarks and gluons of the Standard Model, in the proton. The latest electron-proton scattering experiments have been performed at the Hadron Electron Ring Accelerator (HERA) located at the DESY laboratory in Hamburg. Many precise measurements at HERA have confirmed the theory of Quantum Chromodynamics (QCD), the component of the Standard Model describing the strong interaction, which has emerged since the first SLAC experiments. The HERA data also provide the best constraints on the proton quark and gluon densities over a wide range of momentum transfer fractions.

A class of abundant DIS events at HERA is characterised by a large rapidity gap adjacent to the proton direction in which no hadrons emerge. These events have generated considerable interest because they are not yet fully understood within the theory of the strong interaction. They are described as being 'diffractive' and must involve a colour singlet exchange, also known as a 'pomeron'. In the most commonly used theoretical approach, a partonic structure is ascribed to the diffractive exchange, and the the photon is viewed as

probing the structure of the pomeron rather than that of the proton. The measurement of this thesis, performed with the H1 detector at HERA, helps to understand better the partonic structure and the dynamics of the diffractive exchange in a crucial region of phase space for new tests of our understanding within QCD.

Chapter 1 introduces the ingredients of the physics of deep inelastic scattering which are needed for the discussion of diffractive DIS that follows in chapter 2. Chapter 3 contains a brief description of the HERA accelerator, and a more detailed description of the H1 detector, focusing on the sub-detectors used in the analysis presented here. Chapter 4 deals with the event selection. Since diffractive DIS events form a subset of DIS events, the inclusive DIS sample provides a valuable control sample, and so a lot of attention is paid to the selection and the good understanding of this sample of events. The emphasis is put on the discussion of the new method, using the H1 Backward Silicon Tracker, employed for the measurement of the electron and the determination of the event vertex, and the alignment of the various electron detectors. The selection of diffractive events, based on the presence of a large rapidity gap in the event identified using the forward components of the H1 detector, is then presented. The chapter concludes with the demonstration of the good understanding of the diffractive sample. In chapter 5, the procedure used to measure the diffractive reduced cross-section is explained. The stability of the cross-section measurement is also investigated by performing the measurement using another method for the kinematic reconstruction and another Monte Carlo generator. The results of the analysis are presented in chapter 6. The new data considerably expand the phase space covered by inclusive diffraction measurements. The data are discussed and compared with existing H1 results in the region where the data sets overlap. The prediction of a next-to-leading order QCD fit to previous higher Q^2 data, using the DGLAP formalism, is also compared with the data.

Chapter 1

Deep Inelastic Scattering

1.1 Introduction

Electron-proton interactions are mediated by electroweak gauge bosons γ, Z^0 and $W^{\pm}$. Neutral current and charged current processes are distinguished by the presence in their final state of an electron or a neutrino respectively. The former process proceeds via the exchange of γ or Z^0 vector bosons and the latter via the exchange of a W^+ or W^- bosons.

These processes are illustrated in figure 1.1 (a) where X represents the hadronic final state. The 4-momentum squared carried by the exchanged boson is denoted by q^2. It is convenient to introduce the positive quantity:

$$Q^2 \equiv -q^2, \tag{1.1}$$

which is the virtuality of the exchanged boson. When Q^2 is much smaller than the square of the masses of the Z^0 and $W^{\pm}$ [1], the electromagnetic current contribution dominates the DIS cross-section (see section 1.3).

---

[1]The mass of the Z^0 is 91.1882± 0.007 GeV and the mass of W boson is 80.448 ± 0.031 GeV [3].

In DIS, virtual photons couple to single charged partons inside the proton. Finer details of the proton are probed with increasing virtualities. In the photoproduction regime, the electron emits a quasi-real photon with Q^2 much smaller than the proton mass [2] squared, m_p^2. In this region of phase space, the wavelength of the photon is too large to resolve the internal structure of the proton.
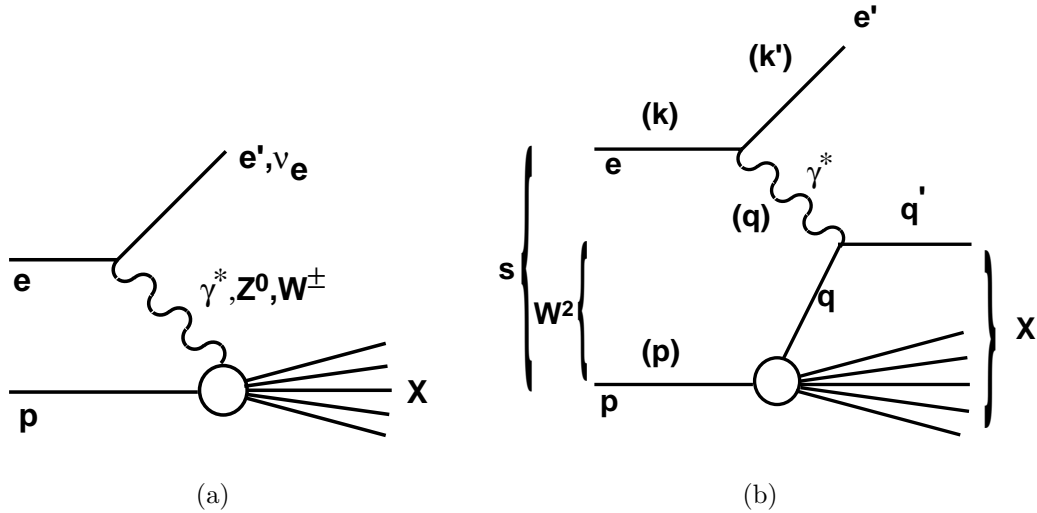
Figure 1.1: (a) Illustration of NC and CC deep-inelastic scattering processes and (b) the kinematics of NC DIS.

1.2 HERA Kinematics

The kinematics of ep processes are described using a combination of the 4-vectors of the proton, the electron, and the photon denoted by p, k and q respectively. They are shown in figure 1.1 (b). The centre of mass energy squared of the ep system, s, is given by:

$$s = (p + k)^2 \simeq 4E_p E_e, \tag{1.2}$$

where E_e and E_p are the electron and proton beam energies, respectively. For the beam energies used in this analysis, s is approximately 320 GeV. The dimensionless Bjorken

---

[2]The mass of the proton is 0.938 GeV [3].

4

scaling variable,

$$x = \frac{Q^2}{2p.q},$$ (1.3)

is interpreted as the fraction of the proton momentum carried by the struck quark in the infinite momentum frame of the proton. There is a second Bjorken scaling variable defined by:

$$y = \frac{p.q}{p.k},$$ (1.4)

which is the fraction of the electron energy taken by the exchanged photon in the proton rest frame. The square of the invariant mass of the hadronic final state X, which is equivalent to the squared mass of the photon-proton system, is given by

$$W^2 = (q + p)^2.$$ (1.5)

In the limit where the masses of the incoming particles can be neglected, the kinematic variables are related by:

$$Q^2 = sxy$$ (1.6)

and

$$W^2 = ys - Q^2,$$ (1.7)

such that only two of the five quantities defined in equations 1.1-1.5 are independent once s is fixed.

1.3 DIS Cross-Sections

The total neutral current DIS cross-section is expressed as the sum of the contributions from virtual photon (γ^*) and Z^0 exchanges and from their interference:

$$\sigma_{NC} = \sigma(\gamma^*) + \sigma(Z^0) + \sigma(\gamma^* Z^0). \tag{1.8}$$

The relative Q^2 dependences of the different terms entering equation 1.8 are given by the ratios of their propagators:

$$\frac{\sigma(Z^0)}{\sigma(\gamma^*)} \sim \left(\frac{Q^2}{Q^2 + M_{Z^0}^2} \right)^2 \tag{1.9}$$

and

$$\frac{\sigma(\gamma^* Z^0)}{\sigma(\gamma^*)} \sim \left(\frac{Q^2}{Q^2 + M_{Z^0}^2} \right), \tag{1.10}$$

where M_{Z^0} is the mass of the Z^0 boson. Neutral Current events are selected in the range $1.5 < Q^2 < 45$ GeV^2 in this thesis, much smaller than $M_{Z^0}^2$, such that the last two terms in equation 1.8 can be neglected in the remainder of this chapter. The differential cross-section in the two variables x and Q^2 can be expressed in terms of structure functions as:

$$\frac{\mathrm{d}^2\sigma(x,Q^2)}{\mathrm{d}x\mathrm{d}Q^2} = \kappa \left(F_2(x,Q^2) - \frac{y^2}{Y_+} F_L(x,Q^2) \right) \tag{1.11}$$

with

$$\kappa = \frac{2\pi\alpha_{em}^2}{xQ^4} Y_+ \qquad \text{and} \qquad Y_+ = 2(1-y) + y^2, \tag{1.12}$$

where α_{em} is the electromagnetic coupling constant. $F_2(x, Q^2)$ is the most well known proton structure function and $F_L(x, Q^2)$ is called the longitudinal structure function. When electron-proton scattering is viewed as the interaction of a flux of virtual photons with the proton, the structure functions can be expressed in terms of the transverse (σ_T) and longitudinal (σ_L) photon cross-sections:

$$F_2(x, Q^2) = \frac{Q^2}{4\pi^2\alpha_{em}} \left[\sigma_T(x, Q^2) + \sigma_L(x, Q^2) \right] \tag{1.13}$$

and

$$F_L(x, Q^2) = \frac{Q^2}{4\pi^2\alpha_{em}} \sigma_L(x, Q^2). \tag{1.14}$$

Equations 1.13 and 1.14 show that F_2 measures the total $\gamma^* p$ cross-section, whereas F_L measures the contribution from longitudinally polarised photons. The positivity of σ_L and σ_T together with equations 1.13 and 1.14 enforces the following inequality:

$$0 \le F_L \le F_2. \tag{1.15}$$

The dependence on y in equations 1.11 and 1.12 and the hierarchy of equation 1.15 imply that the F_2 term is dominant in the low y region and the importance of F_L increases with y. Experimentally, it is not possible to separately measure the F_2 and F_L contributions to the cross-section at fixed s. Instead, measurements of the reduced cross-section, defined by:

$$\sigma_r(x, Q^2) = F_2(x, Q^2) - \frac{y^2}{Y_+} F_L(x, Q^2), \tag{1.16}$$

can be performed. Extractions of F_2 at HERA are typically performed for values of the inelasticity y up to 0.6, where only small corrections are needed for the F_L term.

1.4 The Quark Parton Model

The Quark Parton Model [4,5] assumes that hadrons are made up of constituent particles, called partons, that are identified with quarks $(u,\bar{u},d,...)$. It was introduced to explain the unexpected observation of scale invariance, or Bjorken scaling, seen in inelastic electron-proton scattering at SLAC [1,2]. The proton structure function, $F_2(x, Q^2)$, showed little dependence on Q^2 in the range $1 < Q^2 < 10$ GeV^2 at fixed x, providing evidence for point like constituents of the proton. The proton structure function can then be expressed as the weighted sum of the momentum distributions $f_i(x)$ of the constituent quarks i which define the probability of finding a parton i carrying a fraction x of the proton momemtum:

$$F_2(x, Q^2) \rightarrow F_2(x) = \sum_i e_i^2 x f_i(x). \qquad (1.17)$$

The summation is carried out over all species i of quarks with charge e_i. If quarks and anti-quarks were the only constituents of the proton, their momentum sum should be equal to unity, such that:

$$\sum_i \int x f_i(x) dx = 1. \qquad (1.18)$$

However, a value of ~ 0.5 instead of 1 was obtained in the fixed target experiments [6]. This puzzle finds an explanation in terms of the presence of non-charged constituents (gluons) within the framework of Quantum Chromodynamics (QCD) which is outlined in the next section. QCD also accounts for the scaling violations observed in the precise HERA measurements covering five orders of magnitude in Q^2 and extending from $x = 2 \times 10^{-5}$ up to $x = 0.65$. These measurements are presented in figure 1.2. It can be seen that F_2 falls slightly with Q^2 at high x, whereas it rises with Q^2 at low x. The scaling behaviour of F_2 is also seen in the plot for intermediate values of $x \sim 0.1$.
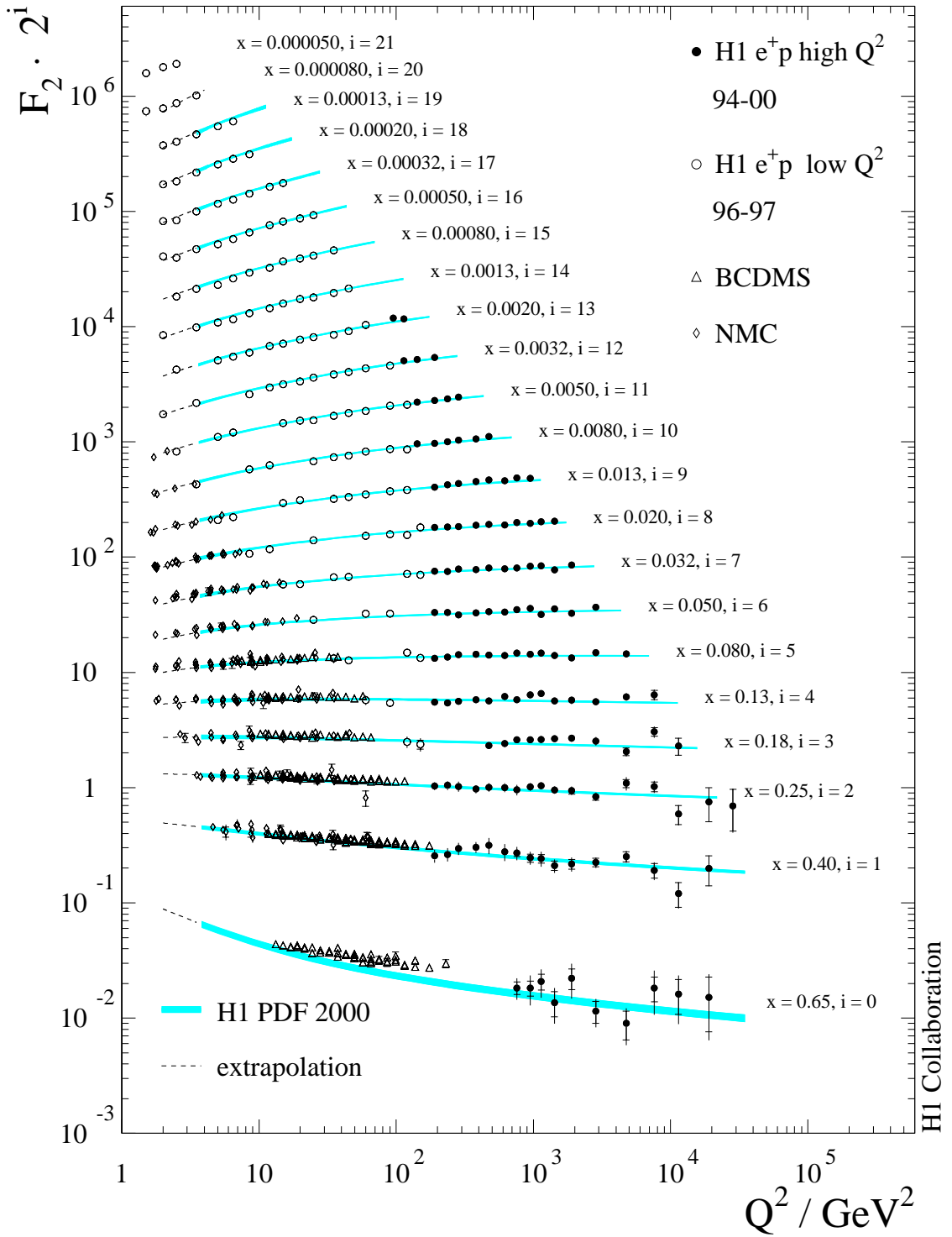
Figure 1.2: Measurements of the proton structure function F_2 as a function of Q^2 in bins of x compared to a QCD fit using the DGLAP evolution scheme. F_2 is multiplied by 2^i for cosmetic purposes.

1.5 Quantum Chromodynamics

Quantum ChromoDynamics (QCD) (see for example [7]) is a non-Abelian gauge field theory that describes the strong interaction. It possesses three colour charges (red, green or blue) that belong to the fundamental representation of the $SU(3)$ gauge group and that are carried by quarks. The strong interaction is mediated by eight massless bosons, called gluons. The number of gluons corresponds to the dimension of the adjoint representation of $SU(3)$ to which the interaction carriers belong. Due to the non-commutative structure of the gauge group, gluons also carry a bi-colour charge and can thus couple to each other. Feynman rules, which are used to form matrix elements, can be derived from the QCD Lagrangian, as in other field theories [3]. The cross-section for a given process can then be calculated once the ultraviolet divergences, which typically arise when one of the momenta in the loop integrals goes to infinity, have been removed using an appropriate regularisation scheme. The regularisation process introduces a dependence of the strong coupling constant α_s on the renormalisation scale μ. In the lowest order of perturbation theory, α_s is given by:

$$\alpha_s(\mu^2) = \frac{4\pi}{\beta_1 \ln(\mu^2/\Lambda_{QCD}^2)} \tag{1.19}$$

with

$$\beta_1 = 11 - \frac{2}{3}n_f, \tag{1.20}$$

where n_f is the number of active quark flavours whose mass is less than the scale μ. The QCD parameter Λ_{QCD} sets the scale for the running coupling. Measurements of the strong coupling α_s are presented, by convention, at the fixed reference scale $\mu_R = M_{Z^0}$. The α_s world average value is $0.1200 \pm 0.0028(\text{exp}) \pm 0.002(\text{scale})$ [3]. It follows from equation

---

[3]The QCD Lagrangian and the Feynman rules for the covariant and physical gauges can be notably found for example in [7]. Their mathematical expressions are not needed in the present discussion.

1.19 and the positivity of β_1 that the QCD coupling α_s is small at small distances that correspond to large momentum transfers μ, and a perturbative calculation in terms of α_s of the cross-section can be performed. This behaviour is known as **asymptotic freedom** and is heavily used in the interpretation of DIS data, where the relevant scale $\mu^2 = Q^2$. At low momentum transfer μ, or large distances, non-pertubative methods need to be used in calculations since the coupling constant gets large, which explains why quarks are confined within hadrons. This is know as **infrared slavery**.

1.6   QCD Hard Scattering Factorisation

In processes involving at least one hadron in the initial state, observables cannot be fully calculated pertubatively because of infrared slavery. Hard scattering factorisation theorems, that allow us to disentangle the pertubatively calculable (hard) aspects from the non-perturbatively calculable (soft) aspects of an interaction, have been proved for numerous processes. In DIS, the mathematical expression of the factorisation theorem is [8]:

$$F_2^{(Vh)}(x, Q^2) = \sum_i \int_x^1 d\xi \; C_2^{Vi}\left(x/\xi, Q^2/\mu^2, \alpha_s(\mu^2)\right) \; f_{i/h}(\xi, \mu^2) \tag{1.21}$$

where the sum over partons i includes quarks, anti-quarks and gluons. The separation between high and low momentum physics is done at an arbitrary factorisation scale μ, only constrained by $\mu^2 \gg \Lambda_{QCD}^2$. $f_{i/h}(\xi, \mu^2)$ is the parton distribution function (*pdf*) of parton i which is specific to the hadron h and depends on the factorisation scale. The *pdf*s are universal in the sense that they do not depend on the type of hard scattering under consideration and on the electroweak vector boson, V [4]. $C_2^{(Vi)}(x/\xi, Q^2/\mu^2, \alpha_s(\mu^2))$

---

[4]However, *pdf*s differ depending on the scheme used to separate the short distance from the long distance dynamics beyond the lowest order in perturbation theory. The DIS and the $\overline{\text{MS}}$ are the most commonly used, but their discussion goes beyond the handwaving discussion presented here (see for example [7]).

is the corresponding infra-red safe coefficient that is independent of the external hadron. This coefficient varies with the exchanged boson and the parton type i.

The factorisation theorem is valid up to corrections that are power suppressed in Q^2, or equivalently it is at **leading twist** theorem.

QCD factorisation implies that cross-sections can be predicted for various processes once the universal parton distribution functions have been determined using the result of a given experiment. Through F_2 measurements, the HERA data provide the strongest constraints on the proton *pdf*s.

1.7 The DGLAP Evolution Equations

The evolution equations are a consequence of factorisation. They allow us to compute the parton distributions at any scale μ' knowing the *pdf*s at a scale μ, provided that both μ and μ' are large enough such that $\alpha_s(\mu)$ and $\alpha_s(\mu')$ are small. At the leading order ($\mathcal{O}(\alpha_s)$) and taking the scale μ^2 equal to Q^2, the most important contributions to the evolution equations correspond to the DGLAP equations that were derived by Dokshitzer, Gribov, Lipatov, Altarelli and Parisi [9–12]:

$$\frac{\mathrm{d}q_i(x,Q^2)}{\mathrm{d}\ln Q^2} = \frac{\alpha_s(Q^2)}{2\pi} \int_x^1 \frac{\mathrm{d}z}{z} \left[q_i(z,Q^2) P_{qq}^{LO}\left(\frac{x}{z}\right) + g(z,Q^2) P_{qg}^{LO}\left(\frac{x}{z}\right) \right] \tag{1.22}$$

and

$$\frac{\mathrm{d}g(x,Q^2)}{\mathrm{d}\ln Q^2} = \frac{\alpha_s(Q^2)}{2\pi} \int_x^1 \frac{\mathrm{d}z}{z} \left[\sum_{i=1,2f} q_i(z,Q^2) P_{gq}^{LO}\left(\frac{x}{z}\right) + g(z,Q^2) P_{gg}^{LO}\left(\frac{x}{z}\right) \right], \tag{1.23}$$

where i runs over quarks and anti-quarks of all flavours. f is the number of quark flavours. q and g denote the quark and gluon distributions. The P_{ij}, called **splitting functions**, give the probability for finding a parton i with momentum fraction x originating from

parton j with momentum fraction z $(> x)$. The different splitting functions corresponding to the different couplings, $q \rightarrow qg$, $q \rightarrow gq$, $g \rightarrow q\bar{q}$ and $g \rightarrow gg$, are illustrated in figure 1.3.
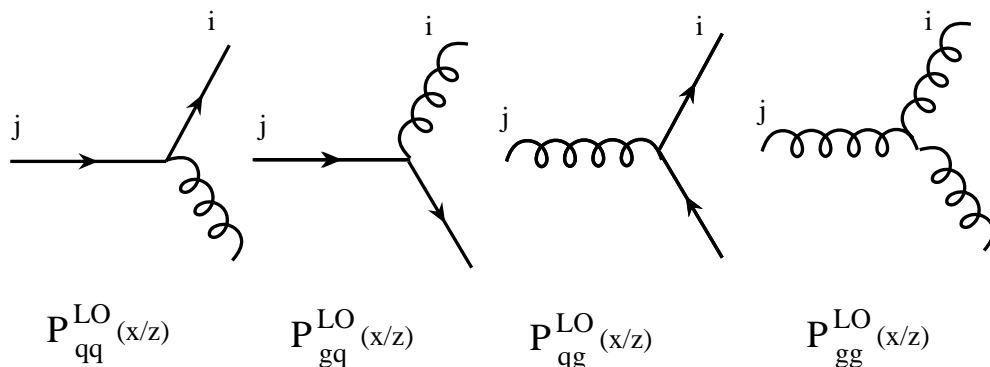
Figure 1.3: Representation of the four LO splitting functions $P_{ij}^{LO}(x/z)$ that give the probabilty for parton j with momentum fraction z to split to produce a parton i with momentum fraction x.

The scaling violations can be physically interpreted within QCD. Non-valence (sea) quarks and gluons are generated by the DGLAP mechanism. As Q^2 increases, more partons, with each having a lower fraction of the proton momentum x, can be resolved, which leads to the observed logarithmic dependence on Q^2

The DGLAP evolution equations are now known to the next-to-next-to-leading-order (NNLO) following the recent calculation by Vogt, Moch and Vermaseren [13].

Using the evolution equation formalism at the next-to-leading order, the H1 parton distributions functions [14] are shown in figure 1.4 for $Q^2 = 10$ GeV^2. These results are obtained using only NC and CC data from H1. The importance of the gluon distribution relative to the others increases dramatically with decreasing x.

The DGLAP equations effectively sum up all the contributions to the cross-section proportional to $[\alpha_s(Q^2) \ln(Q^2/Q_0^2)]^n$ for fixed Q_0^2 which corresponds to the **leading logarithm**
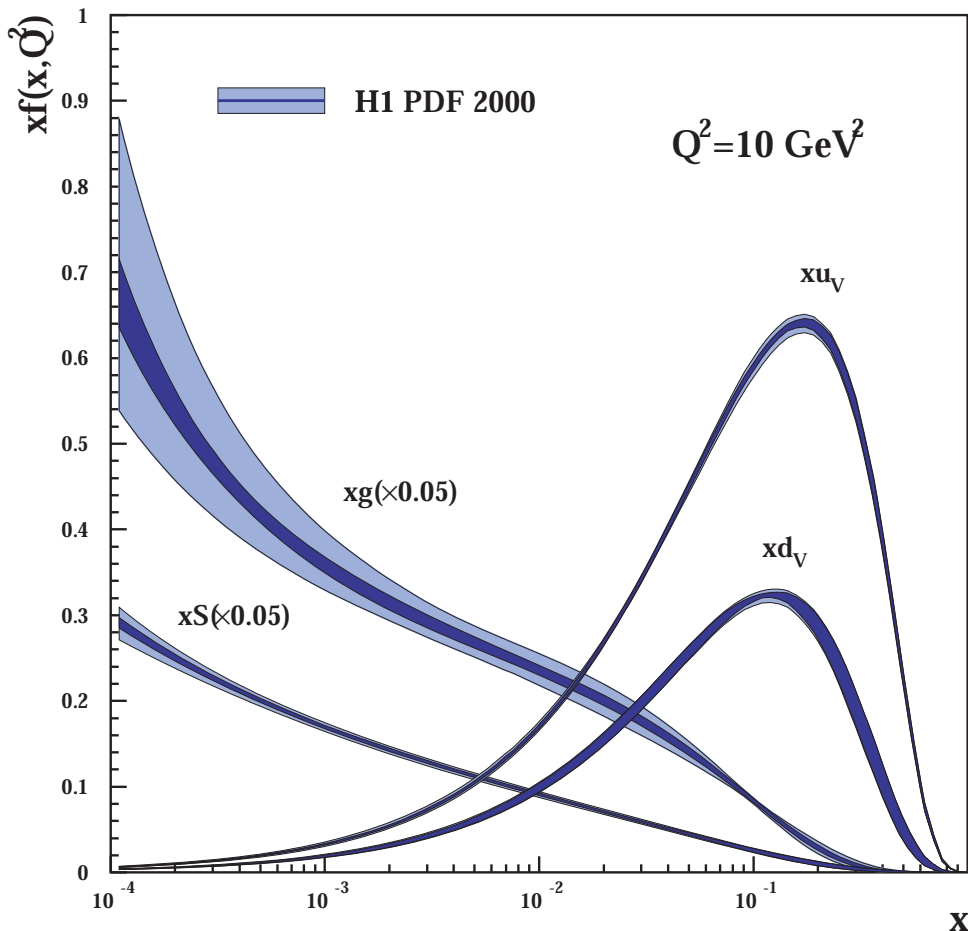
Figure 1.4: The parton distributions functions, from the 'H1 PDF 2000' next-to-leading order (NLO) DGLAP fit, are shown at the scale $Q^2 = 10$ GeV^2.

approximation (LLA) valid in the limit:

$$\alpha_s(Q^2) \ln\left(\frac{1}{x}\right) \ll \alpha_s(Q^2) \ln\left(\frac{Q^2}{Q_0^2}\right) < 1. \tag{1.24}$$

The gluon-gluon splitting P_{gg} function behaves like $\sim \alpha_s/x$, and thus it possesses a singularity at very small x. In this regime, the DGLAP formalism mathematically breaks down and the leading $\alpha_s \ln(1/x)$ terms must also be considered. The BFKL evolution equation effectively sums $\alpha_s \ln(1/x)$ contributions. Experimentally, the DGLAP approach has been very successful in describing the inclusive H1 data down to the smallest values of x. Some final state observables measured at H1 [15–17] are better described when BFKL effects are considered.

Chapter 2

Diffractive Deep Inelastic Scattering

High energy diffraction, and more specifically diffractive DIS, constitutes a very extended topic, and only the most relevant aspects of the theory necessary to follow the work of this thesis are discussed in this chapter.

About 10% of the DIS events measured at HERA are characterised by a large region devoid of activity or 'rapidity gap' [1] between the hadronic final state observed in the main detector and the proton or its dissociation products forming a low mass hadronic state which passes unobserved into the forward beampipe. This class of DIS events is called 'diffractive' since the collisions are elastic or quasi-elastic. The exchange of a colourless object between the proton and the photon was introduced to explain the presence of the rapidity gap. The existence of such an exchange with vacuum quantum numbers ($C = 1, P = 1$), called the pomeron, had originally been postulated to describe the rise with the centre of mass energy of the total and elastic cross-sections observed in hadron-hadron collisions [18]. The discussion of diffractive DIS requires additional kinematic variables to describe the three new degrees of freedom introduced by the presence of the rapidity gap between the outgoing proton and the diffracted photon.

---

[1]Rapidity is defined by $y = \frac{1}{2} \ln \frac{E+p_z}{E-p_z}$. Small rapidity gaps that are exponentially suppressed occur naturally in non-diffractive DIS.

2.1 Diffractive Kinematics
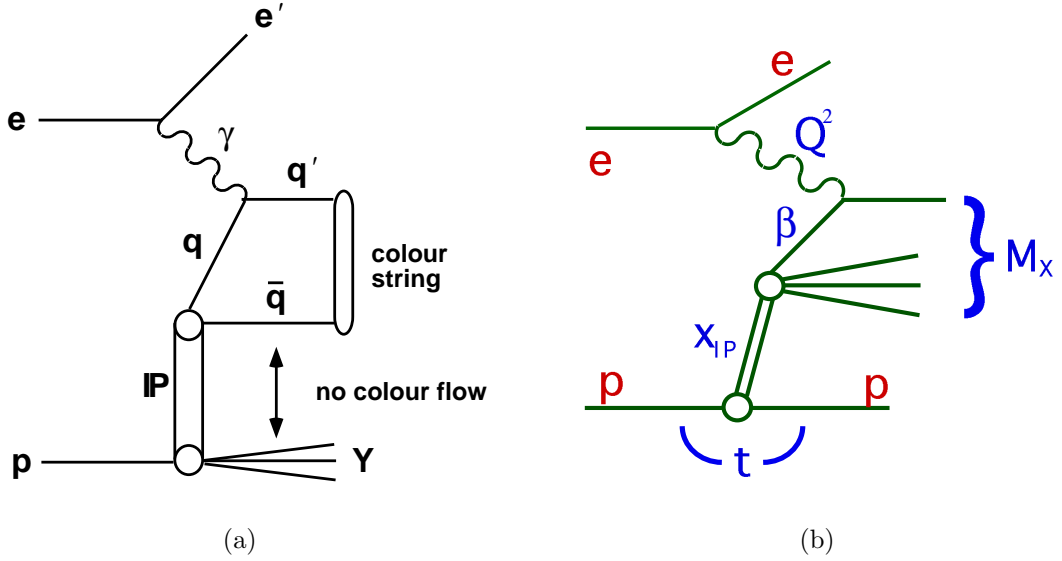
Figure 2.1: (a) Schematic representation of diffractive DIS and (b) illustration of the diffractive kinematic variables.

In what follows, X is used to label the hadronic state into which the photon dissociates, and Y refers to the scattered proton or the proton remnant. A schematic representation of diffractive DIS is shown in figure 2.1 (a). p_X and p_Y designate their 4-vectors. The 4-momentum transfer squared across the proton vertex (see figure 2.1 (b)) is defined by:

$$t = (p - p_Y)^2. \tag{2.1}$$

Two further diffractive variables are introduced:

$$x_{I\!\!P} = \frac{q \cdot (p - p_Y)}{q \cdot p} \approx \frac{Q^2 + M_X^2}{Q^2 + W^2}, \tag{2.2}$$

and

$$\beta = \frac{x}{x_{I\!\!P}} = \frac{-q^2}{2q \cdot (p - p_Y)} \approx \frac{Q^2}{Q^2 + M_X^2}. \tag{2.3}$$

The mass of the proton and the squared four momentum transfer t have been neglected in

the approximation of equations 2.2 and 2.3 since $m_p^2 \ll Q^2$, W^2 and $|t| \ll Q^2$, M_X^2 for the limits appropriate to this analysis. $x_{I\!P}$ is the fraction of the 4-momentum of the proton transferred to the pomeron, and β is interpreted as the fraction of the 4-momentum of the pomeron carried by the struck quark when a partonic structure is ascribed to the colourless exchange. β is therefore the analogue of x in inclusive DIS. Thus, the five independent kinematic variables typically used to describe diffractive scattering are Q^2, t, $x_{I\!P}$, β and M_Y, the mass of the system Y.

2.2 The Diffractive Reduced Cross-section

The expression of the cross-section for diffractive DIS is based on the formalism used in the discussion of inclusive DIS. The only difference resides in the additional dependence introduced by the new degrees of freedom. The measurement performed later will be integrated over M_Y and t leaving a three-fold differential cross-section. The diffractive differential cross-section is then expressed in terms of the reduced cross-section, $\sigma_r^{D(3)}(\beta, Q^2, x_{IP})$, as follows:

$$(2.4)$$

$$\frac{\mathrm{d}^3 \sigma_{ep \to eXp}}{\mathrm{d}\beta \mathrm{d}Q^2 \mathrm{d}x_{IP}} = \frac{4\pi\alpha_{em}^2}{\beta Q^4} \left(1 - y + \frac{y^2}{2}\right) \sigma_r^{D(3)}(\beta, Q^2, x_{IP}). \qquad (2.5)$$

The latter quantity can again be related to the structure functions by :

$$\sigma_r^{D(3)}(\beta, Q^2, x_{IP}) = F_2^{D(3)}(\beta, Q^2, x_{IP}) - \frac{y^2}{1 + (1-y)^2} F_L^{D(3)}(\beta, Q^2, x_{IP}). \qquad (2.6)$$

2.3 QCD Hard Scattering Factorisation for Diffractive DIS

Collins [19] has proved a factorisation theorem for diffractive hard processes in DIS that allows us to separate the short from the long distance dynamics in the same manner as in DIS. The diffractive cross-section can be expressed at the leading twist in terms of diffractive parton distribution functions, $f(x, Q^2, x_{IP})$, convoluted with a hard-scattering cross-section [2]:

$$\sigma_r^{D(3)} \sim \sum_i f_i^D(x_{IP}, x, Q^2) \otimes C_2^{Vi}(x, Q^2), \qquad (2.7)$$

where the sum runs over quark flavours. The C_2^{Vi} are the same hard scattering coefficient functions that were introduced for inclusive DIS. f_i^D are diffractive parton densities which obey the DGLAP equations, and the DIS evolution formalism thus also applies to diffraction. The theorem holds for any fixed value of x_{IP}. This property is exploited in the fits performed by H1 that will be discussed in the next section.

2.4 The Resolved Pomeron Model

Ingelman and Schlein [20] assigned a parton structure to the diffractive exchange. They effectively factorised the diffractive *pdf*s into pomeron parton distributions functions, $f_i^{IP}(\beta, Q^2)$, and a pomeron flux factor, $f_{IP/p}(x_{IP})$, which can be qualitatively interpreted as the probability of the emission of a pomeron by the proton. Hence, the diffractive *pdf*s

---

[2]The cross-section has been integrated over t in the formula presented here.

are mathematically expressed as:

$$f_i^D(x_{IP}, x, Q^2) = f_{IP/p}(x_{IP}) \cdot f_i^{IP}(\beta = x/x_{I\!P}, Q^2), \tag{2.8}$$

and the factorisation equation 2.7 can be rewritten in terms of the *pdf*s of the pomeron as:

$$\sigma_r^{D(3)} \sim f_{IP/p}(x_{IP}) \sum_i f_i^{IP}(x, Q^2) \otimes C_i(x, Q^2) \tag{2.9}$$

$$\sim f_{IP}(x_{IP}) \sigma_r^{IP}(\beta, Q^2), \tag{2.10}$$

where σ_r^{IP} is the ($x_{I\!P}$ independent) eIP cross-section. The flux factor is assumed to be independent of Q^2, which expresses that the physics at the proton vertex is not related to what happens at the photon vertex. This is known as 'Regge factorisation' which finds strong experimental support at HERA. In figure 2.2, the measured reduced diffractive cross-section at intermediate Q^2 is divided by the flux factor and plotted as a function of β for different values of $x_{I\!P}$. The similarity of the normalised cross-section in the overlap regions between different $x_{I\!P}$ values validates the Ingelman-Schlein assumption.

Regge theory has been very successful in describing soft hadronic interactions and elastic scattering [21]. This motivates the Regge-based parametrisation of the pomeron flux factor:

$$f_{IP}(x_{IP}) = \int_{t_{cut}}^{t_{min}} \frac{e^{B_{IP}t}}{x_{IP}^{2\alpha_{IP}(t)-1}} \mathrm{d}t, \tag{2.11}$$

where $t_{cut} = -1.0$ GeV^2 is defined by the selection technique described in section 5.1 and t_{min} is the minimum kinematically allowed value. The $\alpha_{IP}(t)$ term is parametrised with $\alpha_{IP}(t) = \alpha_{IP}(0) + \alpha_{IP}'t$ [21].
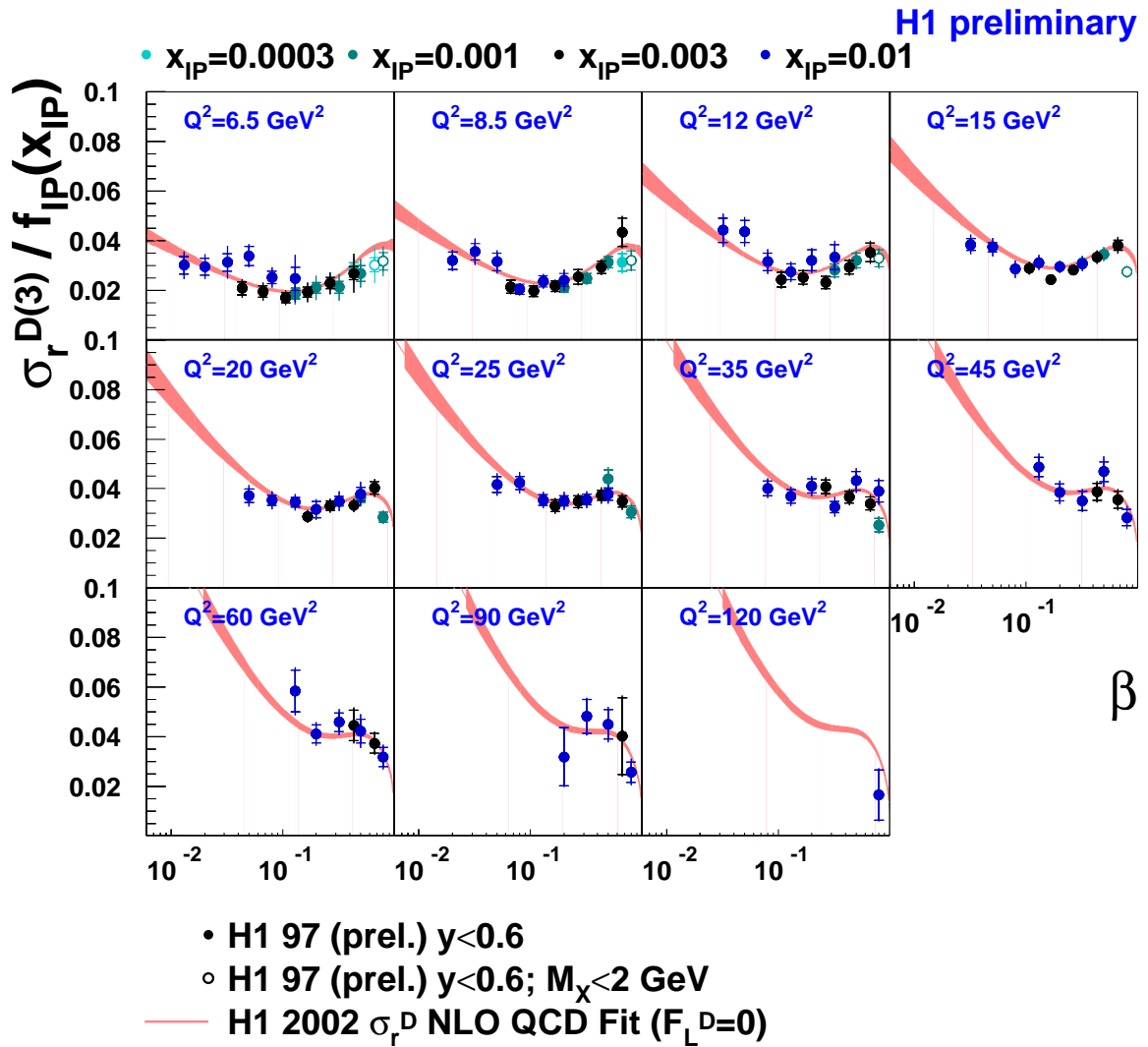
Figure 2.2: Comparison of the diffractive reduced cross-section divided by the pomeron flux for different values of $x_{I\!P}$ as a function of β in Q^2 bins. The prediction of a NLO fit is also shown. Only data points with $y < 0.6$ are presented to minimise the influence of the longitudinal diffractive structure function.

2.5 H1 Diffractive Parton Distributions Functions

A deviation from the factorisation expression of equation 2.8 has been observed in the H1 diffractive reduced cross-section at high β that can be accommodated when the exchange of sub-leading reggeon trajectories is allowed. This comes as no surprise as the exchange of mesons in addition to the pomeron has also been needed to describe the energy dependence

of total hadron-hadron cross-sections [18]. An extra term is therefore added to the cross-section 2.10:

$$\sigma_r^{D(3)}(\beta, Q^2, x_{IP}) = f_{IP}(x_{IP})\sigma_r^{IP}(\beta, Q^2) + f_{IR}(x_{IP})\sigma_r^{IR}(\beta, Q^2), \qquad (2.12)$$

where the reggeon flux factor is given by 2.11 with the *IP* label replaced by *IR*. The value of $\alpha_{IP}(0)$ (~ 1.17) was determined in [22]. The possibility of interference between the pomeron and reggeon term was considered in [23]. No conclusion could be drawn about the role of the interference term without further precision measurements at high $x_{I\!P}$.

The starting *pdf*s for the pomeron consist of a light quark (u,d,s) flavour singlet distribution and a gluon distribution that are parametrised at the scale of 3 GeV^2. The charm contribution, which arises from boson gluon fusion, is calculated in the fixed flavour massive scheme [3]. The meson *pdf*s are evolved independently of the pomeron using a pion parton distribution function. A NLO fit was performed to the H1 data with $Q^2 > 6.5$ GeV^2 and a cut on $M_X > 2$ GeV was applied in order to remove the non-leading twist component of the cross-section. The experimental systematic errors were propagated to the fits for the first time. The gluon and singlet distributions (taken from [22]), normalised such that the pomeron flux is equal to unity at $x_{I\!P} = 0.003$, are shown as a function of the variable z for three different values of Q^2 in figure 2.3. z is equal to β when the photon interacts with a quark and is equal to the fractional momentum carried by the gluon, with $\beta < z$, when the parton entering the hard scattering is a gluon. The plots illustrate that the momentum of the diffractive exchange is mainly carried by gluons. The integrated fraction of this momentum amounts to 75% and is constant with Q^2 within errors. The diffractive gluon distribution displays a strong rise with decreasing z that is also observed in the inclusive distribution. The quark singlet distribution is approximately flat and extends to the highest z in contrast with the quark distribution in inclusive DIS shown

---

[3]In this scheme, the charm quarks are always treated as heavy particles and never as partons, such that they are always produced dynamically via $\gamma^* g \to c\bar{c}$.
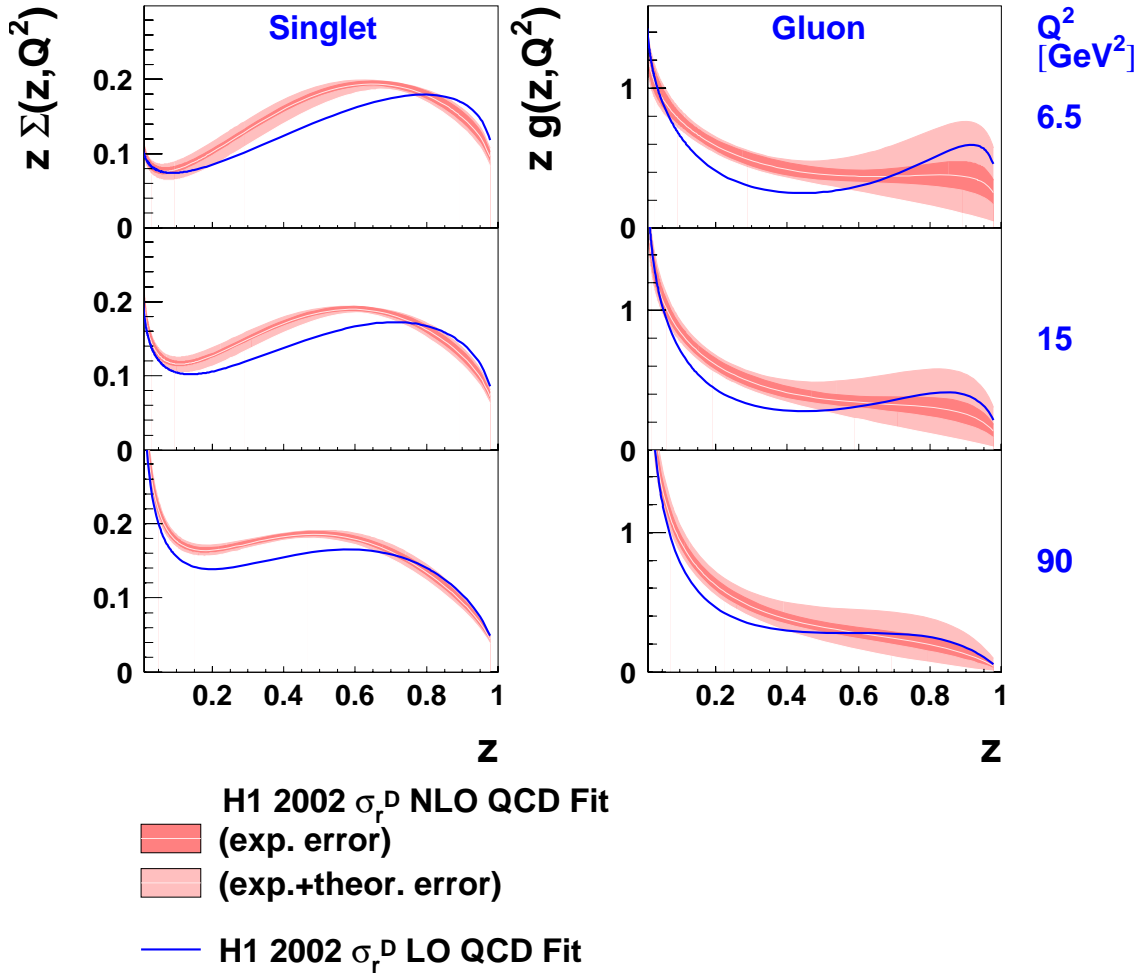
Figure 2.3: The Q^2 evolution of the quark singlet (left) and gluon (right) diffractive parton densities obtained with the NLO QCD fit described in the text are plotted as a function of z. The inner band comprises the statistical and systematic experimental errors and the outer band shows the total error with the theoretical uncertainties included. The result of the LO fit is also shown.

in figure 1.4.

2.6 Comparison between the Predictions of H1 Fits and Data

Invoking Collins' factorisation theorem, the diffractive parton densities can be used to make predictions for the cross-sections of diffractive final state observables. In [24], the diffractive production of $D^{*\pm}$ is investigated. Charm production proceeds dominantly via
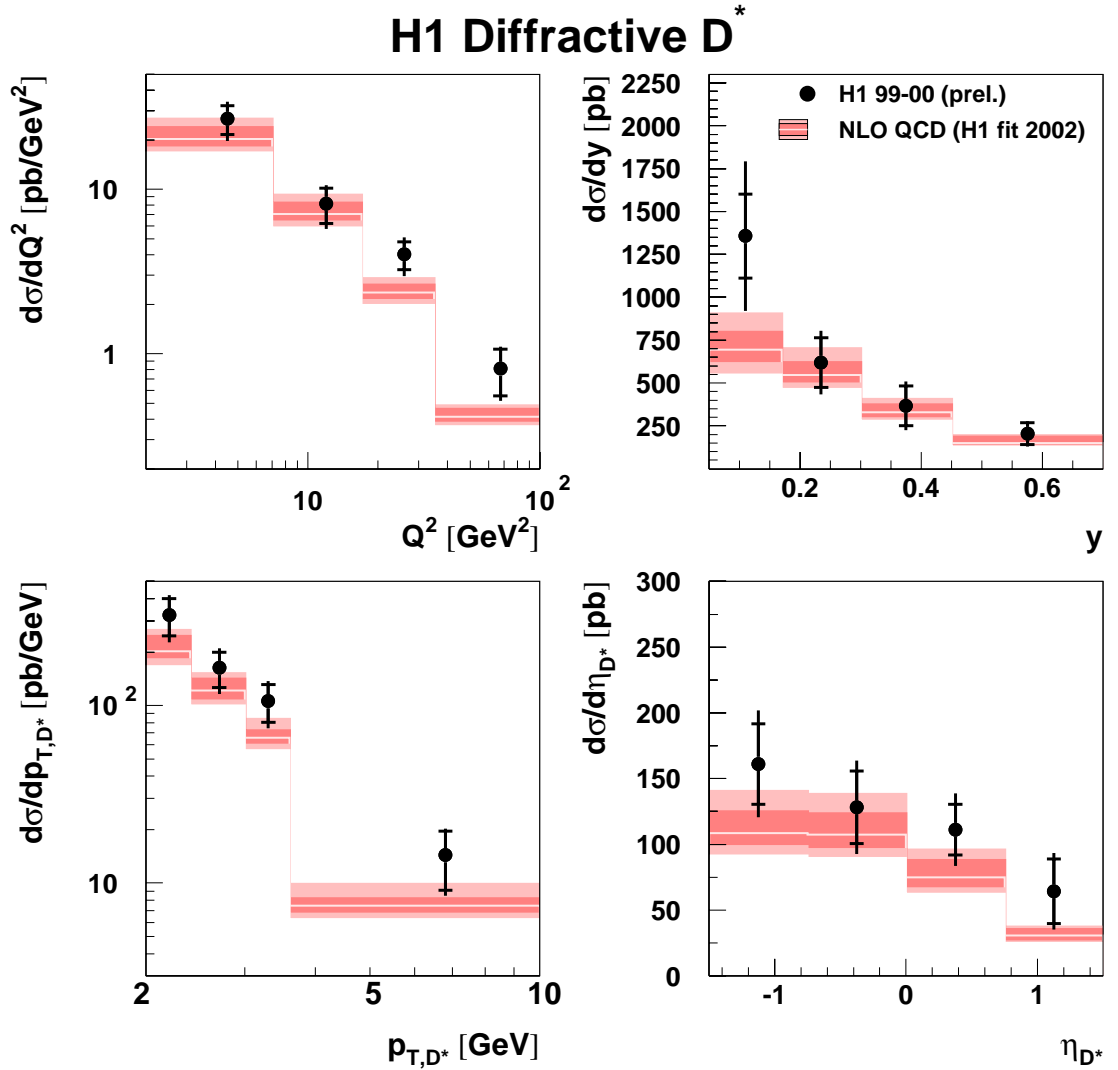
Figure 2.4: Comparison between the measured diffractive D^* meson production cross-sections expressed as a function of Q^2, y, p_{T,D^*} and η_{T,D^*} and the theoretical predictions based on NLO diffractive *pdf*s.

the boson-gluon fusion mechanism ($\gamma^* g \to c\bar{c}$) and is therefore very sensitive to the gluon distribution of the diffractive exchange. Differential cross-sections as a function of the photon virtuality Q^2, the elasticity y, the transverse momentum p_{T,D^*} and the rapidity η_{D^*} of the D^* meson are all compared in figure 2.4 with a NLO calculation that uses the H1 NLO diffractive partons densities. In all cases, there is good agreement between data and theory within the experimental and theoretical uncertainties.
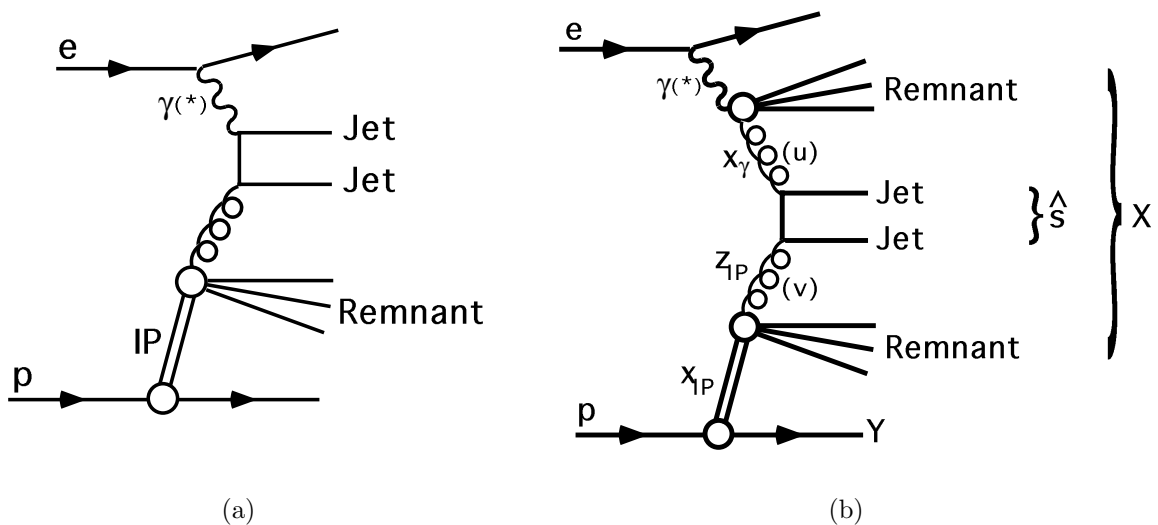
Figure 2.5: Diagrams representing diffractive jet production in DIS (a) and in the 're-solved' photoproduction regime (b).

Dijets in diffractive DIS and photoproduction have also been measured at H1 [25]. The DIS process is sketched in figure 2.5 (a). The same process exists in 'direct' photoproduction, when the proton interacts in a point-like manner. In the 'resolved' photoproduction process represented in figure 2.5 (b), a parton originating from the fluctuation of the photon into a hadronic state enters the hard scattering. The new kinematic variable $z_{I\!P}$, defined by:

$$z_{I\!P} = \beta \left(1 + \frac{\hat{s}}{Q^2} \right),$$ (2.13)

is introduced to estimate the fraction z of the diffractive exchange momentum that enters the hard process. $\hat{s}$ denotes the invariant mass squared of the dijet system. The univer-

sality of the diffractive *pdf*s is again confirmed in figure 2.6 where the DIS diffractive dijet cross-section as a function of $z_{I\!P}$ (a) and as a function of $\log x_{I\!P}$ (b) are well reproduced by the NLO order calculations.

H1 Diffractive DIS Dijets
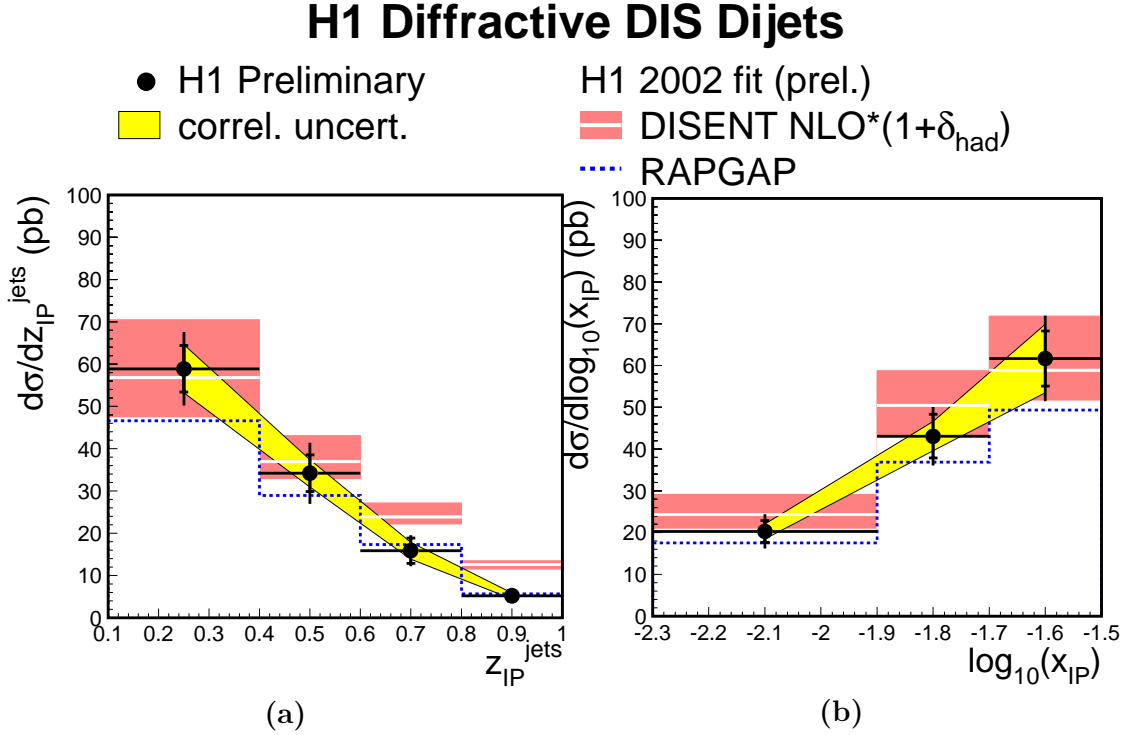
Figure 2.6: Differential cross-sections, shown as a function of $z_{I\!P}$ (a) and $\log x_{I\!P}$ (b), for diffractive dijet production in DIS. The data, shown as points with (statistical and total) error bars, is compared with a NLO prediction using NLO diffractive *pdf*s.

The fits fail to describe diffractive dijet production in the photoproduction regime, and the fit prediction for the diffractive proton-proton interaction measured at the TEVATRON is one order of magnitude too large [22]. This was perhaps expected as the QCD factorisation theorem in diffraction does not apply for these measurements [19].

2.7 The Saturation Model

In the proton rest frame, DIS can be described by the formation of a long-lived partonic fluctuation of the photon long before the interaction with the proton takes place. The photonic fluctuation is dominated by the $q\bar{q}$ dipole that interacts with the proton. The inclusive cross-section for transverse and longitudinal photons can be calculated for a specified dipole cross-section $\hat{\sigma}_{T,L}$ with:

$$\sigma_{T,L}(x, Q^2) = \int d^2\mathbf{r} dz |\psi_{T,L}(Q^2, \mathbf{r}, z)|^2 \hat{\sigma}(Q^2, r, z), \qquad (2.14)$$

where $\psi_{T,L}(Q^2, \mathbf{r})$ is the light cone wavefunction for transverse and longitudinal photons. z is the momentum fraction of the photon carried by the quark as depicted in figure 2.7 and $r^2 \sim 1/Q^2$ is the transverse size of the dipole. Large size dipoles interact with the proton similarly to soft hadron-hadron interactions whereas the large momentum transfer associated with small dipoles can be dealt with perturbatively.
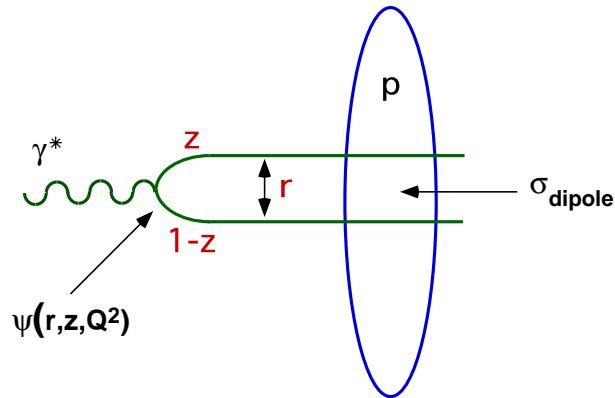
Figure 2.7: Dipole picture of $\gamma^* p$ scattering.

The diffractive cross-section is then given via the optical theorem by:

$$\sigma_{T,L}(x, Q^2) = \int d^2\mathbf{r} dz |\psi_{T,L}(Q^2, \mathbf{r}, z)|^2 \hat{\sigma}^2(Q^2, r, z). \qquad (2.15)$$

It is important to contrast the collinear factorisation approach of diffractive parton den-

sities with the phenomenological model discussed here. In the former scheme, two different sets of parton distributions functions were needed in order to describe inclusive and diffractive processes. In contrast the same dipole cross-sections applies to elastic and total cross-section in the latter approach. Among the different models that exist for the dipole cross-section, only the saturation model will be discussed here as it forms the basis of the SATRAP Monte Carlo simulation that is used later in the diffractive analysis. The objective of the saturation model is to describe the transition from high to low Q^2 at low x. The idea of the model is to damp the strong rise of the cross-section as x decreases by postulating a saturation of the dipole cross-section at low x, for example due to parton recombinations that are not modeled by the linear evolution equations. The effective dipole cross section is expressed as:

$$\hat{\sigma}(x, r^2) = \sigma_0 \left[1 - \exp\left(-\frac{r^2}{R_0^2(x)} \right) \right], \tag{2.16}$$

where $R_0^2(x)$ is the *saturation radius* given by:

$$R_0(x) = \frac{1}{Q_0} \left(\frac{x}{x_0} \right)^{\frac{\lambda}{2}}, \tag{2.17}$$

with $Q_0^2 = 1$ GeV^2. Hence, there are just three free parameters to be determined from fits to the inclusive data: x_0, λ and σ_0. From a recent publication [26], appropriate values for these three parameters were found to be, for $x < 0.01$:

$$\sigma_0 = 23 \text{ mb}, \ \lambda = 0.29, \ x_0 = 3 \times 10^{-4}. \tag{2.18}$$

Once these parameters are specified, the diffractive cross-section can be calculated at $t = 0$ GeV^2 using equation 2.15. Thus, the only additional free parameter required is the slope parameter, b. A reasonable description is obtained with $b = 6$ GeV^{-2} [27].

Chapter 3

The H1 Experiment

At the end of the year 2000, the H1 detector was modified to take full advantage of the HERA high luminosity upgrade. As the data analysed in this thesis were collected during a dedicated run with minimum bias triggers in 1999, the pre-upgrade H1 detector is described in this chapter after a brief introduction to the pre-upgrade HERA accelerator often referred to as HERA I. The emphasis will be put on the detector components relevant to this analysis. HERA delivers multi-bunch beams with a high collision frequency in order to achieve the high luminosities necessary for high precision measurements and the study of rare processes in electron-proton interactions. This necessitates a sophisticated four-level trigger system. The trigger requirements on the trigger system in the 1999 minimum bias data taking is discussed in the remainder of this chapter.

3.1   The HERA Accelerator

The Hadron Electron Ring Accelerator (HERA), situated at the Deutsches Elektronen Synchroton (DESY) laboratory in Hamburg, is the first electron-proton collider in the world and was commissioned during the year 1991. The HERA storage ring, represented

in figure 3.1, has a circumference of 6336 m and consists of two independent accelerators, one for protons and the other for electrons or positrons.
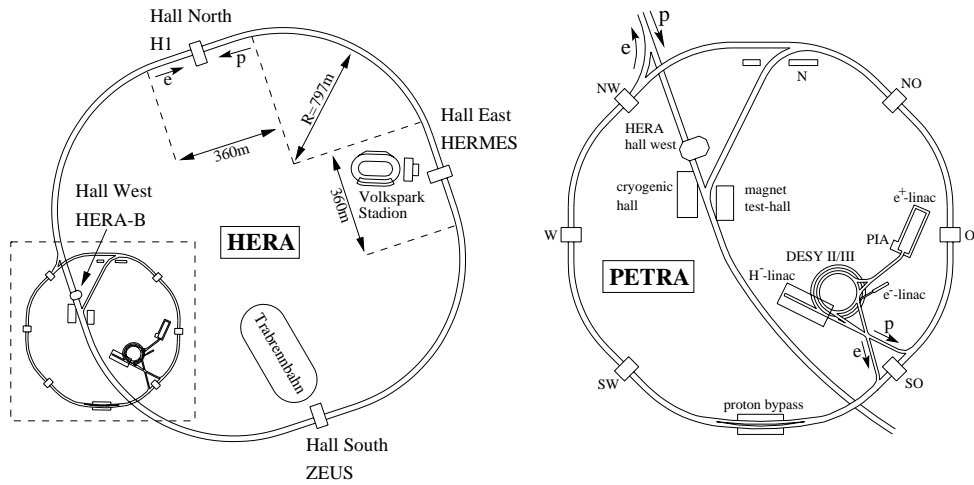
Figure 3.1: The left figure shows the HERA accelerator with the PETRA pre-accelerator in the dotted box, an enlarged view of which is given on the right.

Electrons are initially accelerated to an energy of 14 GeV with a linear accelerator, the e-LINAC, and two circular accelerators, DESY-II and PETRA. They are then injected into HERA where they reach their final energy of 27.5 GeV. Protons, produced from a source of H^+ ions, are first accelerated to an energy of 40 GeV with the DESY III and PETRA rings, and then brought to an energy of 920 GeV in HERA. During the transfer of a proton bunch from PETRA to HERA, a small fraction of the proton current escapes from the main bunch and forms satellite bunches separated in time by 4.8 ns from the main bunch. In HERA, protons and electrons are stored up to 220 bunches of 10^{10} to 10^{11} particles each. The bunch crossing interval is 96 ns. Approximately 175 bunches are collided, the others, called pilot bunches, are not brought into collision. Pilot bunches are used to estimate backgrounds arising from beam-gas and beam-wall interactions.

The 27.5 GeV electrons and the 920 GeV proton beams[1] are collided head on at north and south interaction points where the H1 and ZEUS detectors are located, respectively.

Two other detectors, HERMES and HERA-B, situated at east and west interaction points,

---

[1]The energy of the proton beam was 820 GeV before 1998.

use only one of the beams. The HERMES experiment collides longitudinally polarised electrons with a polarised gas jet target of either H, D or ^{3}He to investigate the spin structure functions of nucleons. The HERA-B experiment was assigned to study CP violation in the B Meson system produced in the collision of protons with either Carbon, Aluminium, Titanium or Tungsten target wires. In the H1 and ZEUS experiments, the structure of the constituents of the proton, neutral and charged current processes and physics beyond the Standard Model are studied using the very high resolving power provided by the high energies of the HERA beams.

3.2   Overview of the H1 detector

The large difference in energy between the electron and proton beams leads to a boost of the scattered particles in the direction of the outgoing proton. This direction, also called the forward direction, is used to define the z-axis of a right-handed Cartesian coordinate system (x, y, z) centered about the nominal interaction point. The x-axis points towards the centre of the HERA accelerator. The angle between a particle and the positive direction of the z-axis defines the polar angle θ of a cylindrical coordinate sytem. Its azimuthal angle is defined by the angle formed by a particle and the x-axis in the (x, y) plane. In lepton-hadron and hadron-hadron collisions, the variable pseudo-rapidity is frequently used instead of the polar angle for ultra-relativistic particles. It is defined by $\eta = -\ln(\tan\frac{\theta}{2})$.

The layout of the H1 [28, 29] (see figure 3.2) detector only differs from other detectors in collider experiments in that it is assymmetric and highly segmented in the proton direction in order to provide a very good reconstruction of the boosted hadronic final state.

Each sub-detector of the H1 apparatus possesses a cylindrical symmetry about the beam-pipe $\boxed{1}$. Two micro-vertex silicon detectors, the Central Silicon Tracker (CST) and the

HERA Experiment H1

1	Beam pipe and beam magnets
2	Central tracking chambers
3	Forward tracking and Transition radiators
4	Electromagnetic Calorimeter (lead)
5	Hadronic Calorimeter (stainless steel)
6	Superconducting coil (1.2T)
7	Compensating magnet
8	Helium cryogenics

Liquid Argon

9	Muon chambers
10	Instrumented iron (Iron slabs + streamer tube detectors)
11	Muon toroid magnet
12	Warm electromagnetic calorimeter
13	Plug calorimeter (Cu, Si)
14	Concrete shielding
15	Liquid Argon cryostat

Figure 3.2: Isometric projection of the H1 detector.

Backward Silicon Tracker (BST) are located in the innermost layer very close to the interaction point. They are surrounded by the Central Tracking Detector (CTD) 2. The Forward Tracking Detector (FTD) 3 and the Backward Drift (BDC) chamber lie on either side of the Central Tracker. The Liquid Argon (LAr) calorimeter is located around the trackers and is made up of an electromagnetic section 4 and an hadronic section 5. The LAr is in turn surrounded by a superconducting solenoid magnet 7 providing an

axial field of 1.5 T. The instrumented iron return yoke of the magnet $\boxed{10}$ is used to detect muons and the residues of hadronic showers. The Forward Muon Detector $\boxed{11}$ allows the detection of further muons making small angles with the beam-pipe in the direction of the outgoing protons. Two other calorimeters situated outside the trackers, the PLUG $\boxed{13}$ and SpaCal $\boxed{12}$, respectively, cover the very forward and backward directions. The Forward Proton Spectrometer (FPS), the Forward Tagger System (FTS) and the Forward Neutron Calorimeter (FNC), not represented in figure 3.2, are used to detect protons or proton fragments escaping the central detector along the beam-pipe. The FTS consists of five scintillator arrays located 9, 16, 24, 53 and 92 meters away from the nominal interaction point. The name 'Proton Roman Tagger' (PRT) is commonly used to designate the scintillators positioned 24 meters away from the central detector. The FPS is made of four movable stations called Roman pots situated at 63, 80, 81 and 90 metres in the forward direction. Additional detectors used to detect electrons in photoproduction events and to measure the luminosity are installed at the rear of the main detector. The main ones are the Electon Taggers ET33 and ET44 at z = -33.4 and -43.2 m respectively, and the Photon Detector (PD) at z = -103.1m.

3.3   The Tracking System

The goal of the tracking system (see figure 3.3) is to reconstruct precisely jets and isolated tracks associated with charged particles. It is divided into three independent modules in order to provide the optimal event reconstruction over a large solid angle: The Central Tracking Detector (CTD) covers the angular range between 22° and 165° and is complemented by Forward Tracker Detector (FTD) which is especially designed to track and trigger on tracks boosted in the forward direction in the angular region between 6° and 25°. The FTD is not used in the analysis presented in this thesis. The BDC and BST constitute the backward tracking detectors which provide an excellent identification

and measurement of the scattered electron in DIS events. They cover the angular range $153^o < \theta < 177.5^o$.
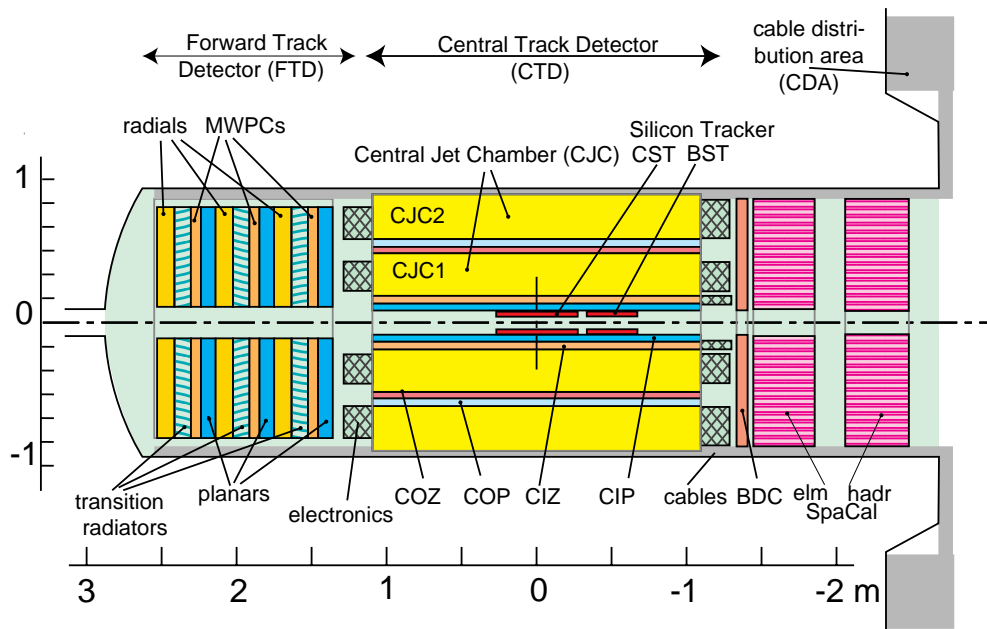
Figure 3.3: The H1 tracking detectors.

3.3.1 The Central Tracking Detector

The main components of the CTD are the two concentric drift chambers CJC1 and CJC2 [30]. Their sense wires run parallel to the beam-pipe to give a measurement of r and φ coordinates with a spatial resolution of 170 μm in the $r - \phi$ plane and a resolution on z of 22 mm from charge division by reading both ends of the wire. Each drift cell is inclined by 30° to the radial direction so that ionization electrons drift almost perpendicular to high momentum tracks. A better resolution in z of 260 μm is obtained with the Central Inner Z-Chamber (CIZ) [31] and the Central Outer Z-Chamber (COZ) [32]. They both have their sense wires oriented perpendicular to the beam-pipe. Fast tracking information for triggering purposes is provided by two multi-wire proportional chambers with wires parallel to the z-direction: the Central Inner Proportional Chamber (CIP) and the Central

Outer Proportional Chamber (COP) [33]. This can be achieved with their high time resolution and fast response.

3.3.2   The Backward Drift Chamber

The BDC [34] is positioned in front of the SpaCal calorimeter and covers a similar angular range $153^o < \theta < 177.5^o$ in for collision at the nominal vertex position. It is designed to determine the polar angle of the scattered electron in DIS from precise track information. It consists of four double-layers mounted along the z direction and divided into eight azimuthal sectors. Each sector consists of 32 drift cells with sense wires strung perpendicular to the beam axis. At small radii, the height of the cells is smaller than at large radii because the background rate increases considerably in the region close to the beam-pipe. The double layers are rotated by 11.23^o with respect to one another for the estimation of the azimuthal angle. In each double-layer, the cells of one layer are also radially shifted by half a cell width with respect to the other layer to resolve the left-right ambiguity.

The BDC hits that are closest to an electron track prediction are combined to form a track segment. The prediction is obtained from the positions of the vertex and the electron energy cluster in the SpaCal. The average resolution for the polar angle is 0.57 mrad [35].

3.3.3   The Backward Silicon Tracker

The dead material (electronics and cables of the CTD) in front of the BDC affects the resolution of the polar angle of the scattered electron. The BST [36] is positioned close to the CST (see figure 3.3), and it consequently provides a better measurement of the electron, but over a limited acceptance compared to the BDC. It also supplements the vertex reconstruction at low and high y where the particles escape the CTD acceptance.

The description that follows corresponds to the configuration of the years 1998-2000. The BST (see figure 3.4) is divided into the BST1 and BST2 sub-detectors each consisting of four wheels of Silicon detectors. The BST1, the farthest from the interaction point, is separated from the BST2 by the read-out electronics of the latter. Each wheel is composed of 16 modules of silicon detectors with r-strips (radial strips) arranged concentrically around the beam-pipe. The modules possess a trapezoidal shape with inner and outer radii $r = 5.9$ cm and $r = 12.04$ cm, respectively. Eight additional ϕ strip modules equip each wheel. Further details on the electron identification procedure will be given in section 4.5.
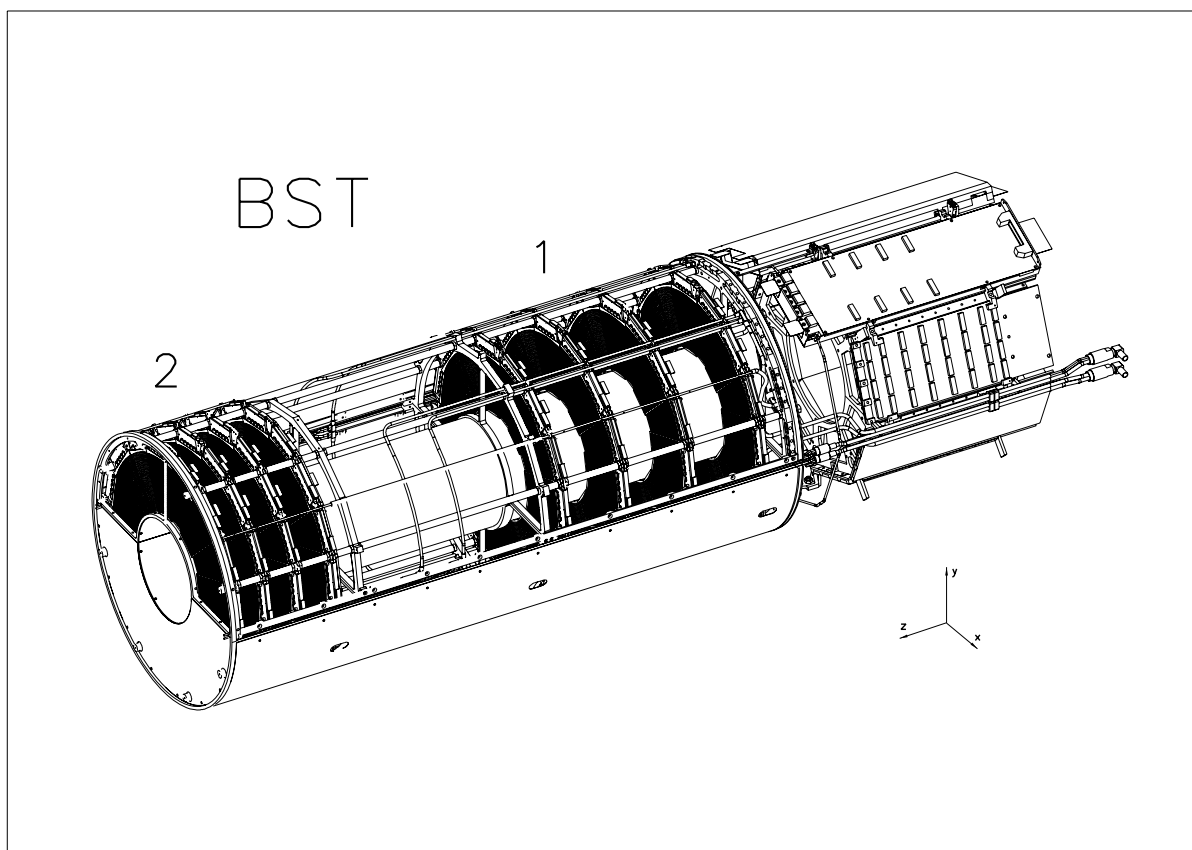
Figure 3.4: Schematic view of the BST detector.

3.4   Calorimetry in the H1 Detector

3.4.1   The Liquid Argon Calorimeter

The LAr calorimeter [29] provides a continuous and hermetic coverage for polar angles from 4° up to 154°. The purpose of the LAr [2] is to measure final states hadrons at all Q^2 and scattered electrons in very high Q^2 (>100 GeV^2). The calorimeter is divided into 8 wheels in z, each of which is further segmented into eight ϕ octants. The six central wheels are split into an inner electromagnetic section (EMC) and an outer hadronic section (HAC). The forward wheel comprises only an hadronic section whereas to the most backward wheel has only an electromagnetic section. The EMC consists in a succession of 2.4 mm thick lead absorbing plates and 2.35 mm thick layers of LAr. It has a total thickness of 20 to 30 radiation lengths for electrons and 1 to 1.4 interaction length for hadrons. The HAC is composed of 19 mm thick lead absorber plates with a double gap of 2.4 mm LAr providing an additional 5 interaction lengths for the absorption of hadrons. The orientation of the absorber plates was chosen to maximise the path length of the particles and is represented on figure 3.5. The energy resolution of the EMC and HAC are $\frac{\sigma(E)}{E} \sim \frac{0.11}{\sqrt{E(GeV)}} \oplus 0.01$ and $\frac{\sigma(E)}{E} \sim \frac{0.50}{\sqrt{E(GeV)}} \oplus 0.02$ for charged pions in test beams [37].

3.4.2   The Spaghetti Calorimeter SpaCal

The SpaCal [38], as with the LAr, is also divided into electromagnetic and hadronic sections. The Spacal is a very compact high resolution lead/scintillating fibre calorimeter that provides a coverage of the region close to the beam-pipe in the θ-range from 153° to 177.5^o, corresponding to Q^2 values in the range $1 \leq Q^2 \leq 120$ GeV^2. The electromagnetic section comprises 1192 cells of dimension 40.5 x 40.5 mm^2 with a depth of 250 mm

---

[2]Liquid argon was chosen for its stability and ease of calibration. The calorimeter's fine granularity yield high resolution and good eπ separation.
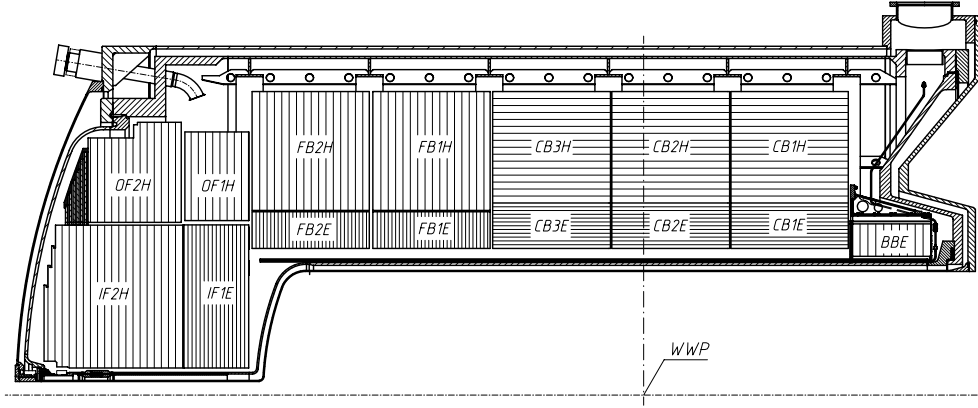
Figure 3.5: Side view of the LAr calorimeter with its absorber plates.

corresponding to 28 interaction lengths and one hadronic interaction length. The cell size is chosen to ensure a good electron-pion separation and a good position resolution. The basic unit of the calorimeter, a two-cell module, is made of 52 lead plates, each with 90 grooves hosting scintillating fibers with a diameter of 0.5 mm to provide a high sampling frequency which leads to an electron energy resolution, determined in test beam experiments, of $\sigma(E)/E = \frac{(7.1\pm0.2)\%}{\sqrt{E/GeV}} \oplus (1.0 \pm 0.1)\%$ [39]. The vertical and horizontal orientations of the 2-cell modules is depicted in figure 3.6 and is chosen to minimize the channeling effect. The innermost module is called the insert module which allows the identification of energy leakage from the calorimeter into the beam-pipe. The scintillation light of each cell is converted into electric pulses using photomultiplier tubes with a time resolution of about 1 ns, allowing strong suppression the non ep-background at the trigger level.

The structure of the hadronic calorimeter section is similar to the electromagnetic one with 136 cells of 12 x 12 x 25 cm^3 providing one nuclear interaction length with fibres 1 mm in diameter.
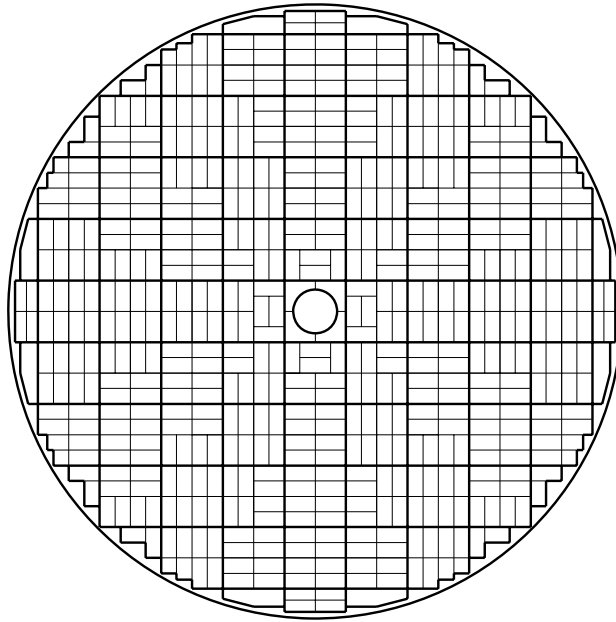
Figure 3.6: Cross-sectional representation of the SpaCal illustrating the orientation of its 2-cell modules and the insert.

3.4.3 The PLUG Calorimeter

The PLUG calorimeter [40] is designed to measure the energy flow in the forward region beyond the acceptance region of the LAr calorimeter (see figure 3.2). It covers the angular range 0.75^o to 3.4^o and has an angular resolution of 5 mrad. It is used here to distinguish between diffractive and non-diffractive events. The PLUG consists of nine copper absorber plates interleaved with eight sampling layers of Silicon. Its rather poor hadronic energy resolution of $\sigma(E)/E = 150\%/\sqrt{E/\text{GeV}}$ is the result of its incomplete shower containment and its coarse sampling.

3.5 The Forward Detectors

3.5.1 The Forward Muon Detector

The FMD [41], whose angular coverage is $3^o < \theta < 17^o$ corresponding to a pseudo-rapidity range of $1.9 < \eta < 3.7$, is situated beyond the return yoke of the solenoid magnet. It comprises three double layers of drift chambers located on either side of a toroidal magnet providing a magnetic field which varies from 1.75 T at the inner radius to 1.5 T at the outer radius. Four doubles layers have their wires strung tangentially around the beam-pipe to provide a measurement of the polar angle, and the other two have their wires strung radially for a measurement of the azimuthal angle. Charged particles leave pairs of hits in the double layers of drift cells which are linked with other pairs on the same side of the toroid to form track segments. Full tracks are reconstructed using the segments on both side of the toroid. The FMD is in fact a *spectrometer* to measure muons in the momentum range $5 < p < 100$ GeV. The lower bound is set by multiple Coulomb scattering, and the upper one is set by the minimum detectable track curvature in the magnetic field.

3.5.2 The Forward Tagger System

The Forward Tagger System consists of five planes of scintillator counters located at $z = 9$ m, 16 m, 24 m, 53 m and 92 m away from the nominal interaction point. Each layer, with the exception of the Proton Remnant Tagger at $z = 24$ m, is formed by four counters positioned as close as possible to the beam-pipe. The PRT comprises seven scintillators and covers a range in pseudo-rapidity of $6 < \eta < 7.5$. Each counter is made of two parallel plastic scintillators, each positioned on either side of a stainless steel layer. A 1 mm thick sheet of lead protects all the detectors against synchrotron radiation. The readout is performed with photo-multipliers.
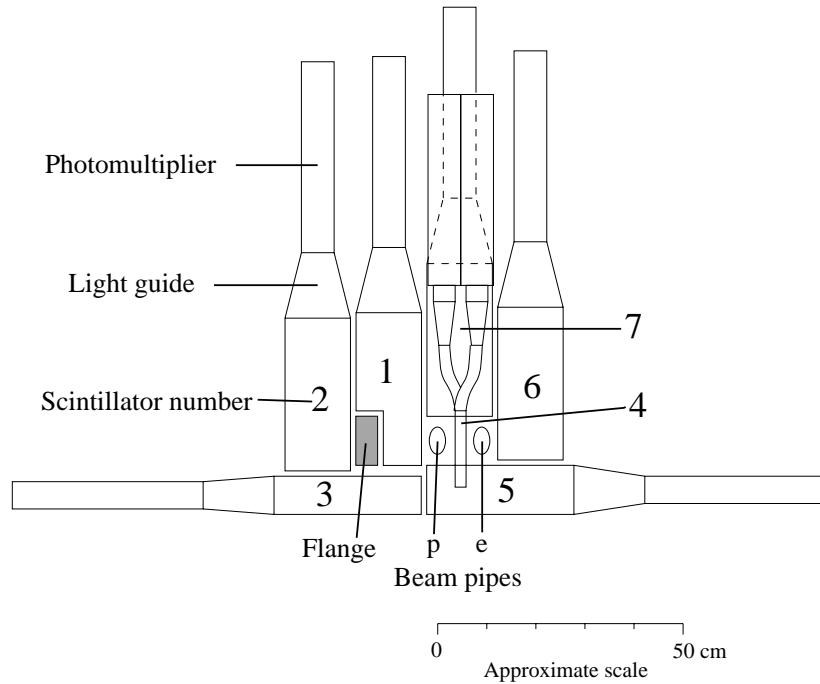
Figure 3.7: The seven scintillators constituting the PRT.

3.6 Triggering and Data Acquisition

3.6.1 Triggering

A high electron-proton collision rate is required in order to gather reasonable statistics for rare processes and high precision measurements. The entire detector cannot be read out during the 96 ns interval between successive bunch crossings because the signal formation in the slowest detector, namely the LAr calorimeter, takes 22 bunch crossings.

Therefore, H1 uses a four level trigger system in order to select the data of interest and to minimize the time during which the detector is inactive. The first two trigger levels, L1 and L2, consist of online hardware, while the fourth level trigger, L4, is a software running asynchronously with the earlier trigger levels [3].

At every bunch crossing, the L1 trigger system of each sub-detector sends eight or sixteen

---

[3]The third trigger level was not implemented during the HERA I running period.

bits of information, called trigger elements, to the central trigger. The central trigger makes 128 logical combinations of these trigger elements to form sub-triggers. In total, it takes 24 bunch crossings before L1 provides a decision whether to keep or reject an event. To avoid dead-time, the full detector information is stored in front-end pipelines whilst the trigger information is being collected and processed. If at least one of the sub-triggers is validated, an L1 keep signal is broadcast to the sub-systems, the pipelines are frozen, rewound by 24 bunch crossings. The full detector read-out starts and dead-time begins. The L1 and further information is passed over to L2 which refines the L1 decision after 20 μs. L2 is divided into two sections, a topological trigger (L2TT) and a neural network (L2NN), each providing 16 trigger elements. These are combined with L1 sub-triggers to form L2 sub-triggers. When an L2 keep signal is issued, deadtime continues until the complete detector information is read out and transfered to the central event builder of the fourth triggering level within 800 μs. The pipelines are then cleared and the dead time stops. A series of physics algorithms are run asynchronously at L4 to further reject remaining background events. About 1% of the rejected events are retained for monitoring and calibration purposes. The L4 farm processes events at a rate of up to 45 Hz. After data taking, the data are reprocessed using the full calibration of the various detectors and the optimised tracking information.

The trigger rates for soft processes can be as large as a few kHz whereas the rates for rare signatures can be much lower than 1 Hz. In order to maximise the efficiency of the data taking, the L1 sub-triggers associated with abundant events are not validated until their sub-trigger conditions has been satisfied a fixed number of times equal to their sub-trigger pre-scale. The pre-scales are adjusted regularly as a function of the beam conditions during a luminosity fill [4].

---

[4]A luminosity fill is the period of time extending from the moment HERA announces luminosity until one or both beams are dumped.

3.6.2 The Triggers of the 1999 minimum Bias Data Taking

The 99 minimum bias (99MB) data taking was fully devoted to the study of the region of the kinematic phase space with $Q^2 < 12$ GeV^2. The electron and proton beams energies were 27.5 GeV and 920 GeV, respectively.

There are three sub-triggers, namely s0, s3 and s9, designed for the identification of DIS events with Q^2 up to 150 GeV^2 which are characterised by the presence of the scattered electron in the SpaCal. Each of these sub-triggers contains an Inclusive Electron Trigger element (IET). There are three IET triggers, each corresponding to a specific electron energy threshold in the SpaCal (see table 3.1).

Trigger Element (Inner Region)	Trigger Element (Outer Region)	Energy Thresho ld
SPCLe_IET_cen1	SPCLe_IET>0	2 GeV
SPCLe_IET_cen2	SPCLe_IET>1	5 GeV
SPCLe_IET_cen3	SPCLe_IET>2	10 GeV

Table 3.1: The definitions of IET trigger elements for the 99MB data taking.

The electron energy is obtained by summing all the contributions deposited in 4 x 4 neighbouring electromagnetic calorimeter cells during the time of flight window of the *ep* interaction. To achieve the best efficiency, the sum is performed in overlapping windows with each window translated by a cell with respect to the previous one. The IET triggers are further divided into outer and inner region [5] triggers. The latter are known as IET_Cen triggers that are excluded from the definition of DIS sub-triggers under normal data taking. However, they were included in the minimum bias runs to give the best access to soft processes. The definitions of the s0, s3 and s9 sub-triggers are summarised in table 3.2, the timing and background trigger elements have been left out in the definition. s0 is the main sub-trigger of this analysis. It has a condition on the radial position of the electron cluster in the SpaCal to ensure reasonable trigger rates. s9 possesses the lowest energy threshold and is therefore used to access the highest y. It requires the existence

---

[5]The inner region is delimited by -16 $< x <$8 cm and -8 $< y <$ 16 cm.

of CJC tracks pointing towards the vertex region to limit the background. The lowest Q^2 values are reached with s3, which has the highest threshold energy of 10 GeV to limit the trigger rates.

Sub-trigger	L1	L2
s0	SPCLe_IET>1 or SPCLe_IET_cen2	$R_{\mathrm{SpaCal}} > 10$ cm
s3	SPCLe_IET>2 or SPCLe_IET_cen3	no requirement
s9	(SPCLe_IET>0 or SPCLe_IET_cen1) and 'good tracks'	no requirement

Table 3.2: The L1 and L2 definitions for the s0, s3 and s9 sub-triggers for the 99MB data taking.

Chapter 4

Event Selection

This chapter starts with the description of the Monte Carlos models used in the analysis. The global selection of events, that ensures the quality of the data used in the analysis, follows. It concentrates next on the procedure adopted to reconstruct the track of the scattered electron. It will be argued that using the BST and its associated electron finder constitutes the best method to measure precisely the electron polar angle and to determine the primary vertex position. The correct alignment of the electron detectors is particularly relevant to the precise reconstruction of the DIS kinematics. Both the alignment and the various kinematic reconstruction methods will be discussed. Before proceeding to the diffractive selection, the reliability of the inclusive sample must be demonstrated. This will be achieved with control distributions and with a comparison of the measurement of the inclusive reduced cross-section with published H1 data. The rest of this chapter is devoted to the diffractive event selection which is based on the rapidity gap method.

4.1 Monte Carlo Models

The physical processes under investigation are modelled with a combination of Monte Carlo generators in order to describe all aspects of the data, including the background. The events generated with the Monte Carlo programs are subjected to a full simulation of the detector response. The reconstruction of the Monte Carlo events using the same tools as for the data provides the modelling of experimental resolutions, efficiencies and acceptances that is necessary to correct the data for experimental bias.

The DJANGO Monte Carlo generator [42] is used to describe the inclusive positron-proton DIS interaction $ep \rightarrow eX$. $\mathcal{O}(\alpha_{\mathrm{em}})$ QED radiative corrections are simulated using an interface to the HERACLES program [43]. DJANGO is also interfaced to the LEPTO Monte Carlo generator [44] which provides the simulation of QCD radiation through the parton shower approach [45]. The fragmentation and hadronisation of quarks is simulated in JETSET [46] using the Lund String Model. The background at low Q^2, arising from hadrons produced in photoproduction being misidentified as electrons, is described by PHOJET [47], a Monte Carlo able to describe both elastic and inelastic processes in order to fully model high energy photon-proton interactions. The COMPTON [48] Monte Carlo program allows us to simulate events of the type $ep \rightarrow e\gamma X$ that arise from QED-Compton scattering and that can also enter the selected data sample.

The RAPGAP Monte Carlo generator [49] models diffractive DIS with an elastic proton. It relies on a LO QCD fit similar to the NLO fit described in section 2.5. Data from the publications [50] were used in the fit. The scattering off charm quarks in the diffractive exchange is generated separately from the scattering off u, d and s quarks. Meson exchanges occurring typically at values of $x_{I\!P} > 0.01$ are also described with RAPGAP. The simulations of QED and QCD radiation are performed using the LEPTO and ARIADNE [51] Monte Carlo generators, respectively. Inclusive diffraction can also be modelled according to the Saturation Model prescription described in section 2.7 with the SATRAP

Monte Carlo generator, which is based on RAPGAP.

The DIFFVM Monte Carlo generator [52] models the diffractive vector meson production observable in the data at the highest values of β. The vector mesons ρ, ω, φ and J/ψ are simulated in the framework of Regge phenomenology and the Vector Dominance Model [53–55]. Both elastic and diffractive proton dissociation are implemented in DIFFVM. This Monte Carlo is also used to account for the background arising when the proton dissociates into a low mass hadronic final state with $1.6 < M_Y < 5$ GeV, which is not modelled by either the RAPGAP or DJANGO programs.

4.2   Data Quality Selection

Before starting the DIS event selection, a pre-selection of the data is necessary to ensure the stable detector and background conditions for the experiment according to the following requirements:

- *Trigger phases*:

  At the beginning of a fill, the beam currents and the rate of background events are high. The SpaCal trigger pre-scales are consequently large, and the tracking detectors are progressively switched on, becoming fully operational after typically 10 to 20 minutes. The data recorded during this first phase is rejected due to the incomplete tracking and instability of the detector.

- *Run quality*:

  A fill is divided into a series of luminosity runs. Runs consist of a collection of events taken under very similar experimental conditions. They are classified as good, medium or poor. Poor runs are discarded because essential detector components, such as the luminosity system, the CJC or the LAr calorimeter, were not functioning correctly.

46

- *Detector high voltages and readout*:

  Additionally, the read-out and high voltages of the sub-detectors used in this analysis were required to be fully operational on an event by event basis. The relevant systems are the central tracking devices, the luminosity system, the LAr and SpaCal calorimeters, the BDC and the forward detectors (PRT, FMD). Further high voltage and read-out demands are imposed on the BST. The latest runs of the 99MB data taking were rejected due to problems with the BST.

The total integrated luminosity after this preliminary selection is 2.68 pb^{-1}.

4.3 Subtrigger Selection

The s0, s3 and s9 (see section 3.6.2) sub-triggers were specifically designed to cover different regions of the DIS phase space avalaible in the 99MB data taking. Whenever a sub-trigger fires on an event, a trigger weight, equal to the sub-trigger prescale, is assigned to this event. When more than one sub-trigger validates an event, the event weight is determined by the sub-trigger with the lowest prescale.

4.4 Electron Identification and Selection

The electron is identified by looking for the cluster with electromagnetic energy with the highest transverse momentum in the SpaCal calorimeter. This method is valid over the entire y and Q^2 ranges considered in this analysis. Once an electron candidate is found, further requirements are made which will be detailed later after the introduction of the cluster properties. The position of the electron cluster in the SpaCal is defined as the

weighted average over the positions of all calorimeter cells belonging to the cluster:

$$x_{clus} = \frac{\sum_{i=1}^{N} x_i w_i}{\sum_{i=1}^{N} w_i} \quad \text{and} \quad y_{clus} = \frac{\sum_{i=1}^{N} y_i w_i}{\sum_{i=1}^{N} w_i}, \tag{4.1}$$

where x_i and y_i are the coordinates of the geometrical centres of each cell i, and N is the total number of cells belonging to the cluster. Dead cells in the SpaCal and cells with high voltage problems are discarded in order to provide a high quality sample. The weight w_i of the ith cell is given by:

$$w_i = \max(0, w_{cut} + \ln(E_i/E_{clus})), \tag{4.2}$$

where E_i is the energy deposited in one cell, and E_{clus} is the cluster energy. w_{cut} is called the logarithm cut-off parameter, and its value is 4.85 for data and 5.15 for Monte Carlo. This logarithmic dependence of the weights is chosen because it closely matches the true transverse profile of the electromagnetic shower.

The z-position of the cluster is estimated using the following parameterization:

$$z_{clus} = 0.002 E_{clus} + 0.853 \ln(2479\, E_{clus}). \tag{4.3}$$

The estimator for the electron cluster radius, r_{clus}, is defined as the quadratic sum of the logarithmically weighted distances R_i between the centre of the cluster with coordinates (x_{clus}, y_{clus}) and the geometrical centre of the cell i:

$$r_{clus} = \sqrt{\sum_{i=1}^{N} (R_i w_i)^2}. \tag{4.4}$$

The radius of clusters whose origins are hadronic particles is larger than the shower radius of electrons, and the cut $r_{clus} < 3.5$ cm therefore discriminates against the photo-production background. Misidentified hadrons are also eliminated by demanding that the

scattered electron energy is larger than 5 GeV. The cut $E_h < 0.5$ on the energy deposited in the hadronic part of the SpaCal within a cone behind the electromagnetic cluster also gets rid of hadrons faking an electron signal.

The innermost region of the SpaCal corresponds to a region of very high background rates, but is also populated by the events with the lowest values of Q^2 which are of most interest to this analysis. The cut, on the distance R_{SpaCal} of the electron cluster from the beam axis, 10 cm $< R_{SpaCal} = \sqrt{x_{clus}^2 + y_{clus}^2} < 67$ cm is the best compromise between keeping the events of interest and background suppression. The upper and the lower bounds also ensure that the electron track (see section 4.5) candidates within the BST lie within the the SpaCal acceptance, namely $156^o < \theta'_e < 176^o$. Furthermore, the cut on the energy in the innermost 'veto' layer of the SpaCal $E_{veto} < 1$ GeV limits the energy leakage into the beam-pipe. Finally, a good matching between the track reconstructed in the BST with the SpaCal cluster reduces the contamination from neutral particle background (*e.g.* $\pi^0 \rightarrow \gamma\gamma$) with an energy deposition but with no associated track. The difference between the cluster radial position and the track extrapolated into the SpaCal, $\Delta R_{track-clus}$, is formed, and the cut $\Delta R_{track-clus} < 2$ cm is applied.

The electron cuts are summarised in table 4.1.

Cut	Main Purpose
$r_{clus} < 3.5$ GeV	removal of background from hadronic showers
$E > 5$ GeV	removal of the photoproduction
$E_h < 0.5$ GeV	and other fake electron background
10 cm $< R_{SpaCal} < 67$ cm	SpaCal acceptance cut
$E_{veto} < 1$ GeV	cut on energy leakage
$\Delta R_{track-clus} < 2$cm	suppression of neutral particles

Table 4.1: Summary of the cuts on the electron.

4.5   Reconstruction of the Electron Track

In previous F_2^D analyses [50, 56], the BDC was the sole detector used for the electron track reconstruction. As explained in section 3.3.3, the BST presents some advantages over the BDC, but over a restricted angular acceptance. As it is the first time the BST is used in a diffractive analysis, the principles of the BST track finding algorithm will be outlined in this section[1]. The electron track finding is divided into a pre-selection of hits, or pattern recognition, and the track finding itself.

4.5.1   BST Pattern Recognition

The sagitta,

$$\mathbb{S} = (r_i - r_{i-1}) + (r_{i+1} - r_{i-1}) \; \frac{(z_i - z_{i-1})}{(z_{i+1} - z_{i-1})}, \qquad (4.5)$$

is calculated from the hit coordinates r_i and z_i in three successive planes for all combinations of hits. If the hits are consistent with a straight line, a very good approximation of the electron track for the energy range considered in this analysis, the sagitta is compatible with zero. Non-null values of the sagitta indicate that the track is curved. Due to the high resolution and the very good signal to noise ratio of the BST (with a peak value at S/N∼ 13), a cut on a maximum value of the sagitta is sufficient for the pattern recognition.

---

[1]The full description of the BST electron finder is described in the appendix of [57]. The finder of this analysis only differs in the number of BST planes, eight instead of four, and the removal of the cut on the angular acceptance [58].

4.5.2 BST Electron Finder

Depending on whether a central vertex, reconstructed using the tracks in the CJC, exists or not, two different methods are used for the track reconstruction of the scattered electron in the BST.

- A central vertex exists:

  In this case, hits inside a corridor linking the electron cluster in the SpaCal to the central vertex are preselected. The diameter of the corridor is dictated by the radial resolution of the energy cluster. If two or more hits are found, a straight line fit is performed to determine the track parameters, and a refined selection of hits is performed. In the second iteration, the fit result is used to predict the hit positions instead of the line joining the cluster to the vertex. The width of the corridor is also reduced to 300 μm. The track angle and the BST vertex are finally calculated with a linear fit to the final hits.

- No central vertex exists:

  An iterative procedure is used, namely a Kalman filter [59], to select hits. The algorithm starts by connecting the centre of the cluster to the hits in the three closest planes to the SpaCal with a straight line. Each line is used to predict the radial position of the hits in the next plane. The closest hits in this plane to the interpolated hits are selected. Once two hits are found, the procedure is repeated using the two hits to find a third hit, etc. Among all the track candidates, the track with the maximum number of hits is chosen, and the same fit as in the central vertex case is performed to determine the track parameters.

The number of times a BST track is validated in data is compared with the Monte Carlo prediction in figure 4.1 a) after the inclusive analysis cuts. The photoproduction and QED Compton backgrounds were added to the Inclusive Monte Carlo. The electron polar
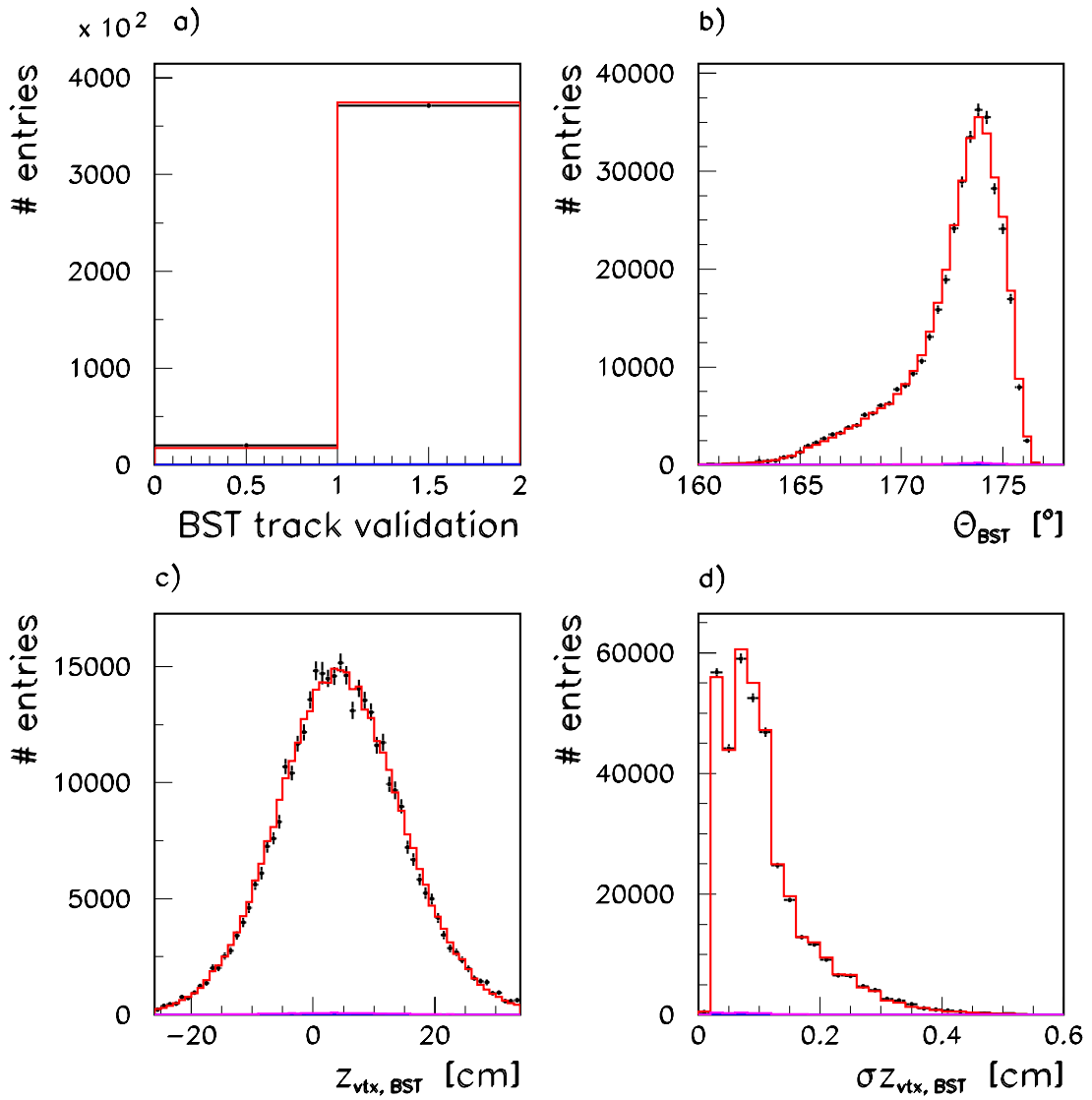
Figure 4.1: Comparison between data (points) and Monte Carlo (histograms) of the BST track validation flag, the polar angle and the vertex distribution and its error obtained with the BST finder algorithm. The (small) photoproduction and QED-Compton background contributions are also shown on the plots.

angle, the vertex position and the error on the vertex position obtained with the BST are plotted in 4.1 b), c) and d), respectively. There is a very good agreement between data and simulation.

4.6 Vertex Selection

A precise knowledge of the interaction vertex is essential for the identification and kinematic reconstruction of DIS events and the calculation of the detector acceptance. Several methods exist for the vertex determination. The most common approach uses the tracks in the CJC to give the so-called central vertices. As seen in the previous section, the origin of the track of the scattered electron reconstructed by the BST offers an alternative method for the vertex determination.

The phase space accessible with BST vertices is only constrained by the acceptance of this detector. This is illustrated in the (x, Q^2) kinematic plane shown in figure 4.2 where the isolines $\theta_e = 162^o$ and $\theta_e = 176^o$ delimit the SpaCal/BST measurement region. Central vertices are further constrained by the acceptance of the CJC to the phase space that lies between the isolines $\gamma_h = 22^o$ and $\gamma_h = 165^o$ when the BST is used for the electron measurement. If the vertex efficiency, studied in the next section, is taken into account, central vertices become unreliable below $y \sim 0.04$. BST vertices cover a much wider area a phase space, down to $y = 0.01$ in this analysis, and will therefore be selected. Furthermore, the error on the z coordinate of BST vertices is an order of magnitude smaller than the error on central vertices.

The vertex distribution obeys a Gaussian distribution to a good approximation. Its mean position, averaged over the 99MB data, is centered at $z_0 = 4$ cm in the H1 coordinate system and its width is approximately 10 cm. The z-position of the BST vertex, denoted by $z_{vtx,BST}$, is required to belong to the interval Δz defined by:

$$\Delta z \equiv (-26 < z_{vtx,BST} < 34 \text{ cm}) \tag{4.6}$$

This suppresses substantially the beam-gas and beam-wall interactions whose tracks do not point towards the vicinity of the primary vertex.
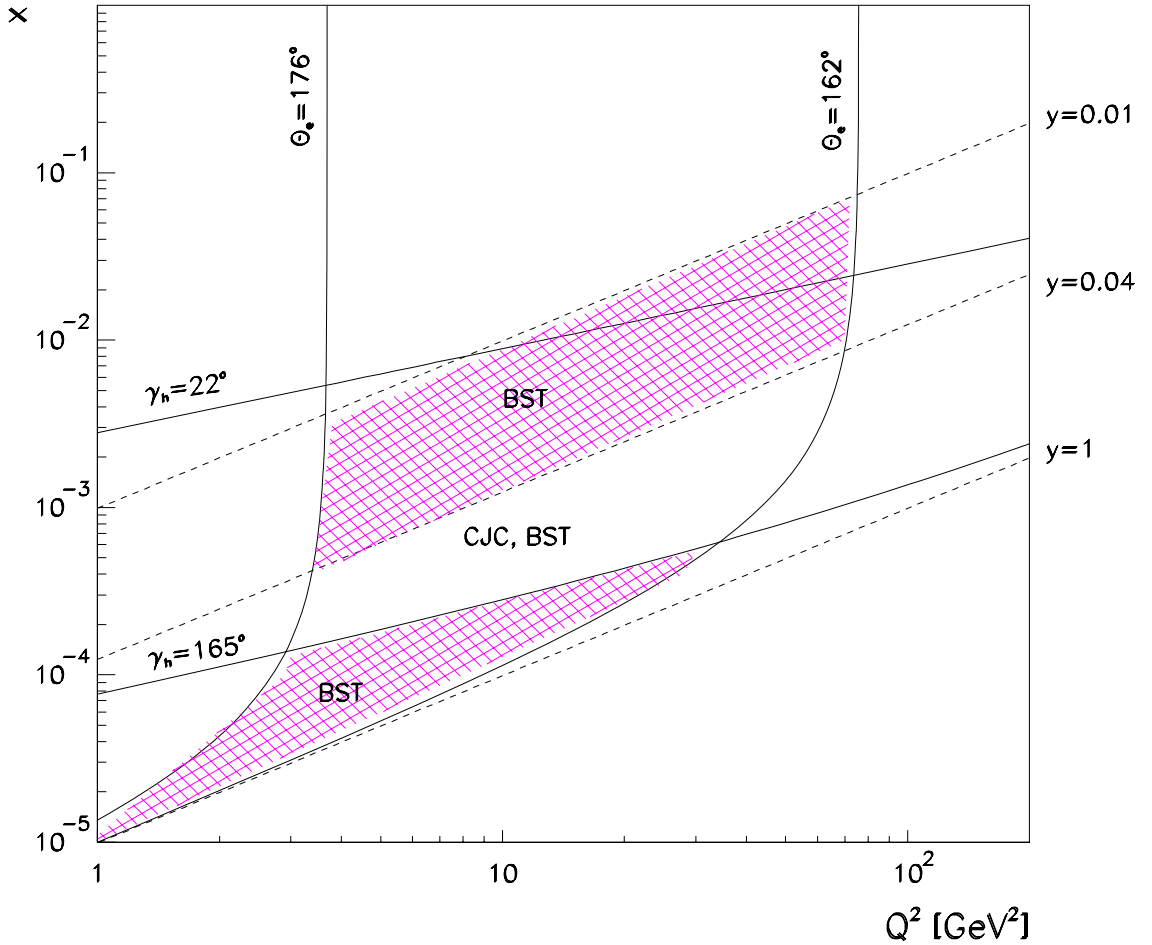
Figure 4.2: Representation of the kinematic plane illustrating the phase space accessible with central vertices, which is delimited by $y > 0.04$ and $\gamma_h < 165^o$. The electron measurement further restricts it to $162^o < \theta_e < 176^o$. The hatched regions show the additional phase space that is covered when BST vertices are used.

4.7 BST Track Reconstruction and Vertex Efficiencies

The precise reproduction of the efficiencies in data by the Monte Carlo simulation for the various sub-detectors is essential for the cross-section calculation (see section 5.1), as any disagreement between them will contribute to the error on the cross-section. The BST is the only new sub-detector used in the measurement of inclusive diffraction, and
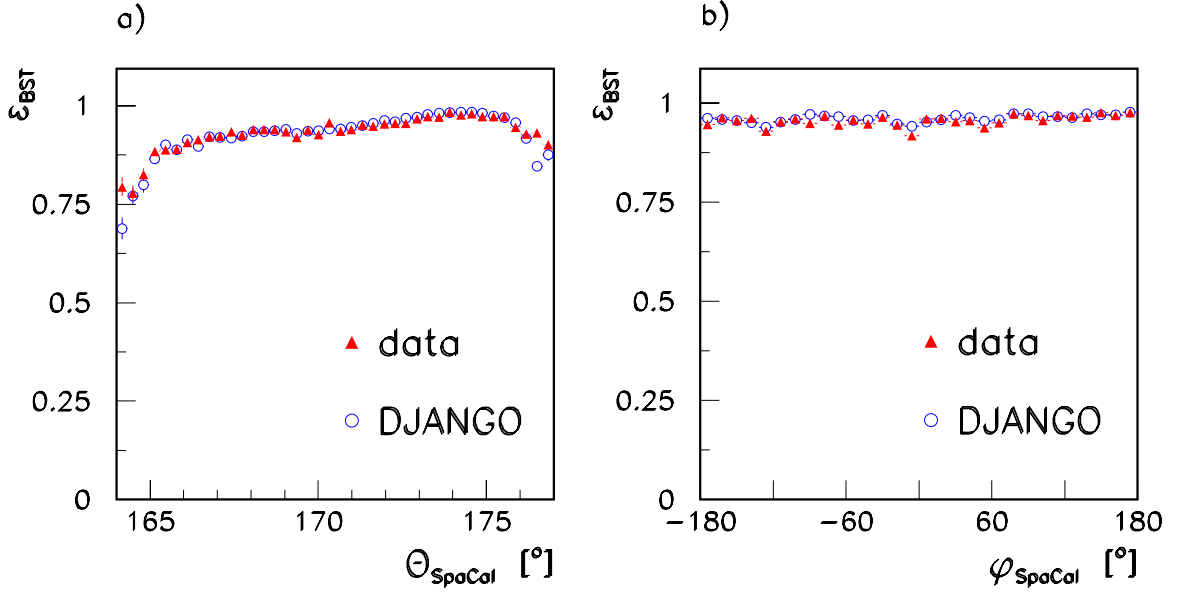
Figure 4.3: The BST efficiency expressed as a function of the azimuthal and polar angles measured with the SpaCal.

its efficiencies are investigated in the remainder of this section.

The efficiency to find a track is defined as the ratio of the number of DIS events with a clean high energy electron for which a BST track is found with a precisely reconstructed vertex to the total number of DIS events with a clean electron:

$$\epsilon_{BST} = \frac{\# \text{ events } (\exists vtx_{BST} \text{ AND } \sigma z_{vtx,BST} < 0.3 \text{ cm AND } E'_e > 20 \text{ GeV})}{\# \text{ DIS events with } E'_e > 20 \text{ GeV}}, \qquad (4.7)$$

where $\sigma z_{vtx,BST}$ denotes the error on the BST vertex position.

The efficiency as a function of the polar and azimuthal angles measured with the SpaCal is shown in figure 4.3. A good agreement is observed between the data and the inclusive DIS Monte Carlo, DJANGO, with an uncertainty of 1% over most of the phase space covered by the measurement.

The BST track information is used to determine the event vertex which plays a crucial role in the reconstruction of the event kinematics. The BST vertex efficiency is defined
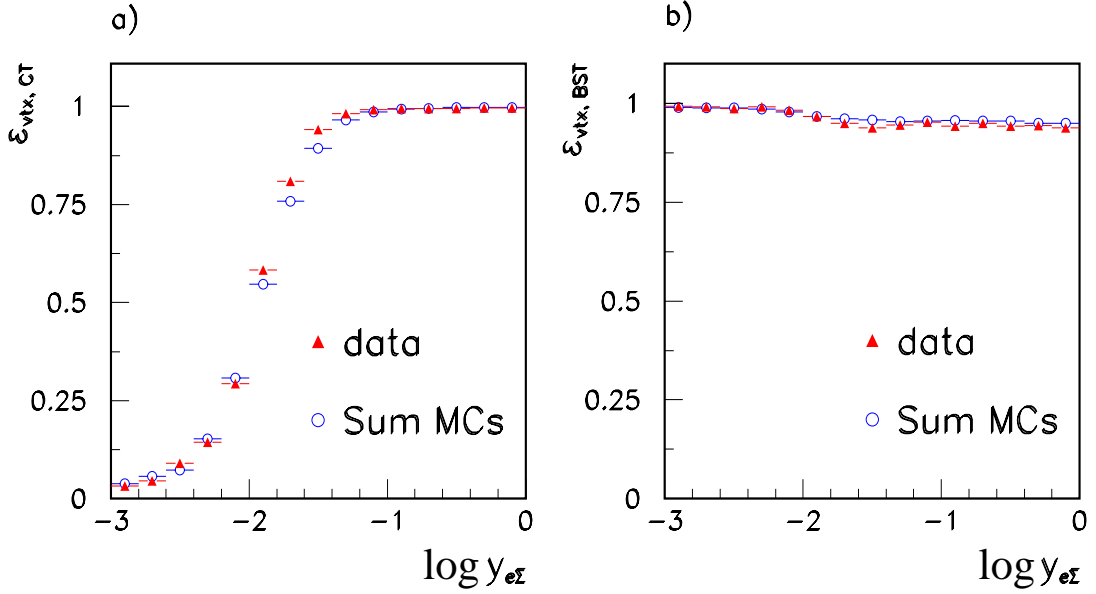
Figure 4.4: The efficiencies to find a vertex with the central tracker a) and the BST b) as a function of y calculated with the eΣ method. The data are compared with the sum of the inclusive DIS, photoproduction and QED-C Monte Carlo simulations.

as the ratio of the number of events reconstructed precisely by the BST with a vertex in the range Δz, defined in equation 4.6, to the total number of events in this range:

$$\epsilon_{vtx,BST} = \frac{\#\text{ events }(\exists vtx_{BST}\text{ AND }\sigma z_{vtx,BST} < 0.3\text{ cm AND in }\Delta z)}{\#\text{ events in }(\Delta z)}. \tag{4.8}$$

The PHOJET Monte Carlo simulation is used to model the background entering the sample at low electron energy. The vertex efficiency for both central and BST vertices is plotted in figure 4.4 as a function of y reconstructed with the e-Σ method [2]. The plot in figure 4.4 a) illustrates the strong variation of the efficiency with y for central vertices. The efficiency drops for $y < 0.04$ ($\log(y) < -1.4$) when the hadronic final state starts to escape the CJC acceptance. This limits the phase space to the region $y > 0.04$ as discussed in section 4.6. When the BST electron track is used to define the vertex, the efficiency remains high over the entire y range as can be seen in figure 4.4 b).

[2] This method is discussed in section 4.9.

56

4.8   Global Event Properties

In an ideal and perfectly hermetic detector, the total $E - p_z$ of the electron and hadronic final states is equal to $2E_e$ ($= 55$ GeV) for neutral current processes. In reality, this quantity is smeared around its nominal value due to the finite detector resolution. In contrast, both initial state photon radiation and photoproduction events can lead to a reconstructed $E - p_z$ significantly lower than $2E_e$. In the first case, a photon with energy E_γ, usually emitted almost collinearly to the incident electron, escapes along the beam-pipe, and in the second scenario the scattered electron is outside the SpaCal acceptance. Therefore, the cut $E - p_z > 35$ GeV is imposed to suppress photoproduction background and reduce radiative effects. QED Compton events are removed using their typical signature which consists of two electromagnetic clusters nearly back to back in the azimuthal plane with no hadronic energy deposits in the very forward part of the LAr calorimeter.

4.9   Reconstruction of the DIS kinematics

The DIS variables can be fully reconstructed from two independent variables provided that the beam energies are known. In the case of QED initial state radiation, a photon generally escapes undetected along the beam-pipe. Consequently, the effective electron beam energy is unknown, and more than two variables are necessary for the kinematic reconstruction. Since both the electron and the hadronic final state can be measured with the H1 detector, several methods are available. They are reviewed in this section. Their region of applicability is also discussed.

4.9.1 Electron Method

In the electron method, the kinematics are reconstructed solely from the electron information as follows:

$$y_e = 1 - \frac{E'_e}{E_e} \sin^2 \frac{\theta_e}{2}, \tag{4.9}$$

$$Q_e^2 = 4 E_e E'_e \cos \frac{\theta_e}{2} \tag{4.10}$$

and

$$x_e = \frac{Q^2}{s y_e}, \tag{4.11}$$

where E_e and E'_e are the energy of the incident and scattered electron, respectively. θ_e denotes the polar angle of the scattered electron. This method is very sensitive to initial state radiation because it directly depends on E_e. The resolutions on y_e and Q_e^2 are given by:

$$\frac{\delta y_e}{y_e} = \left(1 - \frac{1}{y_e} \right) \frac{\delta E_e}{E_e} \oplus (\frac{1}{y_e} - 1) \cot(\theta_e/2) \delta\theta_e \tag{4.12}$$

and

$$\frac{\delta Q_e^2}{Q_e^2} = \frac{\delta E_e}{E_e} \oplus \tan(\theta_e/2) \delta\theta_e, \tag{4.13}$$

where $\oplus$ is defined by $x \oplus y = \sqrt{x^2 + y^2}$. The resolution on y decreases with decreasing y. For $y \lesssim 0.15$, kinematic reconstruction methods using both electron and hadronic quantities are more accurate. The precision on the reconstruction of Q^2 relies on the accurate measurement of the electron angle. This also illustrates the necessity of the BST to achieve the best measurement of the inclusive cross-section.

4.9.2 Hadron Method

Two hadronic quantities are usually defined. The transverse momentum of the hadrons, p_t^h, and $\Sigma = E^h - p_z^h$. The latter is minimally affected by losses along the beam-pipe in the forward direction. Such losses are always very large due to the proton remnant. The kinematics are reconstructed from the following equations:

$$y_h = \frac{\Sigma}{2E_e}, \tag{4.14}$$

$$Q_h^2 = \frac{p_{t,h}^2}{1 - y_h} \tag{4.15}$$

and

$$x_h = \frac{Q^2}{s y_h}. \tag{4.16}$$

The resolution on Q^2 is given by:

$$\frac{\delta Q_h^2}{Q_h^2} = \frac{2\delta p_{t,h}}{p_{t,h}} \oplus \frac{y_h}{1 - y_h} \frac{\delta y_h}{y_h} \tag{4.17}$$

Hence, the resolution on Q^2 decreases for large values of y, and the hadron method is best used for measurements at low and medium y. In addition, the hadronic final state variables p_t^h and Σ are intrinsically less well reconstructed than the electron quantities E_e' and θ_e. Methods combining both hadronic and leptonic information are therefore better suited to the kinematics of neutral current processes over a wide range in y.

4.9.3 Sigma method

The Sigma method is based on three independent variables and is by construction insensitive to initial state radiation. Losses along the beam-pipe are minimised for the

reconstruction of y by replacing the electron energy in equation 4.14, with the total $E - p_z$ of the event, since $2E_e = (E - p_z)$ from energy conservation. The reconstruction of Q^2 uses the p_t of the electron. It is hence independent of collinear QED initial state radiation. The expressions for the reconstruction of y, Q^2 and x are:

$$y_\Sigma = \frac{\Sigma}{\Sigma + E(1 - \cos\theta_e)}, \tag{4.18}$$

$$Q_\Sigma^2 = \frac{E^2 \sin^2\theta_e}{1 - y_\Sigma} \tag{4.19}$$

and

$$x_\Sigma = \frac{Q^2}{sy_\Sigma}. \tag{4.20}$$

At high y, the scattered electron angle is large, and the errors on Σ largely cancel out between the numerator and the denominator in y improving the resolution with respect to the hadron method.

4.9.4   eΣ Method

The eΣ method combines the best reconstruction of x attained with the Σ method and the precision of the Electron approach for the reconstruction of Q^2. It reconstructs the variables using:

$$x_{e\Sigma} = x_\Sigma, \tag{4.21}$$

$$Q_{e\Sigma}^2 = Q_e^2 \tag{4.22}$$

and

$$(4.23)$$

$$y_{e\Sigma} = \frac{Q_{e\Sigma}^2}{s x_{e\Sigma}}. \qquad (4.24)$$

$$(4.25)$$

4.9.5 Double Angle Method

As it names suggests, the Double Angle Method uses the electron and hadronic angles. It does not rely on any energy measurements, and it is thus very useful for calibration purposes. The angle of the final state hadrons γ is given by:

$$\cos\gamma = \frac{p_{t,h}^2 - \Sigma^2}{p_{t,h}^2 + \Sigma^2}, \qquad (4.26)$$

from which the following kinematic variables can be obtained:

$$y_{DA} = \frac{\tan(\gamma/2)}{\tan(\theta_e/2) + \tan(\gamma/2)} \qquad (4.27)$$

and

$$Q_{DA}^2 = 4E_e^2 \frac{\cot(\theta_e/2)}{\tan(\theta_e/2) + \tan(\gamma/2)}. \qquad (4.28)$$

x is again obtained with the relation $Q^2 = sxy$. This method is particularly useful for the low y and low Q^2 region of phase space where the electron angle is large and the hadronic angle small. This can be deduced from the expression of the Q^2 resolution:

$$\delta Q_{DA}^2 = \frac{y-2}{\sin\theta_e}\delta\theta_e \oplus \frac{-y}{\sin\gamma}\delta\gamma. \qquad (4.29)$$

4.9.6 Electron-Double Angle Method

y can be reconstructed as a combination of y_e and y_{DA} to exploit the precision of the electron method at high y and the precision of the Double Angle method at low y: The expressions for Q^2 given in equations 4.9 and 4.28, for the Electron and Double Angle methods, respectively, can be both re-arranged to yield $Q^2 = 4E_e^2(1-y)/\tan^2(\theta/2)$.

$$y_{eDA} = y_e^2 + y_{DA}(1 - y_{DA}), \tag{4.30}$$

$$Q_{eDA}^2 = \frac{4E_e^2(1 - y_{eDA})}{\tan(\frac{\theta_e}{2})^2} \tag{4.31}$$

and

$$x_{eDA} = \frac{Q_{eDA}^2}{sy_{eDA}}. \tag{4.32}$$

This method possesses the best overall resolution for inclusive diffraction, where the containment of the hadronic final state in the LAr calorimeter gives an improved resolution on the hadronic angle γ_h. This is the reconstruction method adopted for the diffractive measurement.

The relative resolutions of the eDA method and $e\Sigma$ method for the reconstruction of the diffractive kinematics are compared in section 5.2.1 in terms of their bin purities when using the binning of the diffractive measurement. High bin purities correspond to good resolutions since it is then less likely to reconstruct events outside the bin in which they were generated.

4.10 Alignment of the Electron Detectors

The BST track-finding algorithm requires the accurate alignment [3] of the BST and the SpaCal with respect to one another. As a cross-check of the alignment procedure and to ensure the consistency of the different available methods to measure the electron polar angle, the BDC is also precisely aligned with both the SpaCal and the BST.

The SpaCal is aligned with the Central Tracking Chambers which defines the H1 coordinate system. The electron tracks obtained with the central tracker and the SpaCal are used for this purpose. A clean lepton sample was used by selecting scattered electrons with an energy $E_e > 20$ GeV and by requiring the electron clusters to have a radius $R_{clus} > 30$ cm in the SpaCal. The alignment constants are then determined from a fit to the difference in polar angles measured with the central tracker (θ_{CT}) and with the SpaCal (θ_e), $\Delta\theta = \theta_{CT} - \theta_e$, using the following relation:

$$\Delta\theta = P_1 \cos(\varphi_e) + P_2 \sin(\varphi_e) + P_3. \tag{4.33}$$

The values of the P_1 and P_2 parameters obtained from the fit give the shifts Δx and Δy (see table 4.2) that have to be applied in the x and y directions, respectively. The third parameter P_3 provides the alignment constant Δz in the z direction. The alignment of the BDC follows a similar procedure. The alignment constants for both the SpaCal and the BDC are given in table 4.2.

The correctness of the alignment procedure of the SpaCal and the BDC with the CT is

---

[3] The reader is referred to [60] for a comprehensive discussion.

	Δx [cm]	Δy [cm]	Δz [cm]
SpaCal	-0.10	-0.42	-0.8
BDC	-0.03	-0.2	0.8

Table 4.2: Alignment constants for the SpaCal and BDC.
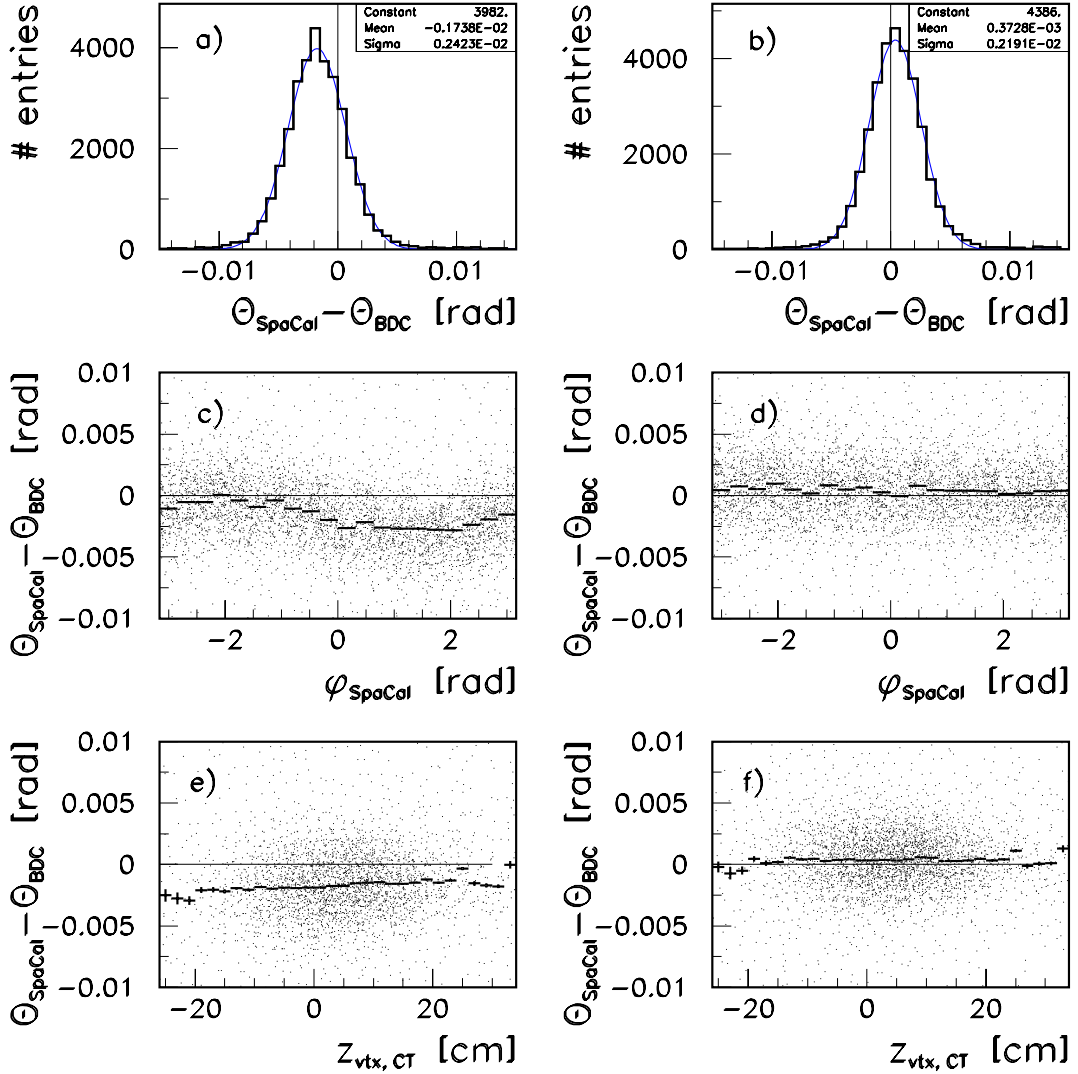
Figure 4.5: Check of the alignment of the SpaCal with the BDC using the difference in their θ coordinates. The left-hand plots are before alignment and the right-hand plots show the results of the alignment procedure. In plots c)-f), the average for each bin of the scatter histogram is also shown.

cross-checked with their relative alignment in figure 4.5. The left-hand plots a), c) and e) correspond to the non-aligned detectors. The right-hand plots b), d) and f) are after alignment.

In figure 4.5 a) and b), the difference in polar angle measurements between the SpaCal and the BDC is fitted with a Gaussian to exhibit the overall misalignment. It is 1.7 mrad
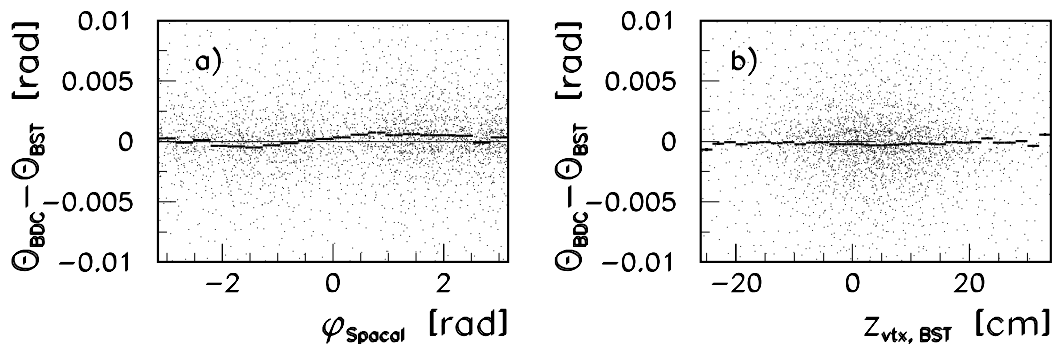
Figure 4.6: The correct alignment of the BDC with the BST is demonstrated in the two scatter plots where the difference in the BDC and BST polar angles are shown as a function of φ_{BDC} in a) and as a function of the z-vertex postion measured with the BST in b). The bin average of the profile histogram is also shown.

on average before alignment and around 0.4 mrad after alignment. The alignment in the transverse plane is checked by plotting $\Delta\theta_{Spacal-BDC}$ versus the azimuthal angle measured with the SpaCal. The characteristic trend of a sine curve due to a misalignment in the $(x-y)$ plane can be observed in the scatter plot of figure 4.5 c) where the average in φ bins of the scatter histogram is also represented. The profile histogram in 4.5 d) proves the improved alignment after correction of the detector positions. The original misalignment in z can be seen on figure 4.5 e) where the difference of polar angle is plotted this time as a function of the position of the vertex measured with the central tracker. The good alignment of the SpaCal and the BDC is corroborated in the plot 4.5 f).

The alignment of the BST is much more elaborate and an iterative procedure was followed. It consists of a series of internal alignments of the 8×16 r-detectors and of external alignments to the H1 coordinate system as defined by the CJC. The alignment constants for the BST were provided by the Inclusive Physics Working Group and the reader is referred [60] for a detailed discussion. The correct alignment is confirmed here with the plots of figure 4.6 where the difference between the polar angle measurements of the BDC and BST is shown as a function of the azimuthal angle measured with the SpaCal.

4.11   The Inclusive Control Sample

The objective of this section is to demonstrate the good level of understanding of the inclusive sample which is required to proceed to the diffractive analysis. Control distributions comparing data with Monte Carlo are first discussed. As explained in section 4.1, the DJANGO Monte Carlo is used to model the inclusive process. It is combined with the PHOJET and COMPTON Monte Carlos used for the description of the photoproduction and the QED Compton backgrounds. The control plots are followed by the measurement of the inclusive DIS reduced cross-section σ_r^{inc} which serves as an additional test of the quality of the inclusive event selection. Furthermore, it demonstrates the validity of the procedure followed for the $\sigma_r^{D(3)}$ cross-section extraction which is explained in chapter 5.

4.11.1   Inclusive Control Distributions

The electron energy distribution is plotted in figure 4.7 a). The description is reasonable in most bins. The discrepancy between data and Monte Carlo in the sharply falling edge of the electron spectrum is covered in the inclusive and diffractive measurements by assigning an uncertainty of 1.5% on the electron energy scale.

The electron calibration of the SpaCal with the kinematic peak method used in this analysis was performed in [61]. Alternative electron calibrations could provide a better description. However, as the error on the azimuthal angle of the the electron was dominant in [56], this thesis is focussed on the improvement of the detector alignment. The ratio E_{DA}/E_e (figure 4.7 b)) constitutes another calibration check. The distribution peaks near 1 as expected. The description of the data by the models is reasonable.

The p_t balance, defined as the ratio of the total transverse momentum of the hadronic system (p_t^h) to the transverse momentum of the electron (p_t^e) is an indicator of the consistency of the electron and hadronic calibrations. The y balance serves the same purpose.
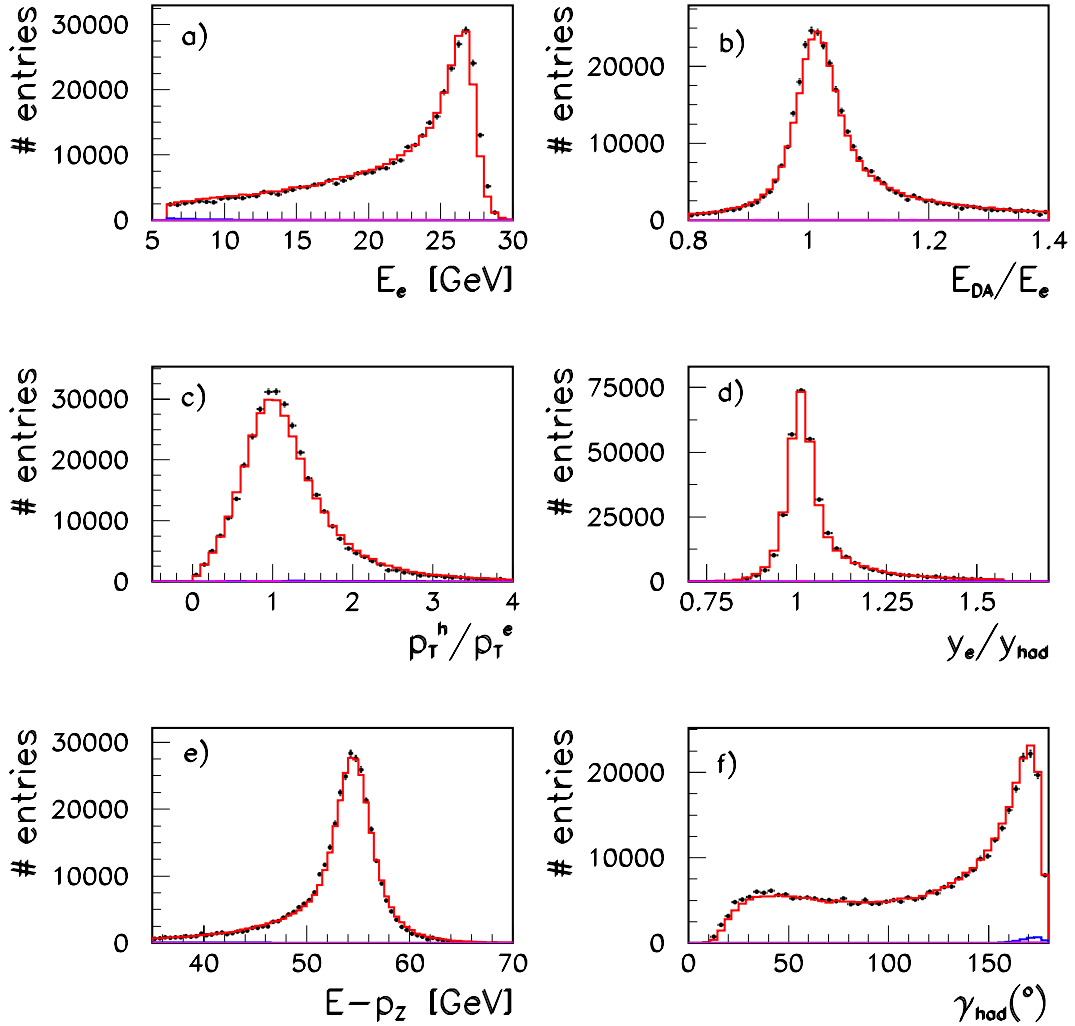
Figure 4.7: Inclusive Control Distributions.

They are shown in figures 4.8 c) and d) and a good description by the Monte Carlo model is observed. Good agreement between data and Monte Carlo can be observed for the $E - p_z$ distribution in the plot 4.8 e). The hadronic angle is the final quantity represented in figure 4.8 f). It corresponds to the angle of the scattered quark in the naive quark-parton model and is well described by the Monte Carlo.

The inclusive kinematic variables x, y and Q^2 reconstructed with the eΣ method are all displayed in figure 4.8. The simulation is in good agreement with the data overall.
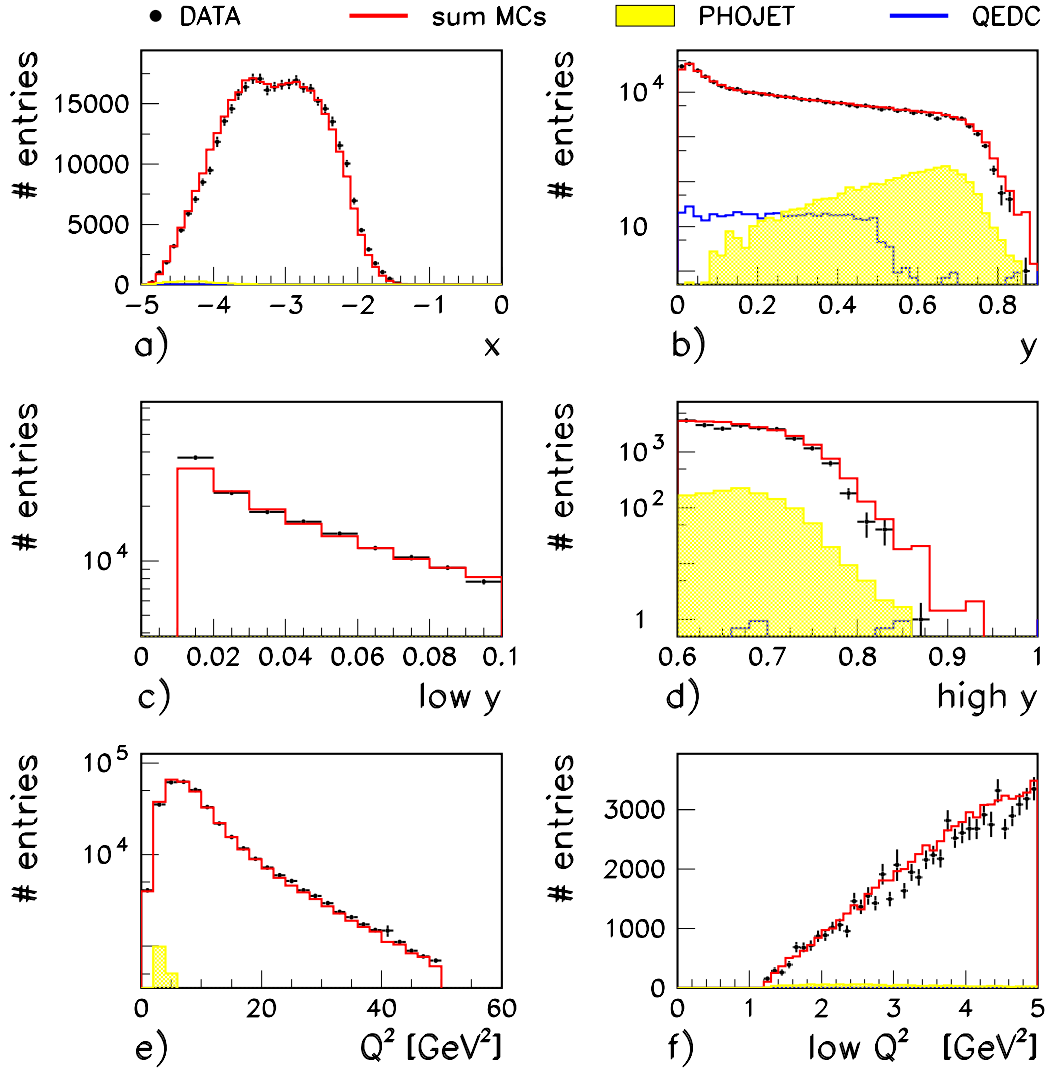
Figure 4.8: Inclusive kinematics control distributions.

However some small discrepancies can be observed at the edges of the available phase space.

4.11.2 Measurement of the Inclusive Reduced Cross-Section

The measurement of the inclusive DIS reduced-cross section is compared with the H1 published data [62] as function of Q^2 and x in figures 4.9 and 4.10, respectively. The
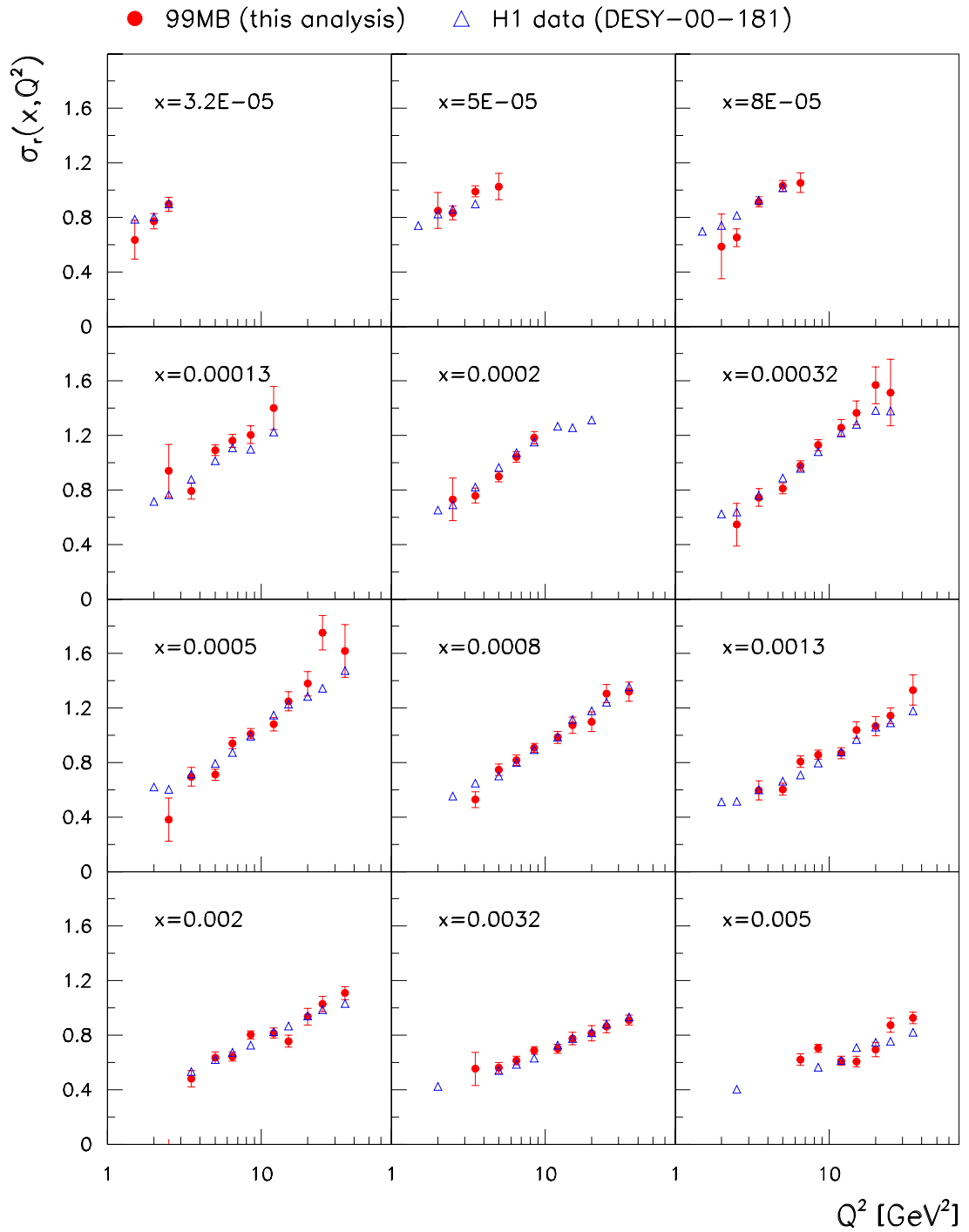
Figure 4.9: Comparison between the measurement of the inclusive-reduced cross-section performed in this work and the published 1997 data by H1. The cross-section is shown at fixed x values as a function of Q^2.
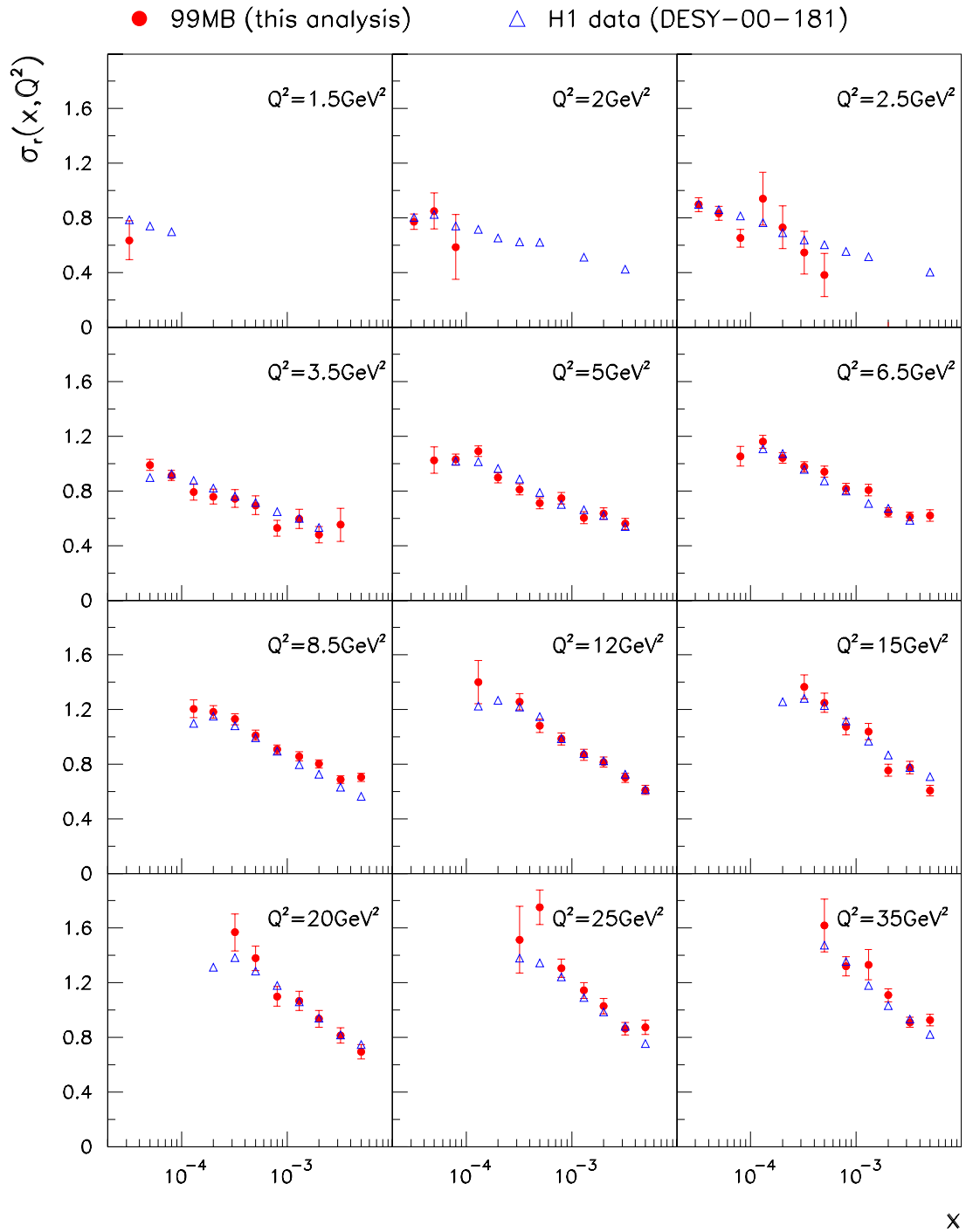
Figure 4.10: Comparison between the measurement of the inclusive-reduced cross-section performed in this work and the published 1997 data by H1. The cross-section is shown at fixed Q^2 values as a function of x.

binning in the variables x and Q^2 is similar to the one adopted in the H1 publication. The eΣ method was employed for the kinematic reconstruction whereas the best resolution was achieved in [62] with the Σ method for $y < 0.17$ and with the electron method at larger y values. All other aspetcs (bin centre corrections, radiative corrections,...) of the procedure used to obtain σ_r^{inc} are completely analogous to those described for the diffractive measurement in chapter 5. The overall agreement with the H1 published data is good.

4.12 Selection of Diffractive Events

In the H1 experiment, two complementary methods are available to select diffractive events. The first method uses the FPS to detect the scattered proton and measure its four-momentum which permits the measurement of the reduced diffractive cross-section $\sigma_r^{D(4)}(Q^2, x_{I\!\!P}, \beta, t)$ [63]. Unfortunately, this method suffers from relatively low statistics due to the the limited geometric acceptance and low efficiency of the FPS. A high statistics sample can be obtained using the rapidity gap method, which exploits the region of inactivity in the detector between the elastic or dissociated proton and the diffractively produced system X caused by the absence of any colour string connecting them. This selection is independent of the diffractive model implemented in the Monte Carlo simulation for generating diffractive events. Since the outgoing proton is not detected, the reconstruction of its four momentum is not possible, and hence the cross-section must be integrated over the variables M_Y and t. The latter method is used in the analysis presented here. The rapidity gap is imposed using the LAr and the Plug calorimeters, the Forward Muon Detector and the Forward Tagging System.

The LAr Selection

The most powerful selection criterion for diffractive events is based on a cut on the η_{max} variable, defined as the pseudo-rapidity of the most forward particle leaving an energy deposit in the LAr calorimeter exceeding 400 MeV. This threshold is chosen in order to reject noise whilst maintaining a high efficiency. Electronic noise exceeding 400 MeV can still lead to a loss of diffractive events resulting in a decrease of the diffractive selection efficiency. This effect is properly modelled in the Monte Carlo simulation of the detector.

The pseudo-rapidity of the most forward edge of the LAr calorimeter is around 3.4. The cut $\eta_{max} < 3.3$ constitutes the best compromise between the need to access the widest $x_{I\!P}$ range and the rejection of non-diffractive DIS background. The contamination of the sample is further reduced using the information provided by the Forward Muon Detector (FMD) and the Forward Tagging System (FTS).

Forward Muon Detector Selection

Beyond its design objectives, the FMD also serves to detect or veto on particles at very high pseudo-rapidities. For example, particles from the proton remnant with high pseudo-rapidities may scatter off the beam-pipe and collimators resulting in secondary particles which can be detected in the FMD. The three outer layers, beyond the toroid magnet, suffer from high hit counts due to the background arising from synchrotron radiation, and only the three inner layer on the main detector side of the toroid can be used. The pairing algorithm used within each layer in the normal track reconstruction is adapted to recognise tracks, in the three inner layers, originating from tracks associated with secondary scattering in the beam-pipe which possess a steeper angle than primary tracks.

Diffractive events are selected with the FMD by demanding no more than two hit pairs in its first two layers closest to the the interaction point and no more than two hit pairs

72

in the third layer:

$$N_{FMD1} + N_{FMD2} \leq 2 \quad \text{AND} \quad N_{FMD3} \leq 2. \tag{4.34}$$

This selection results in a fraction of diffractive events lost due to noise of 1.3%

The noise fraction was calculated using randomly triggered data. It is defined as the ratio of events with activity in the FMD but none in the LAr calorimeter to all randomly triggered events.

The Forward Tagging System Selection

The FTS permits the detection of activity from the proton remnant at the largest pseudo-rapidities. In contrast to the FMD, the random noise present in these scintillators is negligible, and diffractive events are selected by demanding no hit. However, the sixth layer of the PRT presented some high noise level in the early fills of the 99MB data taking, and it was therefore taken out of the selection. Due to the large discrepancies between data and Monte Carlo, the two most forward FTS stations cannot be used, and the selection is solely based on the PRT and the two FTS stations located nine and sixteen meters away from the interaction point. Hence, the following cuts on the number of hits, denoted by N, are applied:

$$\sum_{i=1}^{5} N_{PRT,i} + N_{PRT,7} = 0 \quad \text{AND} \quad N_{FTS_{1,2}} = 0. \tag{4.35}$$

The efficiency of the PRT, defined as the ratio of events which give a signal in the PRT over all DIS events, is too high in Monte Carlo. This is attributed to the failure of the simulation to describe the worsening of the response of the PRT with time as the high rates in the forward region provoke the rapid aging of the scintillators.
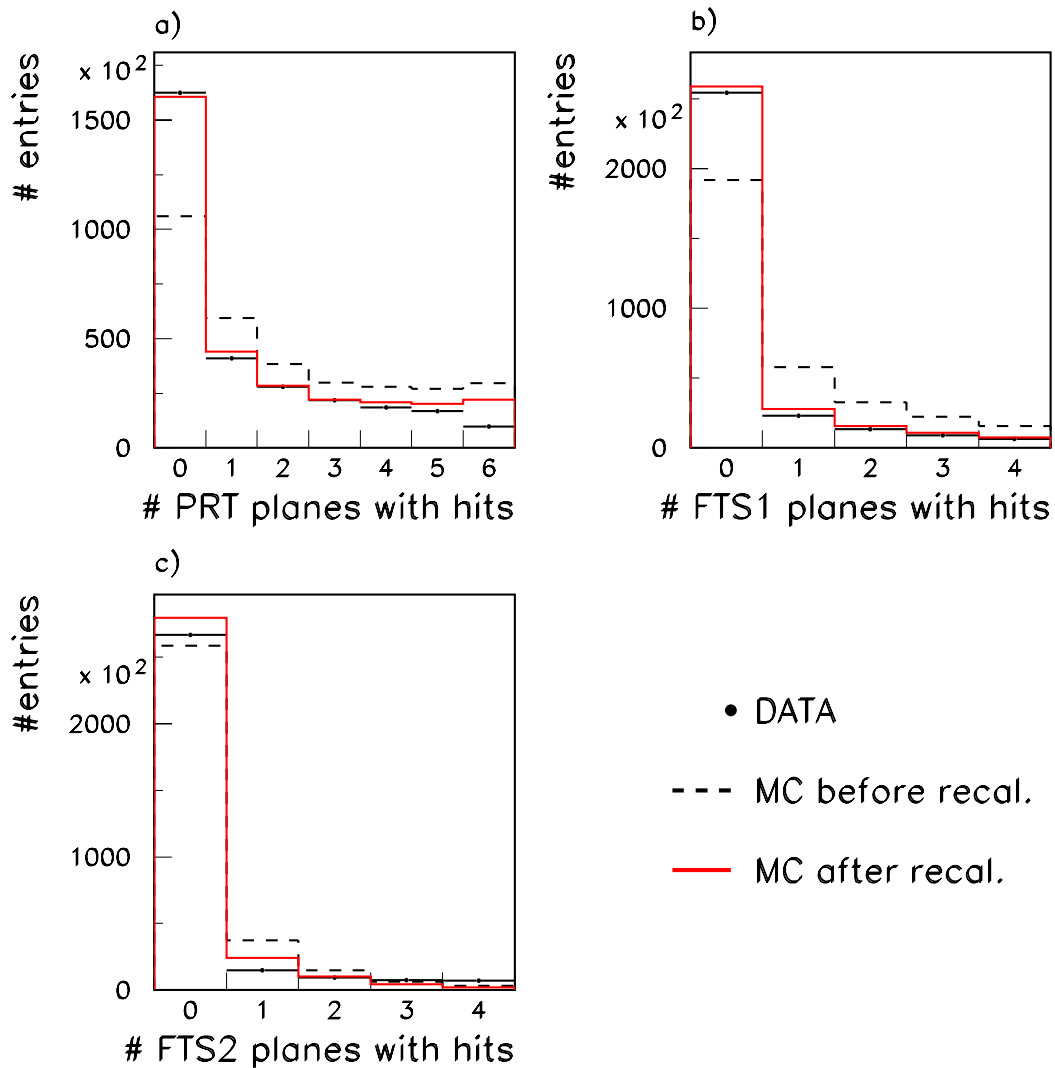
Figure 4.11: Comparison between data and Monte Carlo of the number of PRT and FTS planes with hits before and after the downgrading of the efficiency in the simulation.

The procedure adopted here for the correction of the Monte Carlo efficiency is based on the work presented in [61,64]. It consists in applying an overall downgrading factor to the efficiency of the stations in Monte Carlo. This choice, rather than to use individual factors for each PRT station, is motivated by the strong correlation between all the stations. The downgrading factor is obtained by forming the ratio of data to Monte Carlo for the global

PRT efficiencies defined by:

$$\epsilon_{PRT} = \frac{\# \text{ events} \left(\sum_{i=1}^{5} N_{PRT,i} + N_{PRT,7} > 0 \text{ AND anti}\right)}{\# \text{ DIS events AND anti}},$$ (4.36)

where 'anti' stands for anti-diffractive cuts that are defined as follows:

$$\text{anti} = \eta_{max} > 3.3 \text{ AND } N_{FMD1} + N_{FMD2} > 2 \text{ AND } N_{FMD2} > 2.$$ (4.37)

The anti-diffractive cuts are designed to select a sample of non-diffractive events in which activity in the acceptance region of the PRT and the FTS is to be expected from the proton remnant. Re-calibration factors are also needed for the FTS1 and FTS2. They are obtained using a similar method to that for the PRT and the resulting factors are summarised in table 4.3.

Detector	Re-calibration Factor
PRT	0.743 ± 0.002
FTS1	0.482 ± 0.002
FTS2	0.810 ± 0.004

Table 4.3: Probability with which activity is ignored in the Monte Carlo simulation for the PRT and FTS stations evaluated as described in the text. The errors quoted are statistical.

The improved description of the data by the simulation is illustrated in 4.11 where the distribution in the number of PRT planes with hits in Monte Carlo before and after downgrading is compared with data.

4.13 The Plug Calorimeter Selection

The Plug calorimeter helps to reject the background contributions at high $x_{I\!P}$. Events with energies above 5 GeV are rejected. The random noise present in the Plug is not included in the detector simulation. A correction factor was calculated in a manner similar to the

FMD. The total noise correction due to the FMD, PRT, FTS and Plug is $\sim 2\%$ for the 99MB data.

4.14 Summary of the Diffractive Event Selection

The diffractive selection is summarised in table 4.4.

Diffractive cuts
$\eta_{max} < 3.3$
$N_{FMD1} + N_{FMD2} \leq 2$ AND $N_{FMD3} \leq 2$
$\sum_{i=1}^{5} N_{PRT,i} + N_{PRT,7} = 0$ AND $N_{FTS_{1,2}} = 0$
$E_{Plug} < 5$ GeV

Table 4.4: Summary of the diffractive cuts.

4.15 Diffractive Control Distributions and Kinematics

Diffraction is modelled with the RAPGAP Monte Carlo generator discussed in section 4.1. The u, d, s and charm quark contributions to the diffractive scattering are shown and identified with the labels 'RAPGAP uds' and 'RAPGAP c' in the figures in this section. The contribution of meson exchanges, labelled with 'RAPGAP me', are also shown. The diffractive vector mesons entering the data sample are described with the DIFFVM programs. The DJANGO Monte Carlo is used here to model the inclusive non-diffractive background. The prescription of table 4.5 for the mixing of RAPGAP

MC	Phase-Space Restriction
DJANGO	$x_{I\!\!P} > 0.1$ OR $M_Y > 5$ GeV
RAPGAP	$x_{I\!\!P} < 0.1$ AND $M_Y < 1.6 GeV$

Table 4.5: Phase-space regions simulated with the DJANGO and RAPGAP Monte Carlos
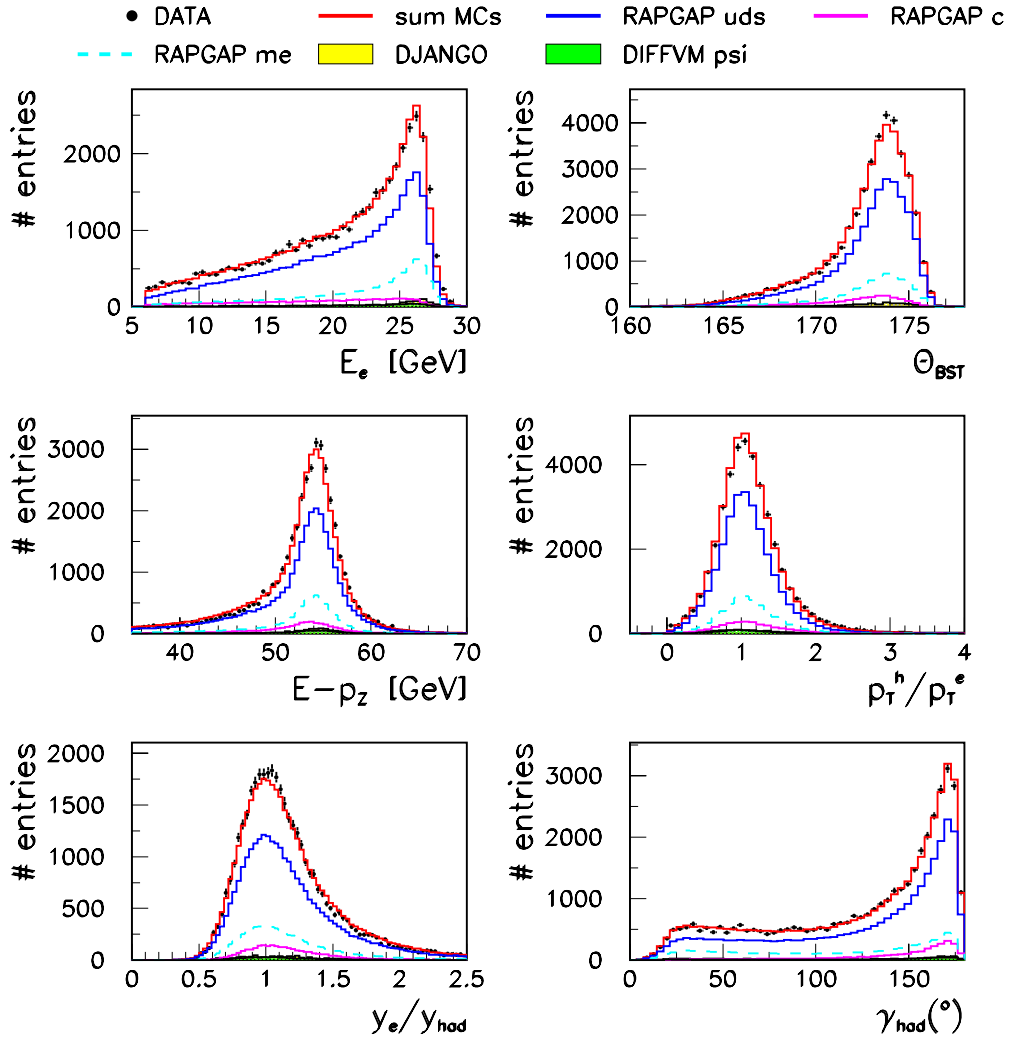
Figure 4.12: Control distributions, discussed in section 4.11.1 for the inclusive sample, are shown in the plots for the diffractive sample. The mixing of the Monte Carlo generators is explained in the text.

and DJANGO prevents their overlap in phase space. Unfortunately, the small admixture of double dissociation events $ep \rightarrow eXY$ is not simulated in either the RAPGAP or the DJANGO Monte Carlo program when the mass of the dissociated proton is in the range $1.6 < M_Y < 5$ GeV. To account for this, a correction factor is applied to the cross-section whose discussion is postponed to section 5.2.4. The remaining background from photoproduction and QED-Compton scattering is treated with the PHOJET and COMPTON simulations, respectively.
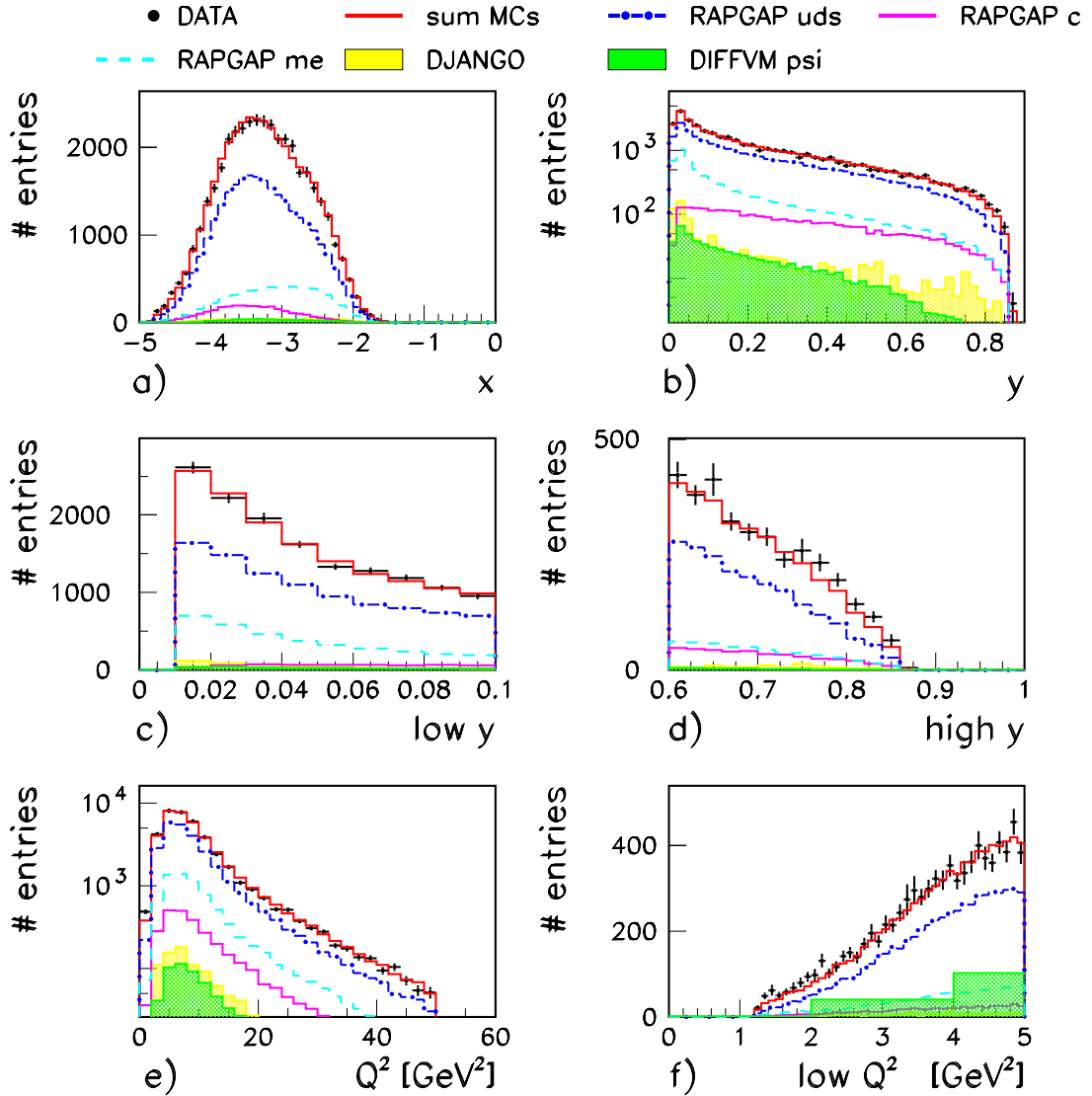
Figure 4.13: Inclusive kinematic variables reconstructed with the eDA metod after the diffractive selection, comparing data and simulation.

The same checks that were performed for the inclusive control sample are now reproduced, after the diffractive event selection, in the plots presented in figure 4.12. The good description of the $E - p_z$, p_T and y balance distributions (figure 4.12 c), d), e)) testify to the quality of the calibration. The electron and hadronic angles are also well reproduced by the simulation (figure 4.12 c), f)). The good description of E_e, shows further that the Monte Carlo simulation reproduces the basic features of the diffractive sample. A very good agreement between data and simulation has been achieved for the inclusive
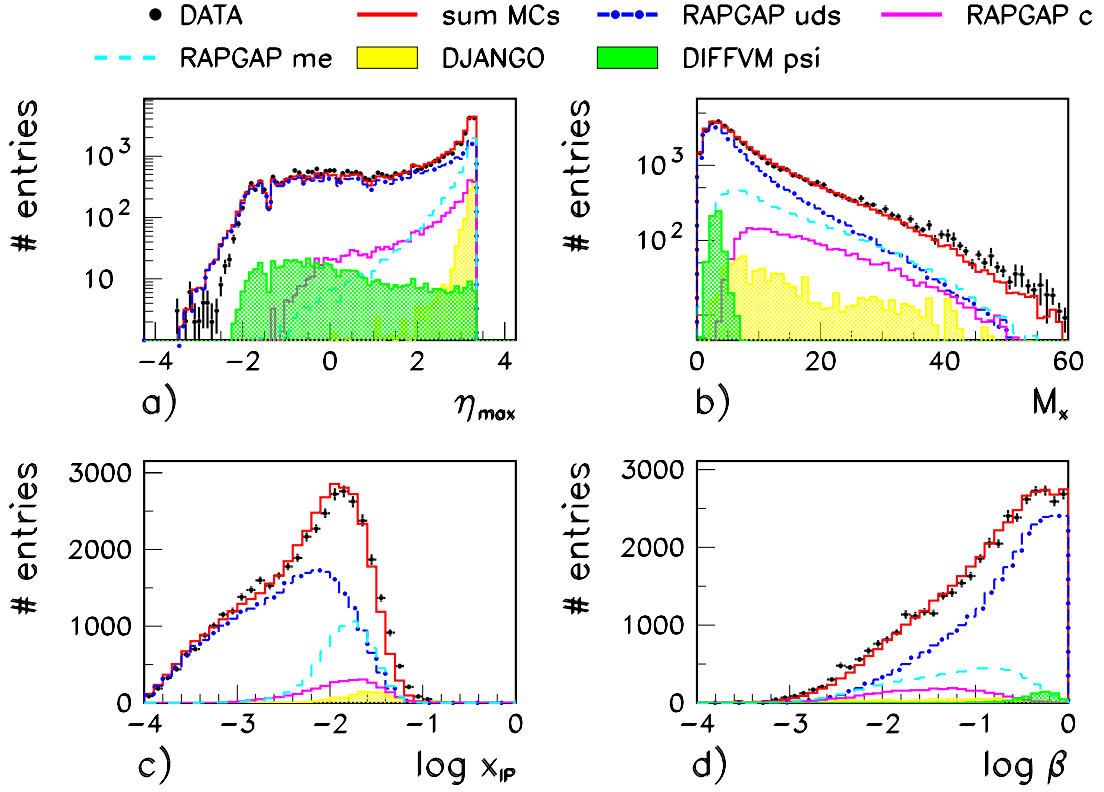
Figure 4.14: The pseudo-rapidity η_{max} of the most forward energy cluster in the LAr calorimeter and the diffractive quantities M_X, $\log x_{I\!P}$ and $\log \beta$ reconstructed with the eDA method after the diffractive selection.

kinematic variables x, Q^2 and y in the diffractive data (see figure 4.13) . In particular, the Monte Carlo very closely matches the data at low y. Accessing the low y region of phase space implies that a better diffractive measurement at high $x_{I\!P}$ can be made as can be seen from the following argument:

The $x_{I\!P}$ formula can be rewritten as:

$$x_{I\!P} = \frac{1}{sy\beta}Q^2 \geq \frac{1}{sy}Q^2, \qquad (4.38)$$

where the inequality holds because $\beta < 1$.

This inequality implies that as y decreases, higher $x_{I\!P}$ values can be accessed for any given value of Q^2.

79
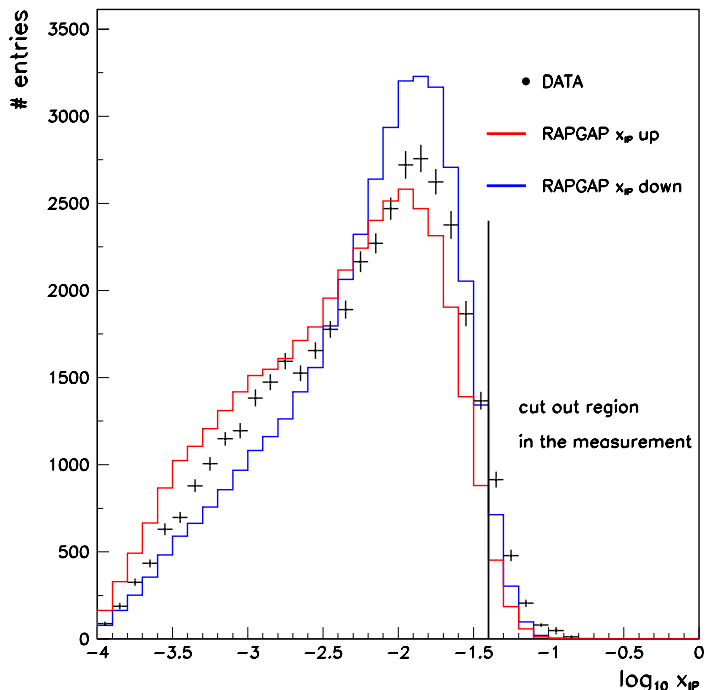
Figure 4.15: $x_{I\!P}$ comparison between data and the re-weighted RAPGAP simulation. The data are contained within the systematic error band up to the highest value of $\log x_{I\!P} = -1.4$ accessed in the measurement.

The RAPGAP Monte Carlo correctly describes the plateau in the pseudo-rapidity (η_{max}) shown in figure 4.14 a). The non-diffractive peak can be clearly seen at the high values of η_{max}. The mass of the hadronic final state M_X, plotted in figure 4.14 c), is reconstructed in a manner which benefits from the optimised reconstruction of y:

$$M_X^2 = (E^2 - p_x^2 - p_y^2 - p_z^2)_h \frac{y_{eDA}}{y_h},\qquad(4.39)$$

which was introduced for the first time in [23][4]. The energy and the momentum of the hadronic final state in equation 4.39 were obtained using an algorithm that combines SpaCal and LAr calorimeter cluster information with CJC track information and which avoids double counting. A scaling factor of 1.07 was also applied to the reconstructed M_X^2

---

[4]The hadronic final state mass squared can be rewritten as $M_X^2 = (E - p_z)_h(E + p_z)_h - p_t^2$ where p_t^2 is the transverse momentum squared of the hadrons. The $(E - p_z)_h$ quantity is very sensitive to losses in the backward direction. When M_x^2 is multiplied by y_{eDA}/y_h, the $(E - p_z)_h$ terms in M_X^2 and in y_h (see equation 4.14) largely cancel yielding an improved resolution on the hadronic mass.

variables to account for residual losses beyond the detector acceptance in the backward direction. The well reconstructed Q^2 and M_X^2 are utilised in the reconstruction of the diffractive variables $x_{I\!P}$ and β [5] shown in figure 4.14 c) and d). The Monte Carlo fails to fully describes the $x_{I\!P}$ distribution from the data. This is not unexpected since the phase space of the present measurement extends beyond the phase space covered by the data used in the fits upon which RAPGAP is based. The uncertainty in the Monte Carlo modelling of the $x_{I\!P}$ distribution is estimated by re-weighting the u,d and s and charm quark distributions in RAPGAP by $(1/x_{I\!P}^{\pm 0.2})$. Figure 4.15 shows the re-weighted $x_{I\!P}$ distributions compared to the data which lies within the uncertainty band for the $x_{I\!P}$ range considered in this analysis, namely $0.00016 < x_{I\!P} < 0.04$ $(-3.8 < \log x_{I\!P} < -1.4)$.

---

[5]The $x_{I\!P}$ and β variables were reconstructed using the formulae 2.2 and 2.3, respectively.

Chapter 5

Measurement of the Diffractive Reduced Cross-Section

The method used for the extraction of the diffractive reduced cross-section is first introduced. It is followed by the specification of the purity and stability criteria imposed on the binnings used in the measurement. The different corrections applied to the data are then discussed. Finally, the measurement is performed with another kinematic reconstruction method and another Monte Carlo generator in order to investigate the stability of the measured reduced diffractive cross-section.

5.1   Extraction of the Diffractive Reduced Cross-Section

Two three-dimensional binning schemes are used in the measurement of the diffractive reduced cross-section $\sigma_r(\beta, Q^2, x_{I\!P})$. In the first and main scheme, which is motivated by the need to test the QCD factorisation theorem, the data are binned in the Q^2, x and $x_{I\!P}$ variables. This choice is best suited for the investigation of the β and Q^2 dependences of the data at fixed values of $x_{I\!P}$. Relatively few $x_{I\!P}$ bins, namely five, are employed

to provide the high statistics necessary for a high precision measurement. The reduced cross-section $\sigma_r(\beta, Q^2, x_{I\!\!P})$ can be extracted from

$$\sigma_r^{D(3)}(\beta, Q^2, x_{IP}) = \frac{xQ^4}{4\pi\alpha^2(1 - y + \frac{y^2}{2})} \frac{\mathrm{d}^3\sigma_{ep \to eXY}}{\mathrm{d}Q^2\mathrm{d}x\mathrm{d}x_{IP}}, \tag{5.1}$$

once the differential cross-section $\frac{\mathrm{d}^3\sigma_{ep \to eXY}}{\mathrm{d}Q^2\mathrm{d}x\mathrm{d}x_{IP}}$ has been determined at a point in Q^2, x and $x_{I\!\!P}$.

The differential cross-section at the point $(Q_c^2, x_c, x_{I\!\!Pc})$ is experimentally obtained with:

$$\left.\frac{\mathrm{d}^3\sigma_{ep \to eXY}}{\mathrm{d}Q^2\mathrm{d}x\mathrm{d}x_{I\!\!P}}\right|_{(Q_c^2, x_c, x_{I\!\!Pc})} = \frac{(N_{data} - N_{bckgrd})}{\Delta V} \frac{BCC * RC}{\mathcal{L}} * \mathcal{C}_Y, \tag{5.2}$$

where $\Delta V = \Delta Q^2 \Delta x \Delta x_{I\!\!P}$ is the bin volume. N_{Data} is the number of events from the data observed in the bin $(\Delta Q^2, \Delta x, \Delta x_{I\!\!P})$ centred around the point where the cross-section is evaluated. The number of background events, N_{bckgrd}, remaining in the data sample after the diffractive selection is estimated with the PHOJET and COMPTON Monte Carlo simulations for the photoproduction and QED-Compton contributions, respectively. The integrated luminosity used in the measurement is denoted by $\mathcal{L}$ (see section 4.2). The remaining terms are the smeared acceptance ($\mathcal{A}$), the radiative corrections (RC), the bin centre corrections (BCC) and the 'smearing' correction ($\mathcal{C}_Y$). They are defined and discussed in the context of this analysis in the remainder of this chapter.

In the second binning scheme, the measurement is performed at fixed β and Q^2 in a large number of $x_{I\!\!P}$ (or equivalently x) bins. This permits the detailed investigation of the $x_{I\!\!P}$ dependence of the reduced cross-section, which is related to the differential cross-section by:

$$\sigma_r^{D(3)}(\beta, Q^2, x_{IP}) = \frac{\beta^2 Q^4}{4\pi\alpha^2(1 - y + \frac{y^2}{2})} \frac{\mathrm{d}^3\sigma_{ep \to eXY}}{\mathrm{d}Q^2\mathrm{d}x\mathrm{d}\beta}. \tag{5.3}$$

The procedure followed to determine the cross-section $\frac{\mathrm{d}^3\sigma_{ep \to eXY}}{\mathrm{d}Q^2\mathrm{d}x\mathrm{d}x_{IP}}$ is the same as for the

previous binning scheme after replacing the variable $x_{I\!P}$ by the x variable. The definition of the cross-section is incomplete without the precise specification of the kinematic range of the measurement. A study in [64] using the DIFFVM Monte Carlo for J/ψ production evaluated the efficiency for detecting the dissociated proton as a function of its mass, M_Y. Requiring elastic protons with $M_Y = m_p$ result in a large systematic error due to the failure of the forward detectors to reject proton dissociation events with low mass. As in [64], the cross-section measurement is performed here in the range $M_Y < 1.6$ GeV. The same study also concluded that it was not possible to detect elastic protons efficiently for values of $|t|$ larger than 1 GeV^2. The cross-section is therefore also integrated over the region $|t| < 1$ GeV^2. $\mathcal{C}_Y$ in equation 5.2 is an additional correction factor that accounts for migrations across the $M_Y = 1.6$ GeV and $|t| = 1$ GeV^2 boundaries. Its determination is explained in section 5.2.4.

5.2 Correction of the Data with the Monte Carlo Simulations

5.2.1 Acceptance Correction

The acceptance correction accounts for the migrations between bins due to the finite resolution of the reconstructed kinematics, the geometric acceptances and the inefficiencies of the sub-detectors used in the selection. Its calculation requires a Monte Carlo simulation of the physics under consideration that has undergone the same reconstruction procedure as the data. This correction is applied on a bin by bin basis and is defined by:

$$\mathcal{A} = N_{rec}/N_{gen}, \tag{5.4}$$

where N_{gen} is the number of (generated) Monte Carlo events that would be observed in each measurement bin in an ideal detector, whereas N_{rec} is the number of Monte Carlo (reconstructed) events that are reconstructed in that bin after passing through the detector simulation and selection criteria. N_{gen} and N_{rec} are computed with the RAPGAP, DJANGO and DIFFVM programs. The kinematic cuts of the selection (y, $\theta_{e'}$,...) are also imposed at the generator level, as the validity of the simulation beyond the phase space of measurement is not guaranteed [1]. The acceptance correction procedure relies on the very good simulation of both the physics and the detector which was demonstrated in section 4.15.

The description of the forward detector efficiencies were the only failure of the detector simulation that needed to be remedied. The remaining differences between data and Monte Carlo will be covered by systematics errors. The numbers N_{rec} and N_{gen} are not independent, since the majority of events that are reconstructed in a given bin are also generated in that bin. The number of generated events can be expressed as the sum of three terms:

$$N_{gen} = N_{stay} + N_{smearout} + N_{lost}, \qquad (5.5)$$

where N_{stay} is the number of events that are generated and reconstructed in the same bin and $N_{smearout}$ is the number of events that are reconstructed outside the bin in which they were generated. N_{lost} is the number of generated events that are not reconstructed inside the range of the binning used in the analysis. Similarly, N_{rec} can be expressed as:

$$N_{rec} = N_{stay} + N_{smearin}, \qquad (5.6)$$

where $N_{smearin}$ is the number of events that are generated outside the bin in which they are reconstructed. The acceptance can be re-expressed using equations 5.5 and 5.6, whose

[1]The effect of these cuts is corrected for in the bin centre corrections (see section 5.2.2).
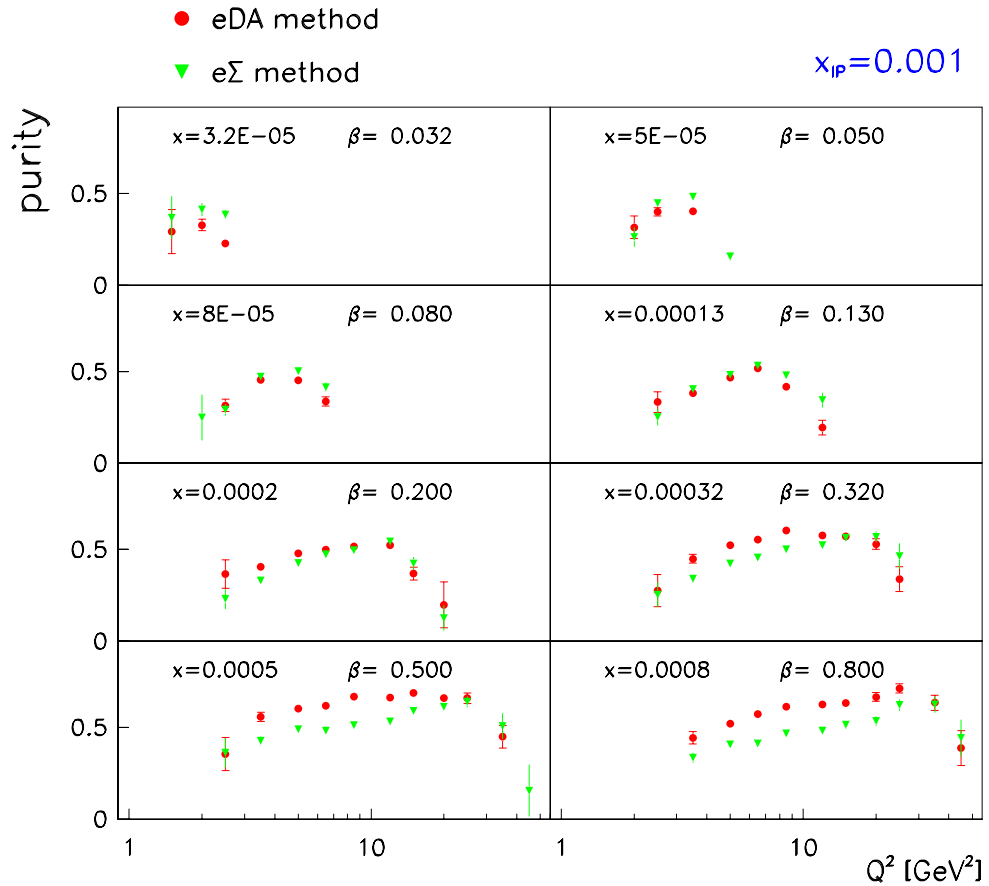
Figure 5.1: Comparison of the bin purities calculated with the eDA and eΣ kinematic reconstruction methods. The purities are plotted, for $x_{I\!P} = 0.001$, as a function of Q^2 in bins of x.

different terms are independent, and the calculation of the error on the acceptance therefore no longer necessitates the knowledge of the covariance matrix.

The quality of the binning can be assessed with the bin purity and stability given by:

$$\text{Purity} = \frac{N_{stay}}{N_{rec}} \qquad \text{and} \qquad (5.7)$$

$$\text{Stability} = \frac{N_{stay}}{N_{gen} - N_{lost}}. \qquad (5.8)$$

It follows that the acceptance can also be expressed as the ratio of the stability to the purity when the number of lost events, N_{lost}, is negligible. Thus, demanding both a high stability and purity guarantees a high acceptance. The purities and stabilities calculated
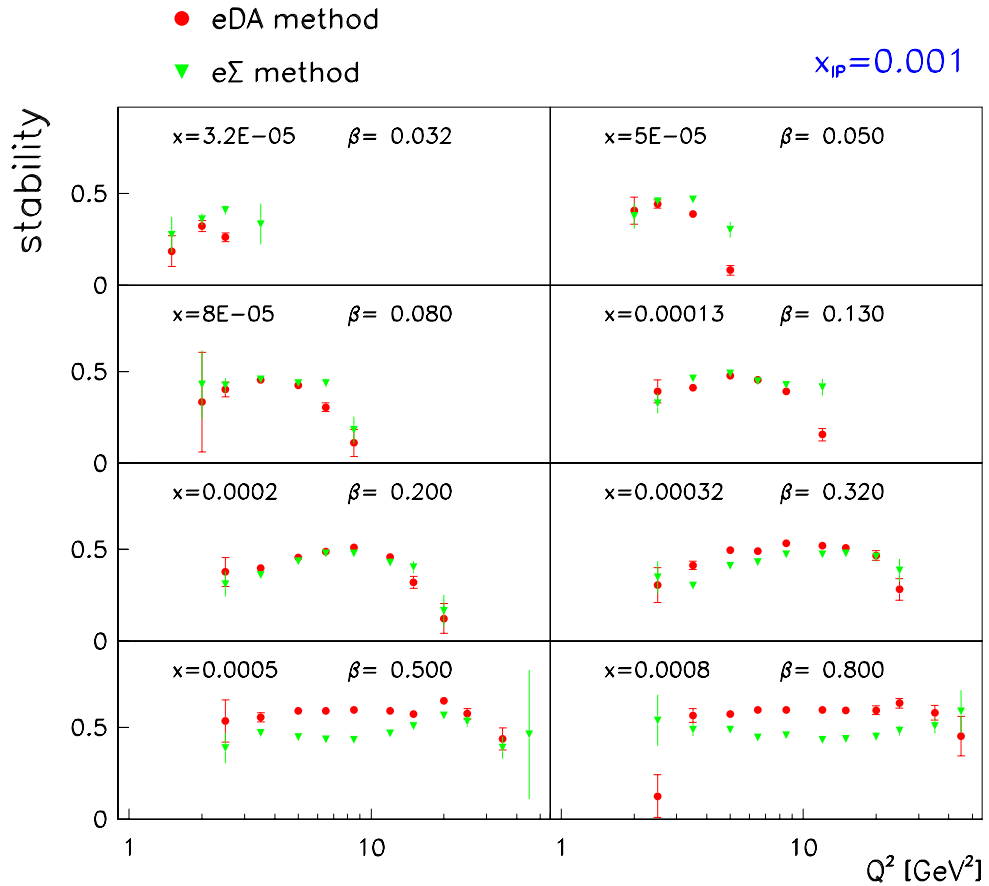
Figure 5.2: Comparison of the bin stabilities calculated with the eDA and eΣ kinematic reconstruction methods. The purities, plotted for $x_{I\!P} = 0.001$, are expressed as a function of Q^2 in bins of x.

with the eΣ and eDA kinematic reconstruction methods are shown in figures 5.1- 5.2, in bins of x, as a function Q^2 for $x_{I\!P} = 0.001$. The eDA reconstruction method presents equivalent or higher purities and stabilities than the $e\Sigma$ method over most of the phase space of the measurement. This is due to the superior resolution of the eDA method. However, the eΣ method is sometimes superior at the edge of phase space. The purities and the stabilities, with typical values of 40% in the $(x,Q^2,x_{I\!P})$ binning scheme, are required to be larger than 20% [2]. Since the limited Monte Carlo statistics gives rise to fluctuation, points with a lower purity and stability were not rejected if they were

---

[2]The values of the purity and stability cuts are the same as in the previous H1 publication on inclusive diffraction [50].

surrounded by bins with a purity greater than 20%.

5.2.2 Bin Centre Corrections

The bin centre correction adjusts the raw measurement, which corresponds to an average over the bin, to the value at the bin centre. From the conservation of the bin volume, the formula giving the bin centre correction can be easily derived:

$$BCC = \frac{\mathrm{d}^3\sigma}{\mathrm{d}Q^2\mathrm{d}x\mathrm{d}x_{I\!P}}\bigg|_{(Q_c^2,x_c,x_{I\!P}c)} \quad \frac{\Delta V}{\int_V \frac{\mathrm{d}^3\sigma}{\mathrm{d}Q^2\mathrm{d}x\mathrm{d}x_{I\!P}}\mathrm{d}Q^2\mathrm{d}x\mathrm{d}x_{I\!P}}. \tag{5.9}$$

The volume, V, of integration is delimited by the bin boundaries and the kinematic cuts defining the edge of the phase space. Thus, the calculation is performed over the same
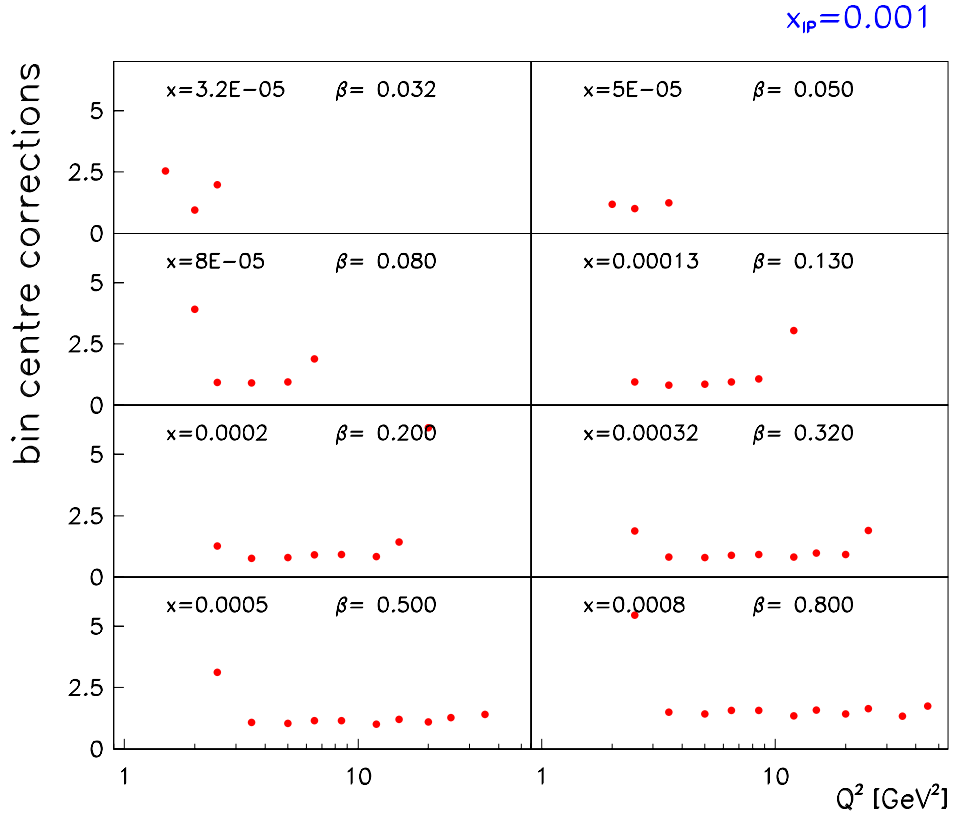
Figure 5.3: Bin centre corrections calculated with the QCD fit to the H1 data expressed as a function of Q^2 at $x_{I\!P} = 0.001$.

region of phase as for the acceptance The bin centre correction is evaluated with the QCD fits that lie at the heart of the RAPGAP Monte Carlo generator. The bin centres corrections are plotted in figure 5.3 as a function of Q^2 for $x_{I\!P} = 0.001$. It can be seen that the bin centre corrections become large at the limits of the phase space.

5.2.3 Radiative Corrections

Comparisons of the measurement with theory require that the measured cross-section is quoted at the Born level. The $E - p_z$ cut and the choice of the eDA reconstruction method for the kinematics restricts the QED radiative effects to manageable levels. However, the cross-section still needs to be corrected for the QED radiative processes discussed in section 4.8.

Two high statistics samples, with and without radiation, were generated with the RAP-GAP Monte Carlo. The HERACLES generator was interfaced to RAPGAP to model the simulation of initial and final state radiation and QED virtual loop corrections. The measurement was simulated for the case of an ideal detector using both samples and the bin dependent factor for the radiative corrections, RC, is given by the ratios of the cross-sections:

$$RC = \frac{\sigma_{Born}}{\sigma_{rad}}, \tag{5.10}$$

where σ_{Born} and σ_{rad} denote the cross-sections without and with QED radiation switched on. The radiative corrections are plotted as a function of Q^2 for $x_{I\!P} = 0.01$ in figure 5.4. They are approximately equal to unity over most of phase space. Larger corrections can be observed for the lowest values of Q^2. This trend is more pronounced for the highest values of $x_{I\!P}$, and hence the lowest y.
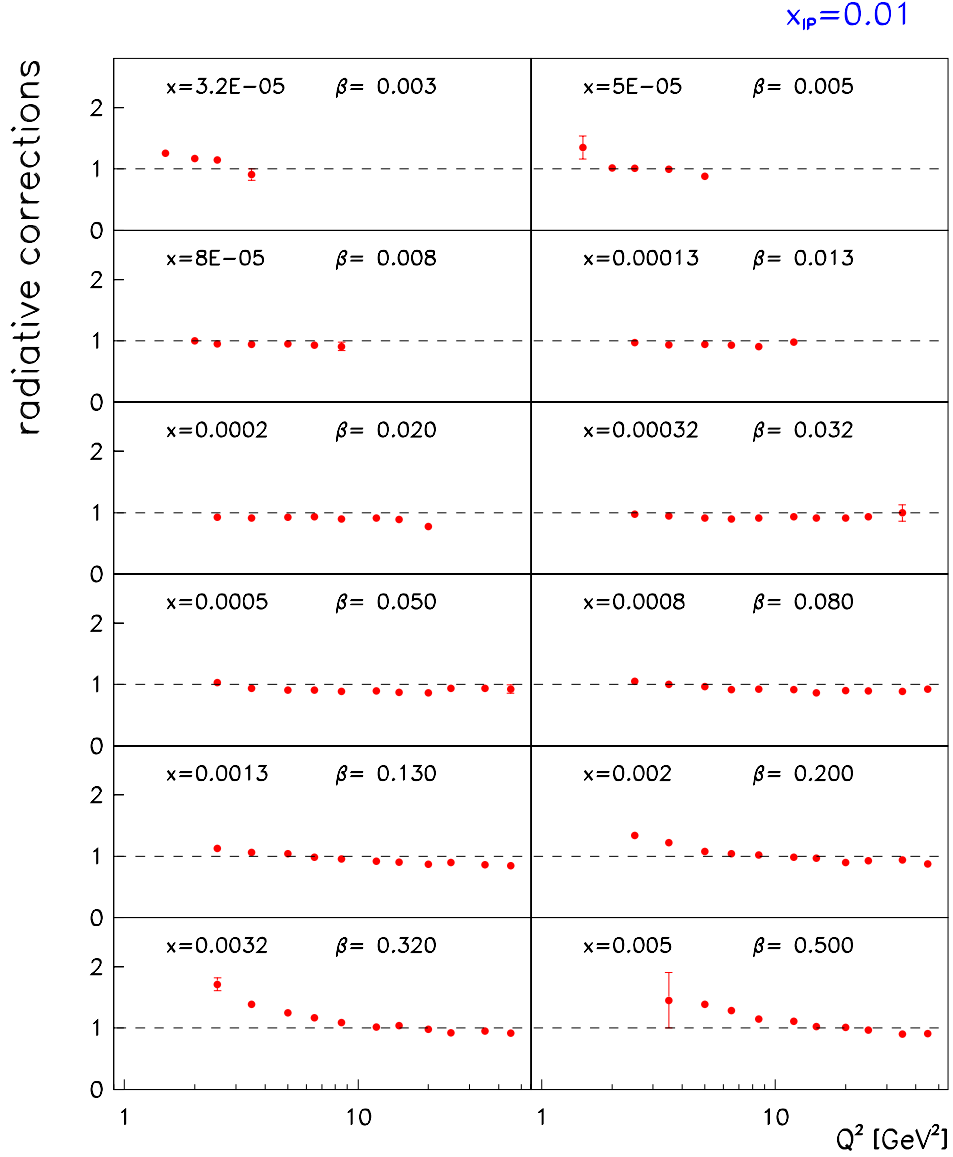
Figure 5.4: Radiative corrections calculated with the eDA method and the RAPGAP Monte Carlo generator shown as a function of Q^2 at $x_{I\!P} = 0.01$.

5.2.4 $\mathcal{C}_Y$ Correction

The smearing of events across the $M_Y = 1.6$ GeV and $|t| = 1$ GeV^2 boundaries is not accounted for by the acceptance due to the absence of a simulation for the region of phase space delimited by $1.6 < M_Y < 5$ GeV. The DIFFVM Monte Carlo generator (*c.f.* section 4.1) is used to remedy for this, since the simulation of both elastic proton

scattering and low mass proton dissociations are implemented in this program. The overall correction factor $\mathcal{C}_Y$ applied to the cross-section is obtained by first computing the net fraction F of events that migrate across the two boundaries using DIFFVM:

$$F = \frac{N_{smearout}^{pdis} - N_{smearin}^{pdis}}{N_{rec}^{pdiss} + R_{pdis}^{elas} N_{gen}^{elas}},\tag{5.11}$$

where

$$N_{smearout}^{pdis} = N_{smearout}^{pdis}(M_Y < 1.6 \text{ GeV AND } t < 1 \text{ GeV}^2 \text{ AND FAILED FWD. CUTS})\tag{5.12}$$

and

$$N_{smearin}^{pdis} = N_{smearin}^{pdis}(M_Y > 1.6 \text{ GeV OR } t > 1 \text{ GeV}^2 \text{ AND PASSED FWD. CUTS}).\tag{5.13}$$

Hence, $N_{smearout}^{pdis}$ and $N_{smearin}^{pdiss}$ are the numbers of proton dissociative events at the reconstructed level that have smeared across the boundaries $M_Y = 1.6$ GeV and $|t| = 1\text{GeV}^2$. The two terms, N_{gen}^{pdis} and N_{gen}^{elas}, in the denominator are the number of generated inelastic events in the region $M_Y < 1.6$ GeV and $|t| < 1\text{GeV}^2$ and the number of elastic events with $|t| < 1$ GeV^2, respectively. In [65], the diffractive J/ψ cross-sections with and without proton dissociation were found to be of similar magnitude [3] and the ratio of the cross-sections R_{pdis}^{elas} was assumed to equal unity in equation 5.11, in conformance with this result. The smearing correction is then given by:

$$\mathcal{C}_Y = 1 - F.\tag{5.14}$$

There are four contributions to the systematic error associated with $\mathcal{C}_Y$:

---

[3]The analysis of diffractive dissociation in photoproduction in [66] resulted in a similar ration. This was also confirmed in study of diffractive DIS in [61].

- The ratio R_{pdis}^{elas} between the non-elastic and elastic cross-sections was varied between 1:2 and 2:1 which gave rise to a systematic error of 0.6%.

- The generated M_Y^2 distribution in the proton dissociation Monte Carlo simulation was varied by $(\frac{1}{M_Y^2})^{\pm 0.3}$. This contributes 2.5% to the total systematic error.

- The slope parameter, b, in proton dissociation was varied by ± 1 GeV^{-2} according to the generated t-distribution e^{bt} giving an error of 0.1%.

- The systematic uncertainties arising from the efficiencies of the PRT and FTS (*c.f.* section 4.12) are estimated by first applying no re-calibration and then by decreasing the values of the correction factors by 100%. The resulting errors are 6.5% for the PRT and 1.6% for the FTS. The detection efficiency of the FMD was downgraded by 4% yielding a contribution of 0.2% to the total systematic error. Finally, a systematic error of 0.1% was obtained by varying the PLUG energy scale by 30%.

The correction factor with its statistical and an overall systematic errors is:

$$\mathcal{C}_Y = 1.012 \pm 0.004(\text{stat.}) \pm 0.075(\text{syst.}). \tag{5.15}$$

5.3 Systematic Errors

5.3.1 Detector Understanding:

Much effort was devoted to achieving the best understanding of the various detector components used in the analysis. However, there remain uncertainties in the detector calibrations and in the description of some detector efficiencies that lead to systematic errors. These were calculated on a bin by bin basis, but only the average percentage error is only quoted in what follows for the sake of clarity.

- *Hadronic Energy Scale:*

  A 4% uncertainty in the overall energy scale the LAr calorimeter led to an average uncertainty in the final measurement of $\sim 2\%$. The absolute SpaCal hadronic energy scale is known with a precision of 7% which resulted in a systematic error of $\sim 1.6\%$.

- *Energy carried by tracks:*

  The fraction of energy carried by tracks in the hadronic final state algorithm described in section 4.12 was varied by $\pm 3\%$. This translated into a systematic error of $\sim 1\%$.

- *Electromagnetic Energy Scale and Electron Angle*

  An error of $\sim 2.8\%$ arsises from the uncertainty of 1% in the energy scale of the electromagnetic part of the SpaCal. An uncertainty of 0.75 mrad was attributed to the possible misalignment of the SpaCal with respect to the BST. This led to an average systematic error of 2.6% on the final measurement.

- *Forward detectors:*

  The uncertainty in the PRT and FTS efficiencies is 25%, which propagates to an error of 1.2% for the PRT and 0.3% for the FTS.

  The efficiency of the forward muon detector was also deteriorated by 5% which gave rise to an error of 0.4%. Finally, the Plug calorimeter energy scale was varied by $\pm 30\%$. This contributed to an error of 0.6%.

5.3.2   Modelling Uncertainties

Imperfections in the Monte Carlo models used to correct the measurement for the detector acceptance, bin migrations and background suppression also give rise to systematic errors.

- *Kinematic distributions:*

  The shapes of the distributions in the diffractive kinematic variables were varied

beyond the limits imposed by previous measurements and the present data. The uncertainty in the $x_{I\!P}$ distribution was estimated by reweighting the distributions in RAPGAP by $(1/x_{I\!P})^{\pm 0.2}$ at the generated level. The variation propagated to an error of $\sim 2.1\%$ on the final measurement. Similarly the reweight of the β distribution by factors $\beta^{\pm 0.1}$ and $(1-\beta)^{\pm 0.1}$ resulted in uncertainties of $\sim 1.4\%$ and $\sim 0.4\%$, respectively. Finally, the t distribution was reweighted by $\pm e^{\pm 2t}$, which led to an uncertainty of $\sim 1.8\%$.

- *High $x_{I\!P}$ background:*

  To estimate the error arising from the contamination of the sample by events generated with DJANGO in the region $x_{I\!P} > 0.1$ or $M_Y > 5$ GeV, the number of DJANGO events was varied by $\pm 100\%$. This yielded an a 2.3% systematic effect.

- *Photoproduction background:*

  The uncertainty in the number of events entering the sample due to the photoproduction background was estimated by varying the PHOJET normalisation by $\pm 100\%$. This resulted in an uncertainty in the reduced cross-section measurement of $\sim 4\%$.

- *QED Compton background:*

  The uncertainty on background from QED Compton events was evaluated by varying the number of contributing events by $\pm 50\%$ which provided a systematic error of $\sim 2.5\%$.

- *Vector meson simulation:*

  The normalisation of the DIFFVM simulation was varied by $\pm 50\%$. An error of $\sim 1.1\%$ was obtained.

5.3.3 Uncorrelated Errors

The following uncertainties are applied in the form of a fixed percentage error which is uncorrelated between bins.

- *Trigger and BST efficiencies*

  The triggers used in this analysis were assumed to be 100% efficient and they were attributed a 1% error [61]. The agreement between data and simulation in the description of the BST efficiency was within 1% over most of the kinematic range of the measurement leading to an error with the same magnitude.

- *Bin-centre and radiative corrections:*

  The evaluation of the bin-centre and radiative corrections, described in sections 5.2.2 and 5.2.3 respectively, have a related systematic uncertainty of 3%.

5.3.4 Normalisation Uncertainties

The uncertainty in determining the luminosity leads to an overall normalisation error on all data points of 2%. The error in determining the noise corrections required for the forward detectors is 0.6%. The correction for migrations across the $M_Y = 1.6$ GeV and $|t| = 1$ GeV^2 measurement boundaries (*c.f.* section 5.2.4) also contributes to the normalisation uncertainty. This combined smearing error of 7.5% is the dominant systematic error in the measurement of the diffractive reduced cross-section. The total normalisation error is 7.5%.

5.4 Stability of the Measurement

5.4.1 Kinematic Reconstruction

After all corrections, the cross-section measurement should be independent of the kinematic reconstruction methods used when their range of applicability overlaps. The eDA reconstruction method gives the best resolution for diffractive studies. To test the sensitivity of the measurement to the choice of reconstruction method, it was also performed with the eΣ method, which is applicable to the entire range of the measurement. The normalised difference between the eDA and the eΣ method is defined by:

$$\text{norm. diff.} = (\sigma_r^D[eDA] - \sigma_r^D[e\Sigma])/\sqrt{\delta\sigma_r^D[eDA]^2 + \delta\sigma_r^D[e\Sigma]^2}, \qquad (5.16)$$

where $\delta\sigma_r^D$ represents the total error. Most points should be much better $|\text{norm. diff.}| \lesssim 1$ and points that fall well outside this range are considered unstable. The normalised difference is shown as a function of β for fixed $x_{I\!\!P} = 0.01$ in figure 5.6, where the horizontal dashed lines represent the limits imposed by the criteria adopted. The measurement is stable throughout the phase space. The strongest deviations observed in the plot can partly be accounted for by the poorer agreement between data and Monte Carlo in the control distributions for the kinematic variables obtained with eΣ method relative to the identical distributions using the eDA reconstruction (*c.f.* section 4.12).

5.4.2 Monte Carlo Generator

The extraction of the diffractive reduced cross-section with the SATRAP Monte Carlo generator provides an additional stability check of the measurement. This generator was originally used in [61] and in [56]. The SATRAP simulation failed to give a good description of the the y, β and $x_{I\!\!P}$ distributions that needed to be reweighted with high
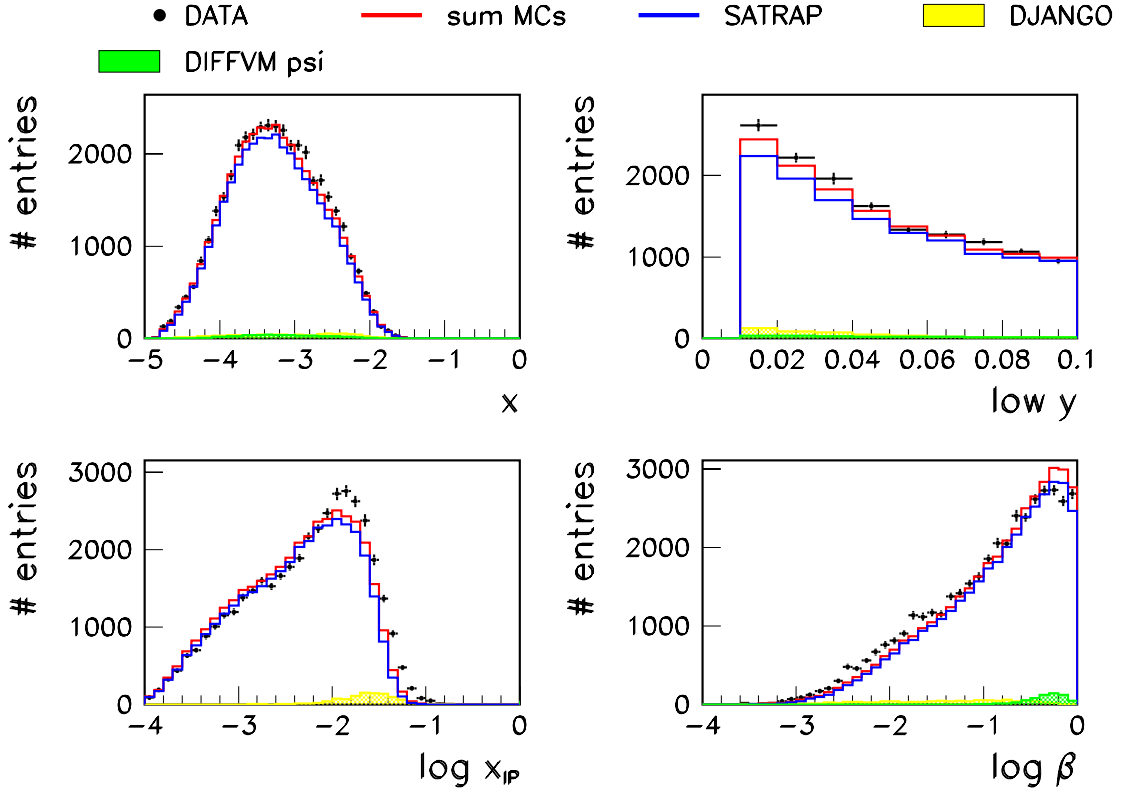
Figure 5.5: Control distributions for x, low y, $x_{I\!P}$ and β kinematic variables using the SATRAP Monte Carlo generator.

order polynomials at the generator level in order to describe the data (see [61]). The same reweight procedure was carried out including the new low y region and the measurement re-performed using SATRAP for the acceptance corrections. The agreement between the RAPGAP and SATRAP cross-sections is illustrated with the normalised difference introduced previously in figure 5.6 for $x_{I\!P} = 0.01$. Good agreement can be observed throughout the phase space. Kinematic control plots comparing the data with the reweighted SATRAP are shown in figure 5.5 for the x, y, $x_{I\!P}$ and β kinematic variables. RAPGAP gives a much better simulation. The validity of the saturation model is questionable at high $x_{I\!P}$ for quasi-elastic processes.
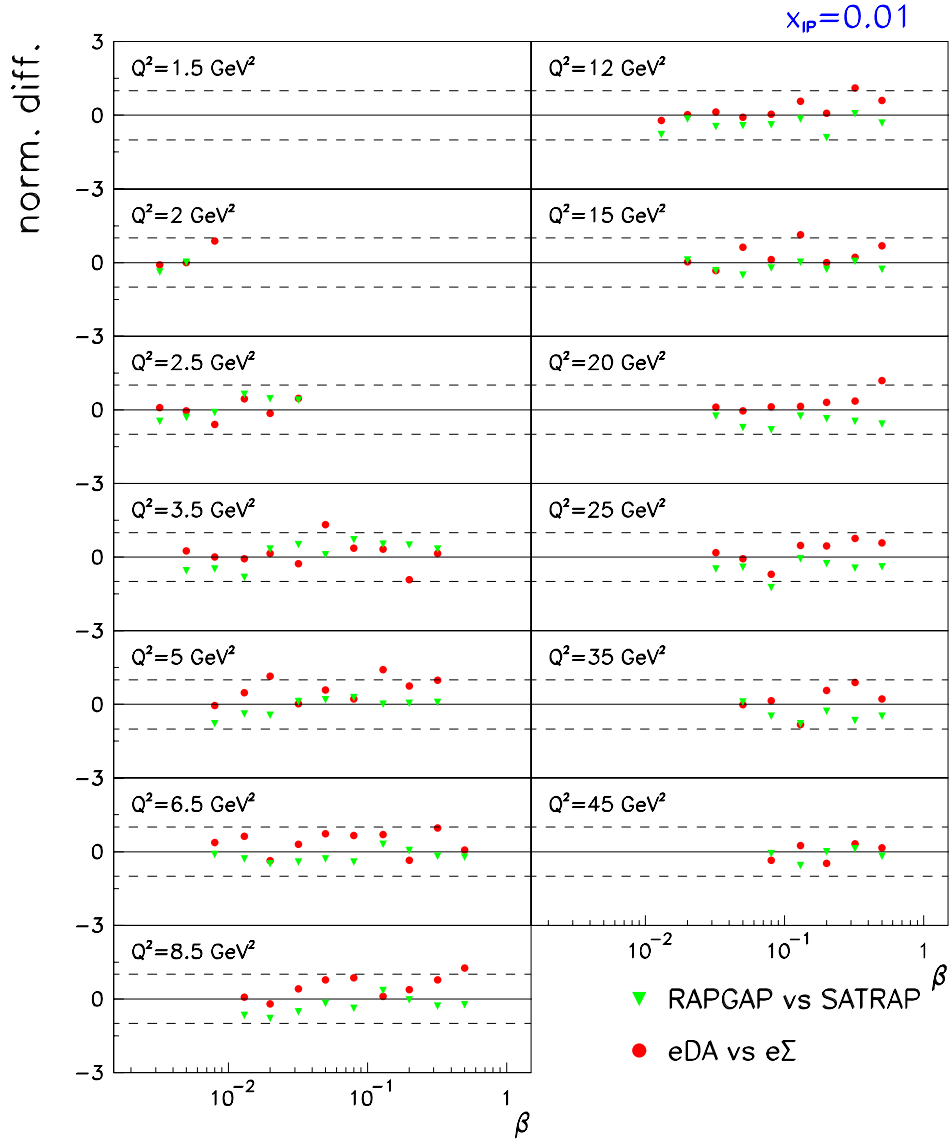
Figure 5.6: Normalised difference (see text) between the reduced cross-section measured with the eDA and eΣ reconstruction methods plotted as a function of β in bins of Q^2 at $x_{I\!P} = 0.01$. The difference between the cross-section measured with the RAPGAP and SATRAP Monte Carlo generators is also represented.

Chapter 6

Results and Discussion

In this chapter, the functional dependence on $x_{I\!\!P}$ of the low Q^2 diffractive reduced cross-section is studied using the measurement performed with the (Q^2, x, β) binning scheme [1] to investigate the $\gamma^* p$ centre of mass energy dependence of the diffractive exchange and to test the hypothesis that the $x_{I\!\!P}$ dependence factorises from the β and Q^2 dependences. The $(Q^2, x, x_{I\!\!P})$ binning scheme is used to investigate the β and Q^2 dependences of the cross-section in order to test its QCD evolution and study its scaling violations.

The results are compared with a preliminary measurement in the medium Q^2 range ($6.5 < Q^2 < 120$ GeV^2) by H1 [50] based on data collected in the year 1997 with an integrated luminosity of 10.6 pb^{-1}. The experimental procedures followed for the extraction of the cross-sections in these two analyses only differ in the detectors used for the electron measurement: the BST has been employed in the present work whereas the BDC was used in the medium Q^2 analysis. However, the different data taking periods lead to very different systematics, due for example to the different forward detector efficiencies. The preliminary high Q^2 H1 99-00 diffractive cross-section [67] extracted from the analysis of all data collected in the years 1999 and 2000 are also shown in some plots for completeness.

---

[1]See section 5.1 for the motivation for this scheme.

In the remainder of this chapter, the low, medium and high Q^2 measurements are identified with the H1 99, H1 97 and H1 99-00 labels, respectively. In the plots, the data points are drawn with inner statistical and outer total errors obtained by adding the systematic errors with the statistical errors in quadrature. The normalisation uncertainty of 7.5%, mainly due to the forward detector selection (see section 5.3.4), is not represented.

The low Q^2 results are also compared with the predictions derived from the NLO QCD fit performed on the medium Q^2 data. The H1 NLO fit is overlayed in all the plots: the solid curves correspond to the phase space covered by the points included in the fit and the dashed curves correspond to the fit predictions beyond this phase space. The widths of the curves indicate the combined experimental and theoretical uncertainties.

In each section of this chapter, only example plots are shown for clarity. Plots of the remaining data can be found in appendix A. In all the plots shown here and in the appendix, the diffractive reduced cross-section [2] is multiplied by $x_{I\!P}$ for presentation purposes in order to remove the approximate $1/x_{I\!P}$ dependence.

6.1 The $x_{I\!P}$ dependence of $\sigma_r^{D(3)}$

The phase space extension achieved in this analysis is best illustrated by the measurement performed in the (Q^2, x, β) binning scheme such that the data are plotted as a function of $x_{I\!P}$ in bins of fixed Q^2 and β. The result from this analysis (H1 99), the preliminary medium Q^2 (H1 97) and high Q^2 (H1 99-00) cross-sections are presented in figure 6.1. The minimally biased triggers of the 99MB data taking open up the low Q^2 region of phase space which now extends down to $Q^2 = 1.5$ GeV^2. The combined measurements span three orders in magnitude in Q^2 ranging from $Q^2 = 1.5$ GeV^2 up to $Q^2 = 1600$ GeV^2. The H1 99 cross-section is compared with the medium Q^2 data in figures 6.1 and A.1 (in the

---

[2]The term 'cross-section' is used interchangeably to designate the cross-section or the cross-section multiplied by $x_{I\!P}$ throughout this chapter.

appendix A) in their region of overlap ($6.5 < Q^2 < 45$ GeV^2). The data sets are in good agreement within the statistical and systematic uncertainties. In the large Q^2 part of the overlap region, the statistical errors of the H1 99 measurement are larger than those of H1 97 due to the lower luminosity, whereas at lower Q^2 the statistical errors are smaller for H1 99 due to the unprescaled triggers (see section 3.6.2). The H1 99 measurement extends to higher $x_{I\!P}$, with typically two new measurement bins at low β, in the comparison plot. This is a direct result of the improved vertex determination with the BST electron finder that allowed the measurement to be extended to lower y. The new low β and high $x_{I\!P}$ region of the measurement provides a small overlap in phase space with the measurement of the diffractive dijet production [68] performed by the CDF collaboration at Fermilab. In most of the phase space, the cross-section is observed to be approximately constant, or rises slowly with decreasing $x_{I\!P}$ at fixed β and Q^2. This behaviour is typical of the pomeron exchange observed in diffractive DIS and corresponds to a pomeron intercept $\alpha_{IP}(0) \sim 1.17$ [22], as used in the NLO QCD fit (see section 2.5). Although the NLO fit describes the data well throughout most of the phase space, the points at low β and high $x_{I\!P}$ lie significantly above the NLO fit predictions. This region of phase space is very sensitive to sub-leading exchanges. The relatively poor agreement of the fit with the H1 99 data suggests that a more sophisticated treatment of these exchanges is needed. When the H1 99 data gets included in the fits, the agreement is likely to improve.

6.2 The β dependence of $\sigma_r^{D(3)}$

It is interesting to study the β dependence of the cross-section to evaluate the extent of the validity of the QCD factorisation approach in diffractive DIS and to investigate the momentum distribution of the quarks in the diffractive exchange. The cross-section is shown for fixed Q^2 at an example $x_{I\!P} = 0.03$ from the $(Q^2, x, x_{I\!P})$ binning scheme in figure 6.2. Further results at $x_{I\!P} = 0.0003$, 0.001, 0.003 and 0.01 are shown in figures
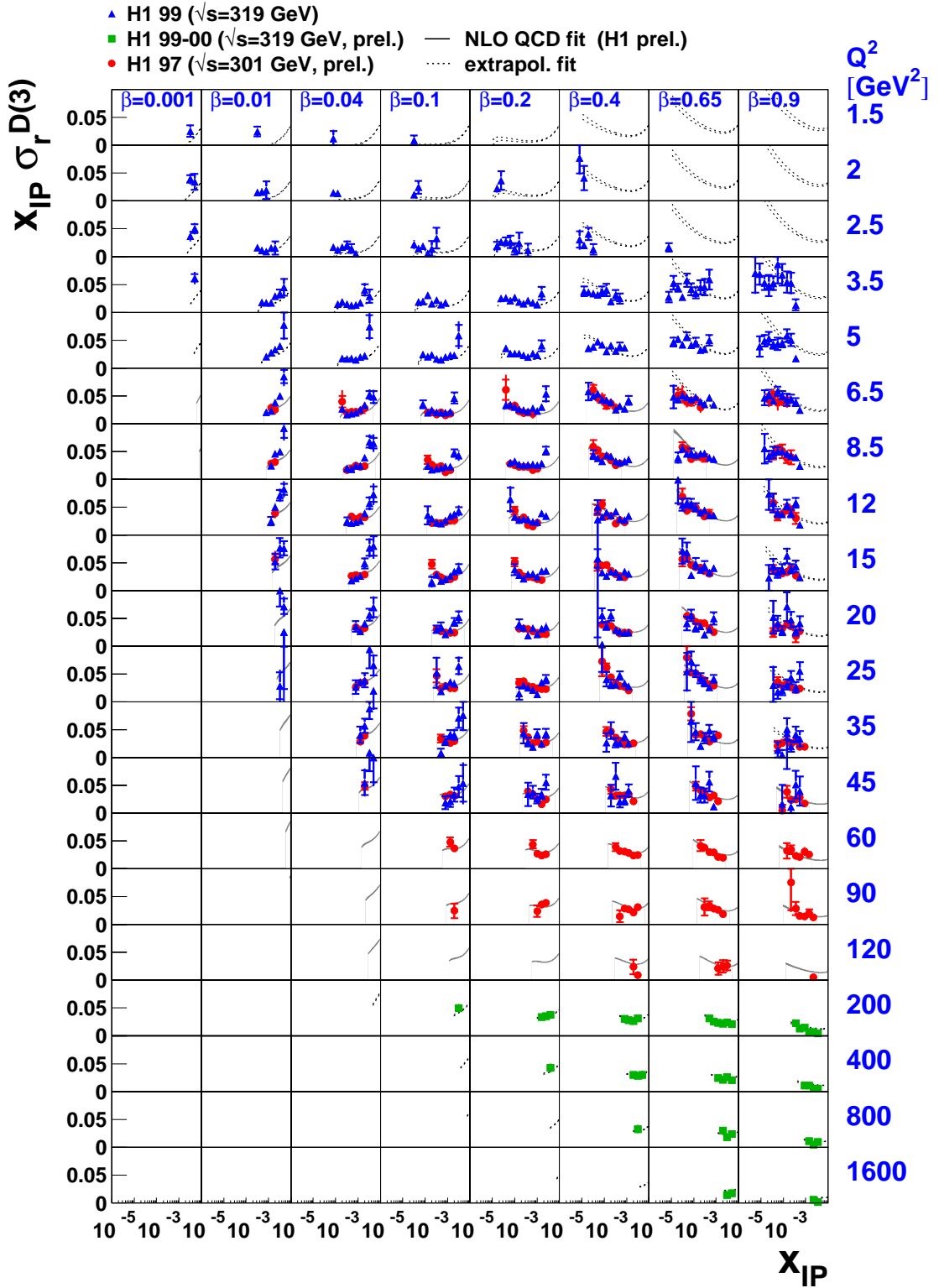
Figure 6.1: The diffractive reduced cross-section (H1 99) extracted from the 99MB data is plotted with the H1 preliminary medium Q^2 (H1 97) and high Q^2 (H1 99-00) data as a function of $x_{I\!P}$ for fixed values of β and Q^2. The prediction of the NLO QCD fit to the medium Q^2 data is also shown.

A.2-A.5 of the appendix A. Good agreement can be observed between the H1 99 and H1 97 measurements in their overlap region, which gives confidence in the newly extracted cross-section at low Q^2. The advantage of using the BST is visible in all $x_{I\!P}$ bins and is most noticeable at the highest value of $x_{I\!P}$, namely $x_{I\!P} = 0.03$ (see figure 6.2). In this bin, the low Q^2 measurement provides more data points than the H1 97 measurement for Q^2 up to 25 GeV^2. The cross-section rises with decreasing β most strongly at high $x_{I\!P}$, where the contribution of meson exchanges becomes significant.

There is good agreement between the data and the NLO fit for $Q^2 > 6.5$ GeV^2. The prediction of the backwards evolution in Q^2 describes the data relatively well down to $Q^2 = 3.5$ GeV^2 with the exception of the lowest $x_{I\!P}$ bin, where the data have a weaker dependence on β than the fit, and where higher twist terms in the pertubative expansion may become significant. At lower Q^2, future parton densities extracted from a NLO QCD fit including the new data could improve the agreement between the fit and the data, or the disagreement could be a manifestation of the breakdown of the DGLAP evolution formalism when the scale used in the calculations becomes too small or the parton densities become too large. The shape of the cross-section is closely related to that of the singlet parton densities expressed as a function of β (see figure 2.3).

6.3 The Q^2 dependence of $\sigma_r^{D(3)}$

The Q^2 dependence of the reduced cross-section provides some information on the scaling violations in diffractive DIS, and is thus indirectly sensitive to the diffractive gluon density. The cross-section is plotted for fixed β values at an example $x_{I\!P} = 0.003$ in figure 6.3. It is plotted at fixed β for the values $x_{I\!P} = 0.001, 0.01$ and 0.03 in figures A.6- A.9 of the appendix A. The data are characterised by positive scaling violation throughout most of the phase space. They only show negative scaling violation in the region $\beta \gtrsim 0.66$. This behaviour can be contrasted with the onset of the negative scaling violations in the
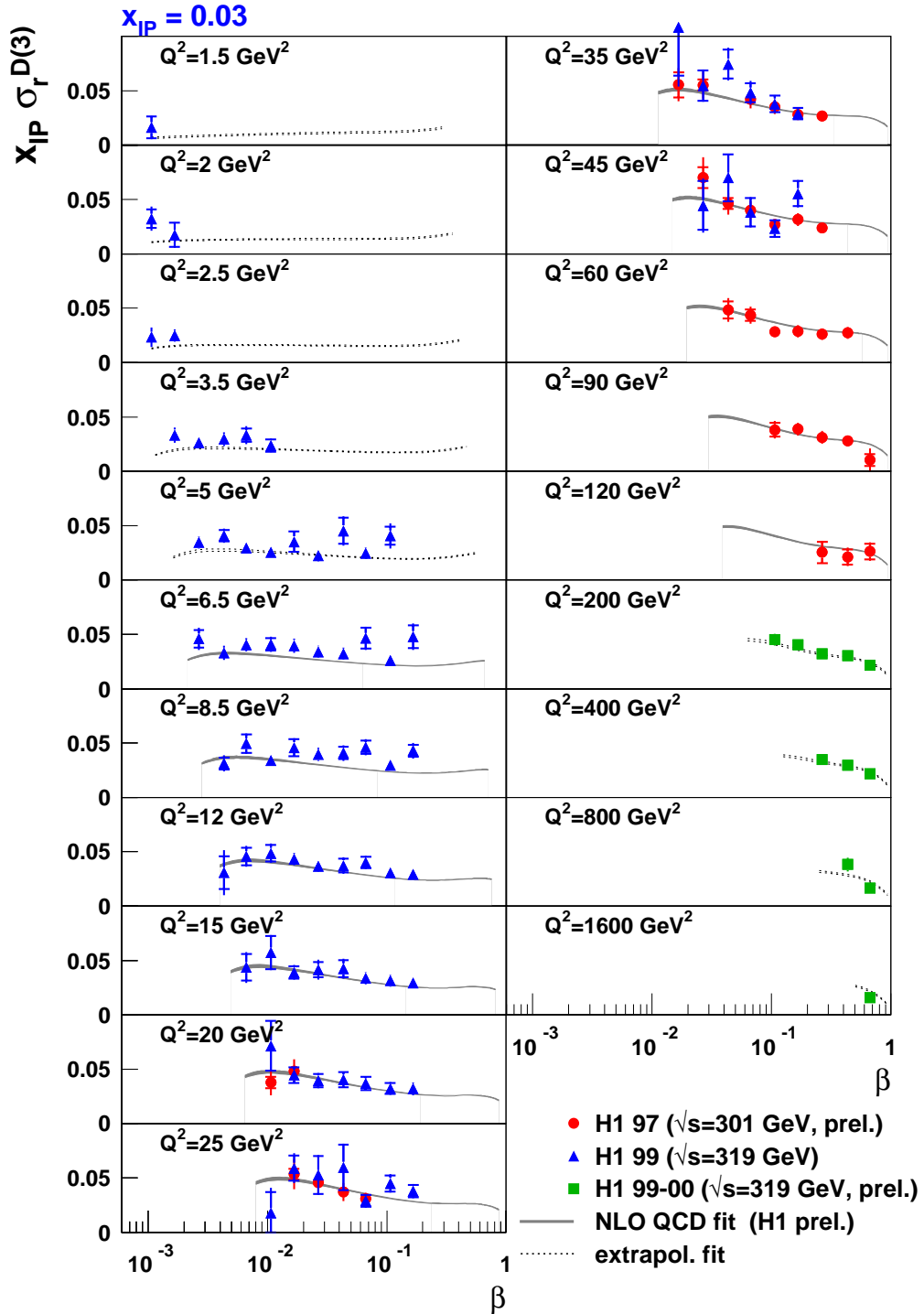
Figure 6.2: The diffractive reduced cross-section is shown as a function of β in bins of fixed Q^2 and fixed $x_{I\!P} = 0.03$. The measurement of this thesis (H1 99) and the H1 preliminary measurements at medium Q^2 (H1 97) and high Q^2 (H1 99-00) are also shown. The prediction of the NLO QCD fit to the 97 data is also represented in the plots.

inclusive data which starts at much lower x ($x = 0.1 - 0.2$) in figure 1.2. The large scaling deviations, in particular at low β, are attributed to the large gluon content of the diffractive exchange. The low Q^2 data will extend the range in Q^2 for the future NLO QCD fits, and hence will further constrain the diffractive gluon density.

6.4   Summary of the Results

The new measurement of the diffractive reduced cross-section at low Q^2 has extended the (low Q^2) phase space studied at H1 from $Q^2 = 6.5$ GeV^2 down to $Q^2 = 1.5$ GeV^2. Lower values of y ($y_{min} = 0.01$) have been reached than in previous analyses of inclusive diffraction, therefore providing extensions to the phase space at high $x_{I\!P}$. The data of this thesis are in good agreement with the preliminary H1 97 measurement within statistical and systematic errors in their overlap region ($6.5 < Q^2 < 45$GeV^2). The NLO QCD fit to the H1 97 data also results in a good description of the H1 99 data down to $Q^2 \sim 3.5$ GeV^2. At the lowest values Q^2, the fit fails to describe the data. Future fits including the new data could result in a better agreement, or the evolution equation framework could break down when the scale becomes too small to ensure the convergence of the pertubative calculations.

The data are consistent with a diffractive exchange characterised by a large gluon density extending to large fractional momenta and will help to constrain better future parton densities.

6.5   Future Prospects

It has been seen that the BST is a crucial detector in measuring the electron accurately at low Q^2. Due to problems associated with this detector, part of the 99MB data taking were
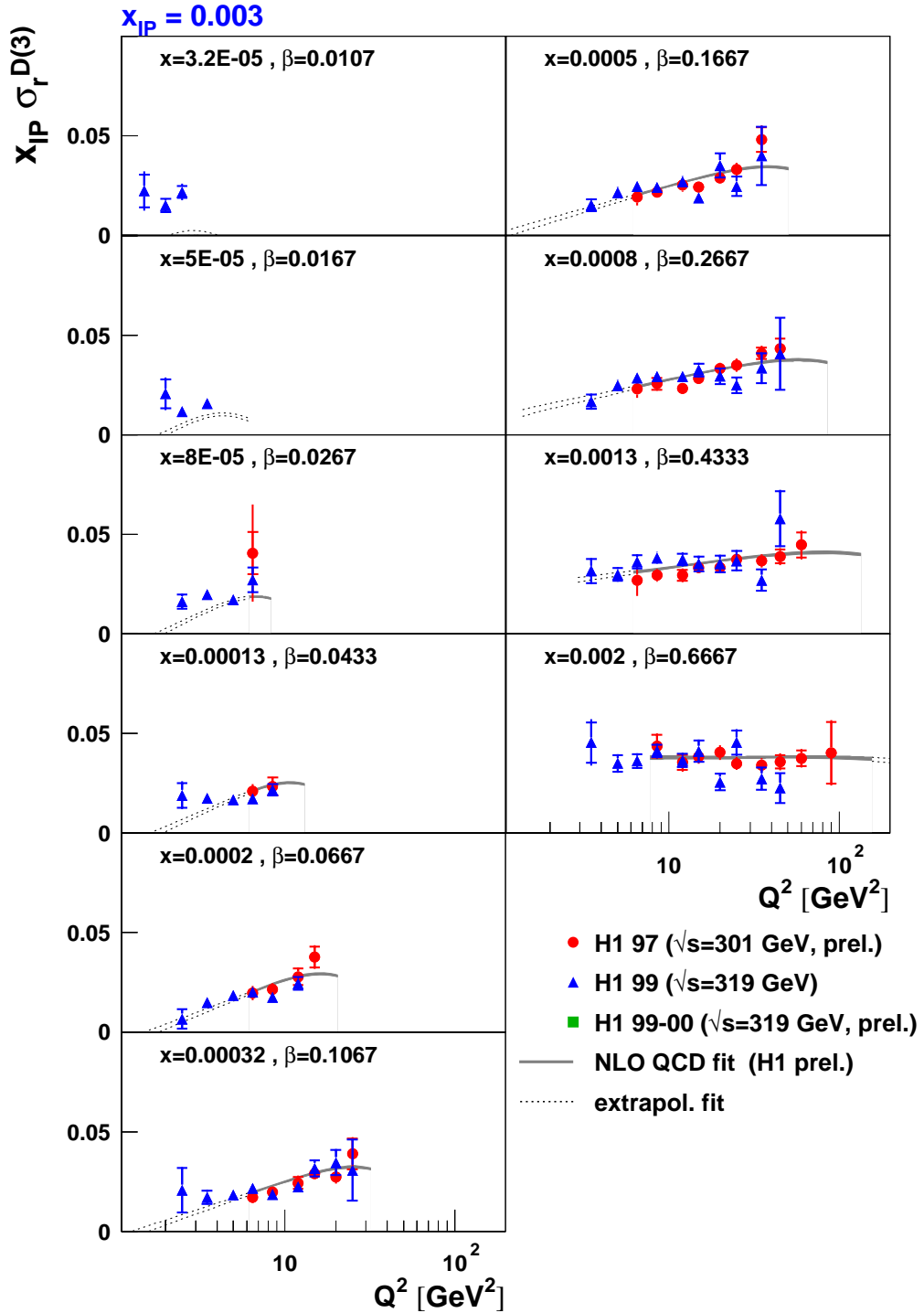
Figure 6.3: The diffractive reduced cross-section is shown as a function of Q^2 in bins of fixed β (x) and fixed $x_{I\!P} = 0.003$. The measurement of this thesis (H1 99) and the measurements at medium Q^2 (H1 97) and high Q^2 (H1 99-00) are also shown. The prediction of the NLO QCD fit to the 97 data is also drawn on the plots.

excluded from this analysis. This resulted in an integrated luminosity of 2.68 pb^{-1} instead of the full available 3.37 pb^{-1}. An extension of the analysis combining the information from the BST and the BDC would therefore yield higher statistics and a small improvement in the errors. A better description of the data by the simulation can be achieved, and hence a more accurate diffractive cross-section, by fitting all the available data and by using the new fits as a new input in the simulation. This would result in an improved agreement between data and the Monte Carlo for the diffractive kinematics variables, in particular at high $x_{I\!\!P}$. The measurement could then be extended to higher values of $x_{I\!\!P}$, in particular at low β, which would allow one to compare the diffractive cross-section with the CDF measurement [68] of diffractive dijet production. A better understanding of the forward detectors would help to reduce the largest contribution to the systematic error on the measurement, which is 7.5% arising from the $\mathcal{C}_Y$ correction (see section 5.2.4). A measurement of the proton-dissociation cross-section would help to test the hypothesis that the ratio of the elastic to the proton dissociation cross-section, assumed in the $\mathcal{C}_Y$ correction, is constant throughout the phase space in inclusive diffraction. These proton dissociation questions could be tackled by the comparison of data from the rapidity gap method with FPS data.

Summary

A new measurement of the diffractive reduced cross-section has been presented at low Q^2 in the kinematic region bounded by $1.5 < Q^2 < 45$ GeV^2. The H1 Backward Silicon Tracker was used for the first time in a diffractive measurement to precisely measure the electron and reconstruct the event vertex. As a result, lower values of y ($y_{min} = 0.01$) have been reached than in previous analyses of inclusive diffraction. This analysis therefore provides much improved kinematic coverage at high $x_{I\!P}$ where the contribution from 'sub-leading exchanges' to the cross-section is largest.

The inclusive data were shown to be well understood, and in particular great care was taken to align carefully the electron detectors. The good agreement between the data and the simulation was demonstrated before proceeding to the extraction of the diffractive reduced cross-section. All systematic effects were investigated. The acceptance correction was evaluated with two different Monte Carlo Simulations, namely RAPGAP and SATRAP, to investigate the uncertainty introduced by the model used to describe the previously unexplored regions of phase space. The cross-section was found be to stable and relatively insensitive to the underlying correction simulation. The insensitivity of the cross-section to the kinematic reconstruction method employed was also demonstrated. The data are consistent with previous H1 results on inclusive diffraction and are in good agreement with the predictions of an NLO QCD fit to the higher Q^2 data down to photon virtualities of around $Q^2 = 3.5$ GeV^2, which confirms the validity of the diffractive parton densities and the DGLAP evolution approach. However, the NLO fit shows some large

discrepancies at the edges of the phase space (low Q^2, low $x_{I\!P}$, high $x_{I\!P}$). New QCD fits including the new low Q^2 points will provide more accurate diffractive parton distribution functions or identify areas where the diffractive factorisation approach fails. The results of the extended QCD fits including the new data and the publication of the 97, 99 and 99-00 data sets and fit results are thus eagerly awaited.

Appendix A

Plots of the Reduced Diffractive Cross-Section

This appendix contains all the plots of the diffractive reduced cross-section not shown in chapter 6. The cross-section is plotted as function of $x_{I\!P}$ in figure A.1 in the region of overlap of the H1 99 and H1 97 measurements. The β and Q^2 functional dependences of the cross-section are shown in figures A.2-A.5 and figures A.6- A.9, respectively for various values of $x_{I\!P}$. The H1 NLO QCD fit prediction is also shown in every plot.
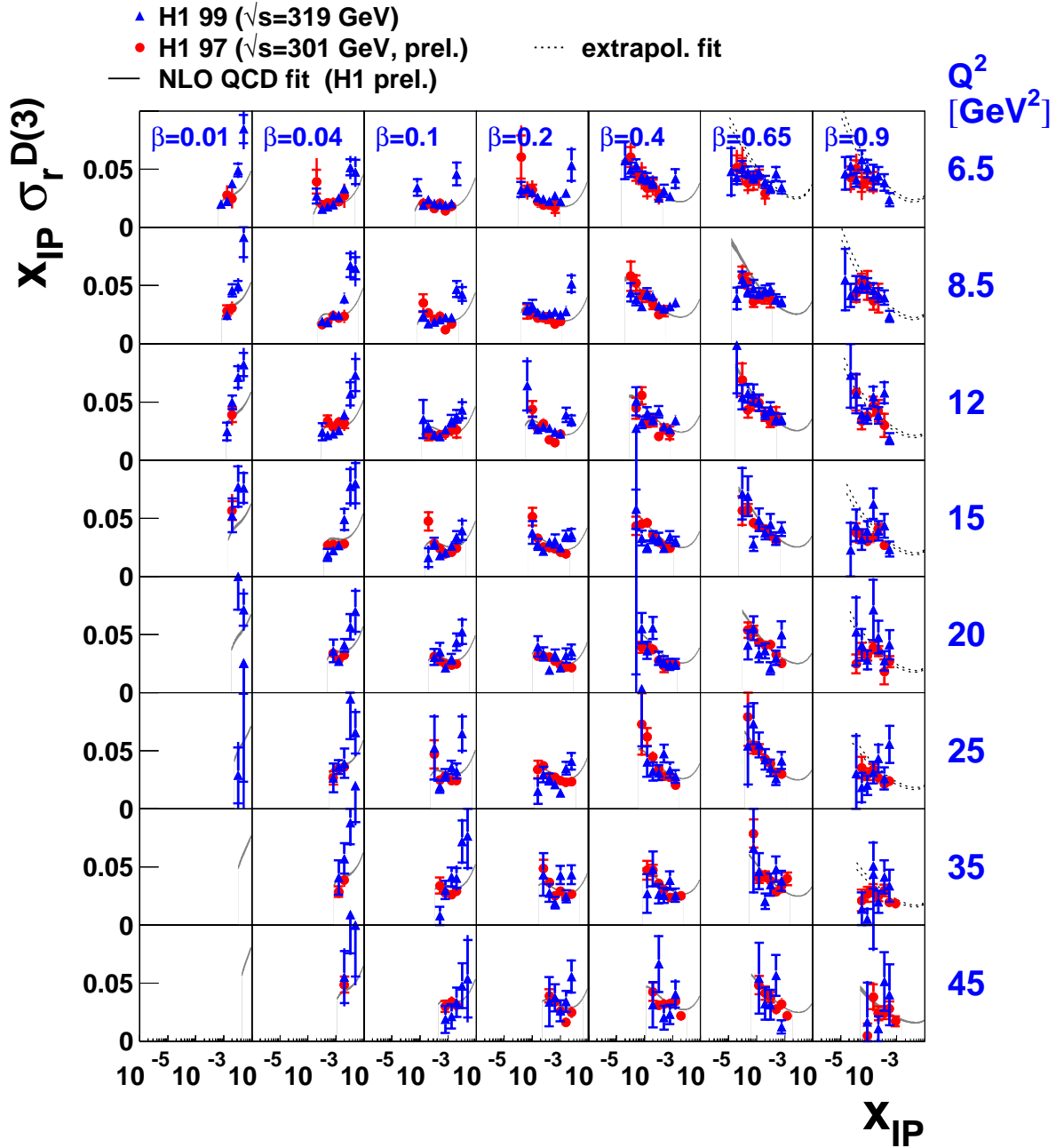
Figure A.1: Comparison of the diffractive reduced cross-section obtained in the analyses of the H1 97 and H1 99 data in the region of phase space ($6.5 < Q^2 < 45$ GeV^2) where they overlap. The $x_{I\!P}$ dependence of the cross-section is plotted at fixed Q^2 and $x_{I\!P}$.
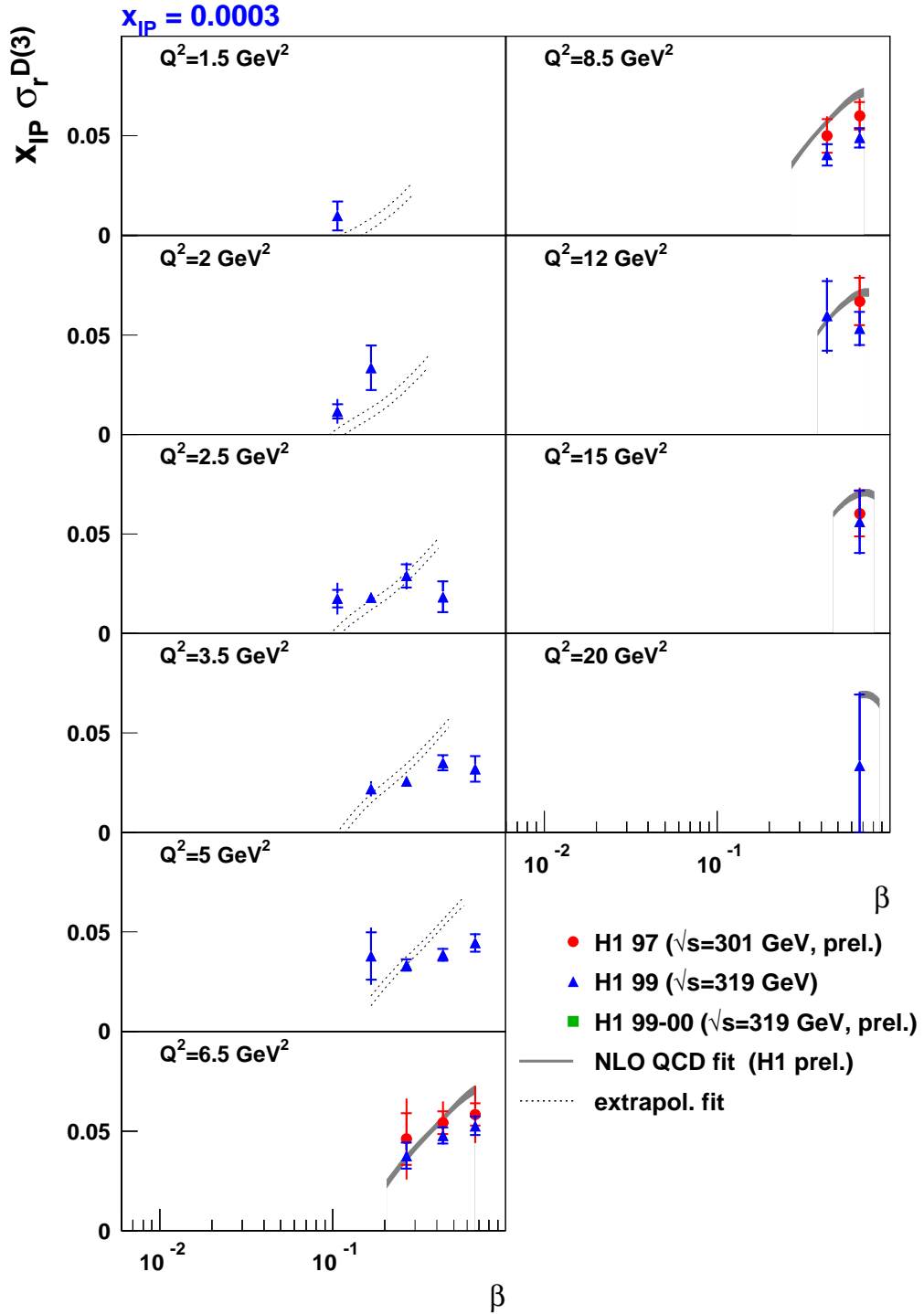
Figure A.2: The diffractive reduced cross-section measured in this thesis (H1 99) is shown as a function of β in bins of fixed Q^2 and fixed $x_{I\!P} = 0.0003$. The results of the H1 preliminary measurements at medium Q^2 and high Q^2 (H1 97 and H1 99-00) are also shown. The result of the NLO QCD fit to the 97 data is plotted.
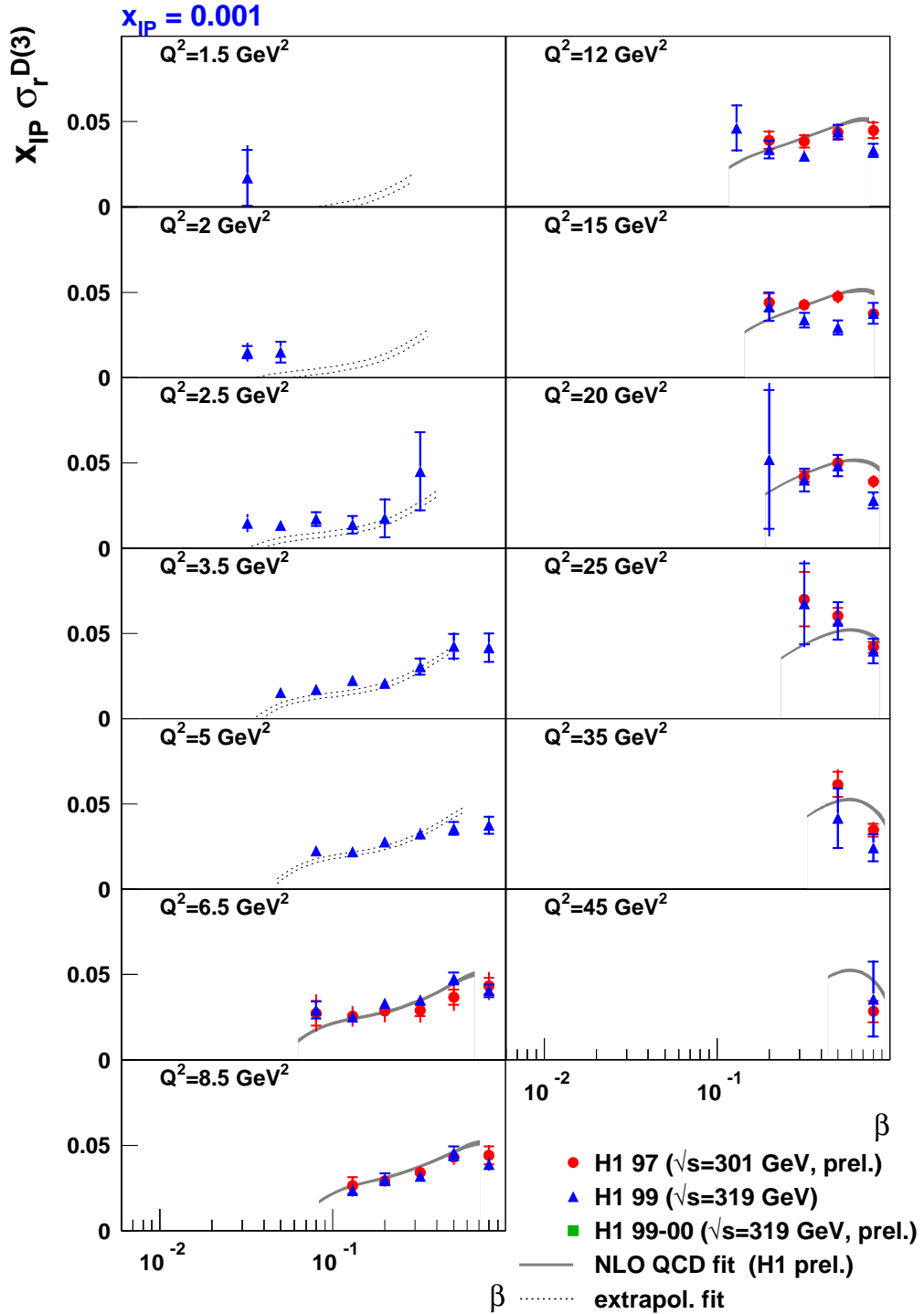
Figure A.3: The diffractive reduced cross-section (H1 99) measured in this thesis is shown as a function of β in bins of fixed Q^2 and fixed $x_{I\!P} = 0.001$. The results of the H1 preliminary measurements at medium Q^2 and high Q^2 (H1 97 and H1 99-00) are also shown. The prediction of the NLO QCD fit to the 97 data is plotted.

Figure A.4: The diffractive reduced cross-section measured in this thesis (H1 99) is shown as a function of β in bins of fixed Q^2 and fixed $x_{I\!P} = 0.003$. The results of the H1 preliminary measurements at medium Q^2 and high Q^2 (H1 97 and H1 99-00) are also shown. The prediction of the NLO QCD fit to the 97 data is plotted.

Figure A.5: The diffractive reduced cross-section measured in this thesis (H1 99) is shown as a function of β in bins of fixed Q^2 and fixed $x_{I\!\!P} = 0.01$. The result of the H1 preliminary measurements at medium Q^2 and high Q^2 (H1 97 and H1 99-00) are also shown. The prediction of the NLO QCD fit to the 97 data is plotted.
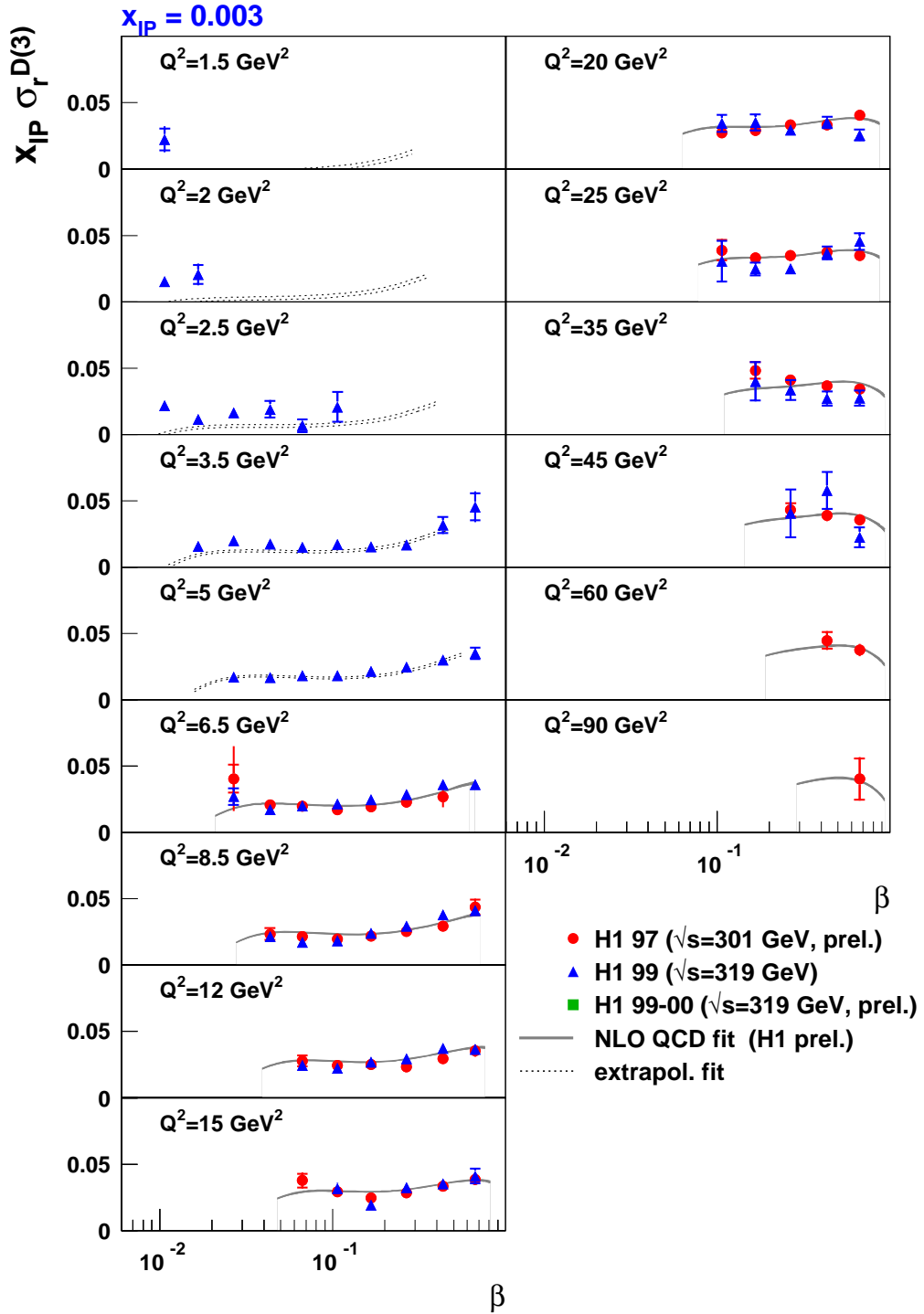
Figure A.6: The diffractive reduced cross-section measured in this thesis (H1 99) is shown as a function of Q^2 in bins of fixed β and fixed $x_{I\!P} = 0.0003$. The results of the H1 preliminary measurements at medium Q^2 and high Q^2 (H1 97 and H1 99-00) are also shown. The prediction of the NLO QCD fit to the 97 data is plotted.
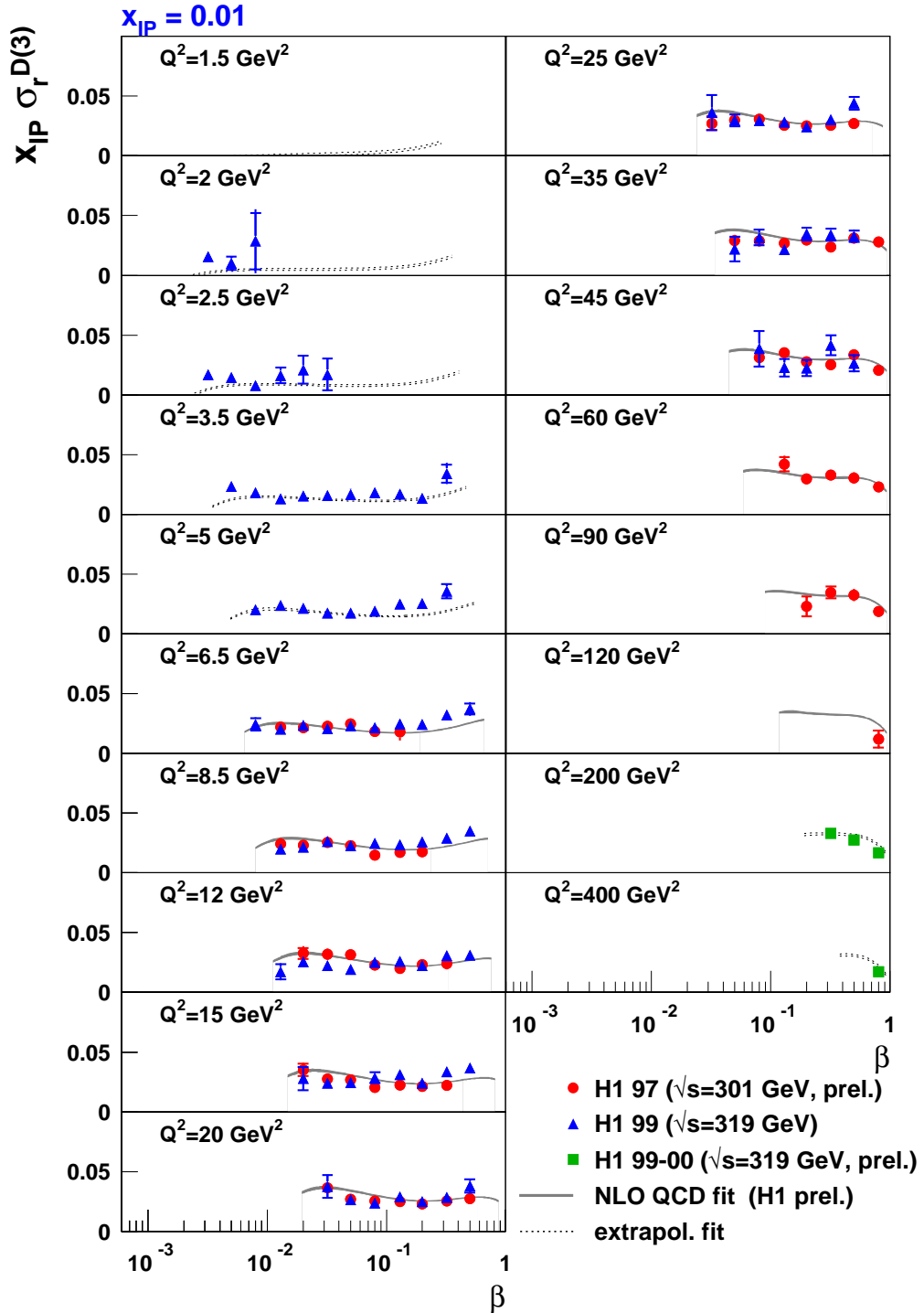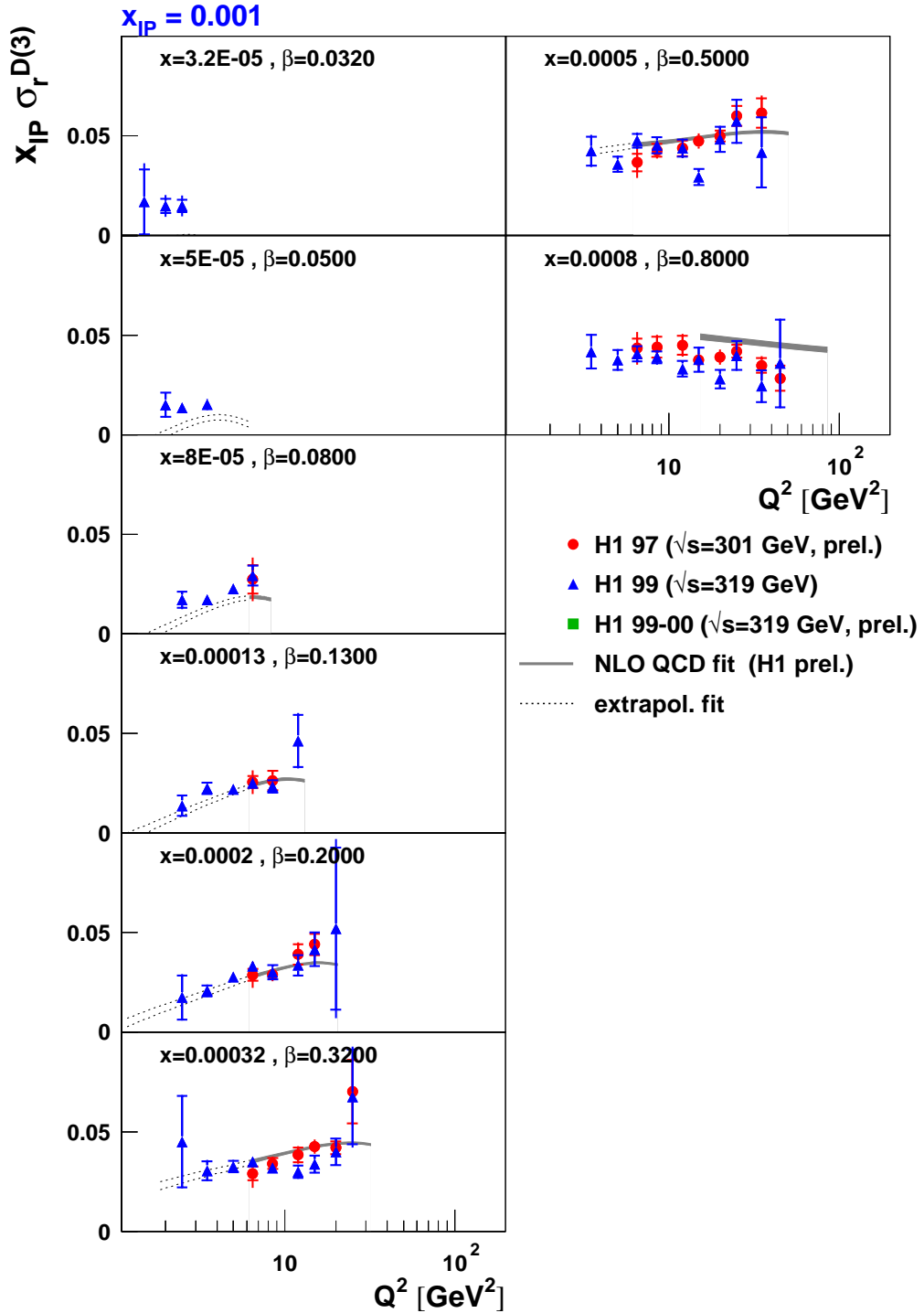
Figure A.7: The diffractive reduced cross-section measured in this thesis (H1 99) is shown as a function of Q^2 in bins of fixed β and fixed $x_{I\!P} = 0.001$. The results of the H1 preliminary measurements at medium Q^2 and high Q^2 (H1 97 and H1 99-00) are also shown. The prediction of the NLO QCD fit to the 97 data is plotted.
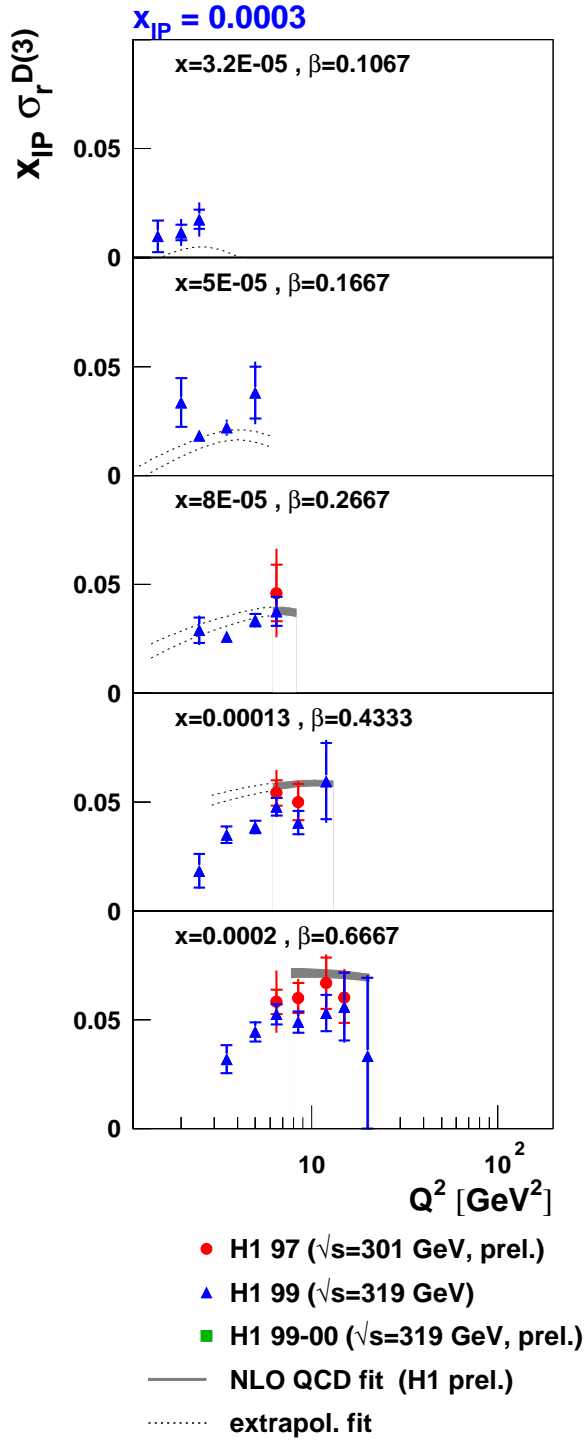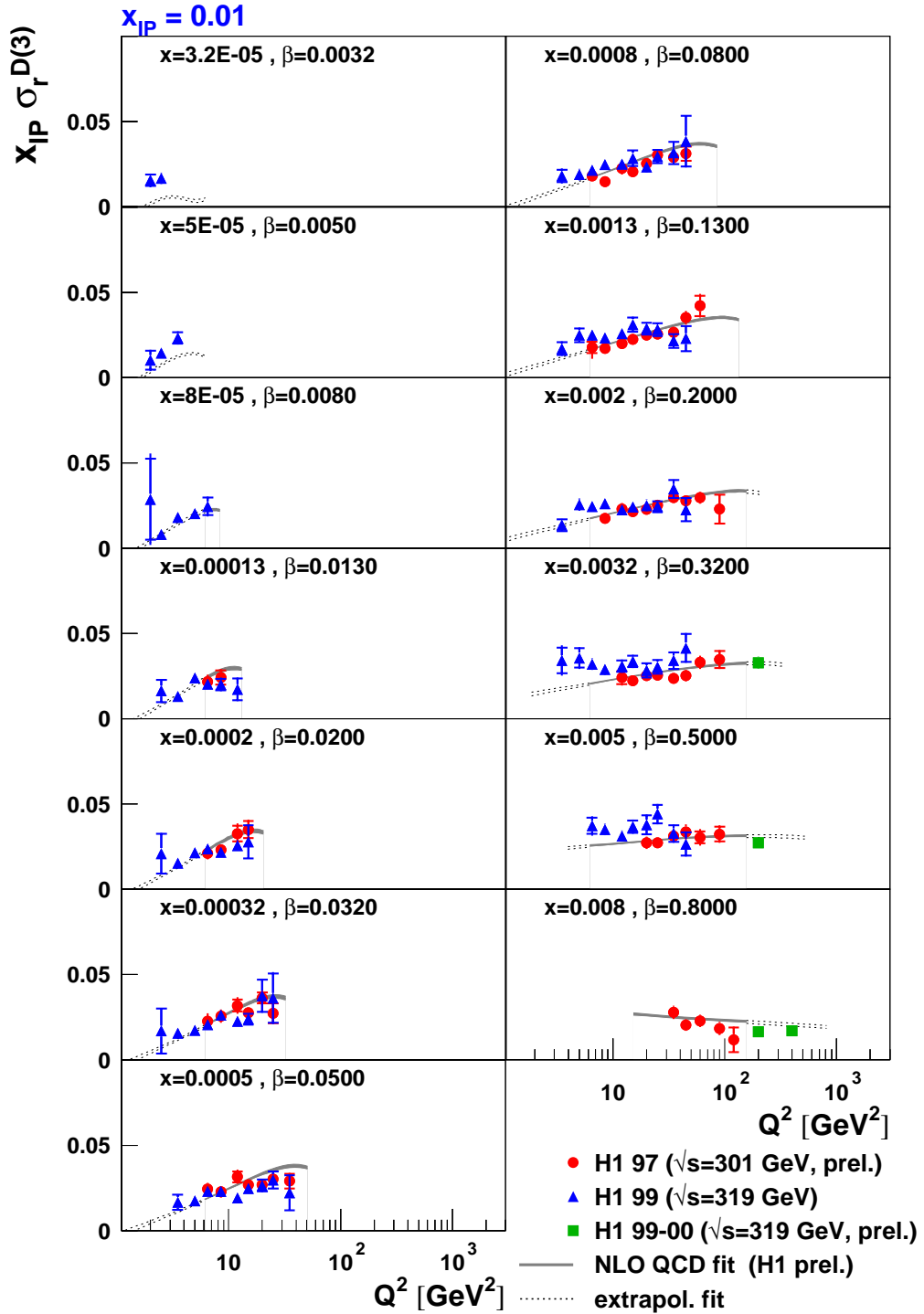
Figure A.8: The diffractive reduced cross-section measured in this thesis (H1 99) is shown as a function of Q^2 in bins of fixed β and fixed $x_{I\!P} = 0.01$. The results of the H1 preliminary measurements at medium Q^2 and high Q^2 (H1 97 and H1 99-00) are also shown. The prediction of the NLO QCD fit to the 97 data is plotted.

Figure A.9: The diffractive reduced cross-section measured in this thesis (H1 99) is shown as a function of Q^2 in bins of fixed β and fixed $x_{I\!P} = 0.03$. The results of the H1 preliminary measurements at medium Q^2 and high Q^2 (H1 97 and H1 99-00) are also shown. The prediction of the NLO QCD fit to the 97 data is plotted.
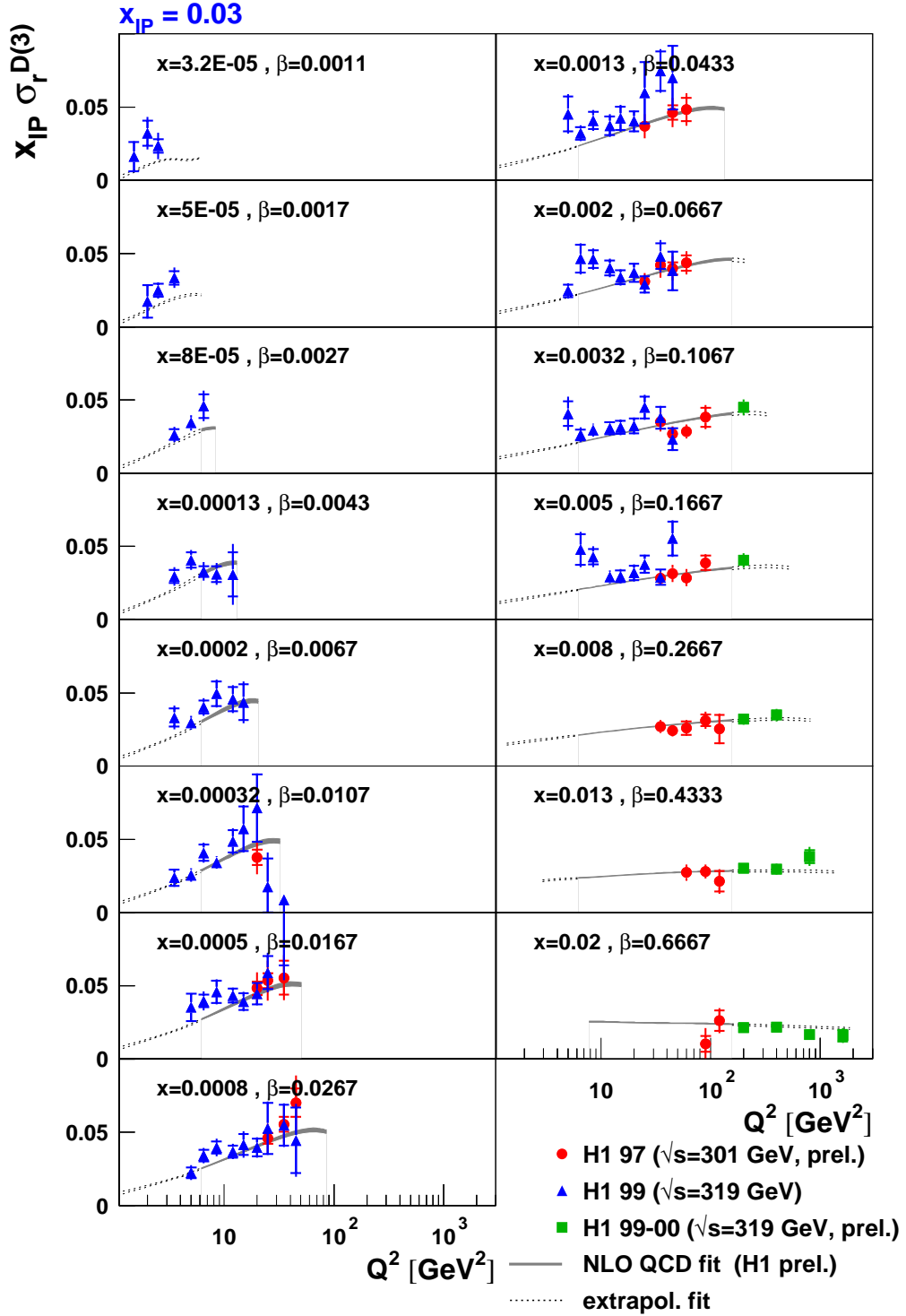
Bibliography

[1] Martin Breidenbach et al. Observed Behavior of Highly Inelastic Electron - Proton Scattering. *Phys. Rev. Lett.*, 23:935–939, 1969.

[2] Jerome I. Friedman and Henry W. Kendall. Deep Inelastic Electron Scattering. *Ann. Rev. Nucl. Part Sci.*, 22:203–254, 1972.

[3] K. Hagiwara et al. Review of Particle Physics. *Physical Review D*, 66:010001+, 2002.

[4] Richard P. Feynman. Very high-energy collisions of hadrons. *Phys. Rev. Lett.*, 23:1415–1417, 1969.

[5] J. D. Bjorken and Emmanuel A. Paschos. Inelastic electron proton and gamma proton scattering, and the structure of the nucleon. *Phys. Rev.*, 185:1975–1982, 1969.

[6] J. G. H. de Groot et al. Inclusive interactions of high-energy neutrinos and anti-neutrinos in iron. *Zeit. Phys.*, C1:143, 1979.

[7] R. Brock et al. Handbook of perturbative QCD. *Rev. Mod. Phys.*, 67:157–248, 1995.

[8] D.E. Soper J.C. Collins and G. Sterman. *Factorization Of Hard Processes In QCD.* World Scientific, 1989.

[9] Yuri L. Dokshitzer. Calculation of the Structure Functions for Deep Inelastic Scattering and e+ e- Annihilation by Perturbation Theory in Quantum Chromodynamics. (in Russian). *Sov. Phys. JETP*, 46:641–653, 1977.

[10] V. N. Gribov and L. N. Lipatov. e+ e- Pair Annihilation and Deep Inelastic e p Scattering in Perturbation Theory. *Yad. Fiz.*, 15:1218–1237, 1972.

[11] V. N. Gribov and L. N. Lipatov. Deep Inelastic e p Scattering in Perturbation Theory. *Yad. Fiz.*, 15:781–807, 1972.

[12] Guido Altarelli and G. Parisi. Asymptotic Freedom in Parton Language. *Nucl. Phys.*, B126:298, 1977.

[13] A. Vogt, S. Moch, and J. Vermaseren. The three-loop splitting functions in QCD. 2004. To appear in the proceedings of DIS 2004.

[14] C. Adloff et al. Measurement and QCD analysis of neutral and charged current cross sections at hera. *Eur. Phys. J.*, C30:1–32, 2003.

[15] C. Adloff et al. Forward jet and particle production at hera. *Nucl. Phys.*, B538:3–22, 1999.

[16] C. Adloff et al. Energy flow and rapidity gaps between jets in photoproduction at hera. *Eur. Phys. J.*, C24:517–527, 2002.

[17] A. Aktas et al. Diffractive photoproduction of J/ψ mesons with large momentum transfer at hera. *Phys. Lett.*, B568:205–218, 2003.

[18] A. Donnachie and P. V. Landshoff. Total Cross-Sections. *Phys. Lett.*, B296:227–232, 1992.

[19] John C. Collins. Proof of Factorization for Diffractive Hard Scattering. *Phys. Rev.*, D57:3051–3056, 1998.

[20] G. Ingelman and P. E. Schlein. Jet Structure in High Mass Diffractive Scattering. *Phys. Lett.*, B152:256, 1985.

[21] Konstantin Goulianos. Diffractive interactions of hadrons at high-energies. *Phys. Rept.*, 101:169, 1983.

[22] C. Adloff et al. Measurement and NLO DGLAP QCD Interpretation of Diffractive Deep-Inelastic Scattering at HERA. 2002. Submitted to 31st Intl. Conference on High Energy Physics, Amsterdam (ICHEP 2002), Abstract 980.

[23] C. Adloff et al. Inclusive Measurement of Diffractive Deep-Inelastic ep Scattering. *Z. Phys.*, C76:613–629, 1997.

[24] H1 Collaboration. Diffractive D^* Meson Production in DIS at HERA. August 2004. 32nd International Conference on High Energy Physics, Beijing (ICHEP04).

[25] H1 Collaboration. Dijets in Diffractive Photoproduction and Deep-Inelastic Scattering at HERA. August 2004. 32nd International Conference on High Energy Physics, Beijing (ICHEP04).

[26] K. Golec-Biernat and M. Wusthoff. Saturation effects in deep inelastic scattering at low Q^2 and its implications on diffraction. *Phys. Rev.*, D59:014017, 1999.

[27] C. Adloff et al. Measurement and QCD Analysis of Neutral and Charged Current Cross Sections at HERA. 2003. Submitted to Eur. Phys. J, 04/03.

[28] I. Abt et al. The Tracking, Calorimeter and Muon Detectors of the H1 Experiment at HERA. *Nucl. Instrum. Meth.*, A386:348–396, 1997.

[29] I. Abt et al. The H1 Detector at HERA. *Nucl. Instrum. Meth.*, A386:310–347, 1997.

[30] J. Burger et al. The Central Jet Chamber of the H1 Experiment. *Nucl. Instrum. Meth.*, A279:217–222, 1989.

[31] S. Egli et al. The Central Inner z Drift Chamber of the H1 Experiment. *Nucl. Instrum. Meth.*, A283:487–491, 1989.

[32] Jan Haack. Calibration of the Outer z Drift Chamber of the HERA H1 Experiment. DESY-ZEUTHEN-94-03.

[33] K. Muller et al. Construction and Performance of a Thin Cylindrical Multiwire Proportional Chamber with Cathode Pad Readout for the H1 Experiment. *Nucl. Instrum. Meth.*, A312:457–466, 1992.

[34] B. Schwab. Das Rückwärtsdriftkammersystem des H1 Experiments. H1 Thesis 6/96.

[35] N. Keller *et al.* Status of the BDC analysis. H1 Internal Note H1-IN-550(08/1998).

[36] W. Eick *et al. Nucl. Instrum. Meth.*, A386:81, 1997.

[37] B. Andrieu et al. The H1 Liquid Argon Calorimeter System. *Nucl. Instrum. Meth.*, A336:460–498, 1993.

[38] R. Appuhn et al. The H1 Lead/Scintillating-Fibre Calorimeter. *Nucl. Instrum. Meth.*, A386:397–408, 1997.

[39] R. Appuhn et al. Performance of an Electromagnetic Lead/Scintillating-Fibre Calorimeter for the H1 Detector. *Nucl. Instrum. Meth.*, A374:149–156, 1996.

[40] W. Hildesheim et al. The PLUG Calorimeter Users Guide. H1 Internal Note H1-IN-372(08/1994).

[41] P. Biddulph et al. The H1 Forward Muon Spectrometer. *Nucl. Instrum. Meth.*, A340:304–308, 1994.

[42] G. A. Schuler and H. Spiesberger. DJANGO: The Interface for the Event Generators HERACLES and LEPTO. In *Hamburg 1991, Proceedings, Physics at HERA, vol. 3* 1419-1432. (see High Energy Physics Index 30 (1992) No. 12988).

[43] A. Kwiatkowski, H. Spiesberger, and H. J. Mohring. HERACLES: An Event Generator for e p Interactions at HERA Energies Including Radiative Processes: Version 1.0. *Comp. Phys. Commun.*, 69:155–172, 1992.

[44] G. Ingelman, A. Edin, and J. Rathsman. LEPTO 6.5 - A Monte Carlo Generator for Deep Inelastic Lepton-Nucleon Scattering. *Comput. Phys. Commun.*, 101:108–134, 1997.

[45] Mats Bengtsson and Torbjorn Sjostrand. Parton showers in leptoproduction events. *Z. Phys.*, C37, 1988.

[46] Torbjorn Sjostrand. The Lund Monte Carlo for Jet Fragmentation and e+ e- Physics: JETSET Version 6.2. *Comput. Phys. Commun.*, 39:347–407, 1986.

[47] R. Engel. PHOJET Manual. University of Siegen preprint 95-05(1995, revised 1997).

[48] A. Courau and P. Kessler. QED Compton Scattering in High-Energy Electron - Proton Collisions. *Phys. Rev.*, D46:117–124, 1992.

[49] Hannes Jung. Hard Diffractive Scattering in High-Energy e p Collisions and the Monte Carlo Generation RAPGAP. *Comp. Phys. Commun.*, 86:147–161, 1995.

[50] H1 Collaboration. Measurement of the Diffractive Structure Function $F_2^{D(3)}$. International Europhysics Conference on High Energy Physics, EPS01, July 2001.

[51] Leif Lonnblad. Ariadne version 4: A program for simulation of qcd cascades implementing the color dipole model. *Comput. Phys. Commun.*, 71, 1992.

[52] B. List and A. Mastroberardino. DIFFVM: A Monte Carlo Generator for Diffractive Processes in *e p* Scattering. Prepared for Workshop on Monte Carlo Generators for HERA Physics (Plenary Starting Meeting), Hamburg, Germany, 27-30 Apr 1998.

[53] J. J. Sakurai. Ann. Phys. 11(1960), 1.

[54] D. Schildknecht J. J. Sakurai. Phys. Lett. B40(1972), 121.

[55] M. Greko. Nucl. Phys. B63(1973), 398.

[56] H1 Collaboration. Measurement of the Diffractive Deep Inelastic ScatteringCross-section at Low Q^2. International Europhysics Conference on High Energy Physics, EPS03, July 2003.

[57] Vladimir Arkadov. Measurement of the Deep-Inelastic ep Scattering ep Cross Section using the Backward Silicon Tracker at H1 Detector at HERA. H1 Thesis 10/00.

[58] Tomas Lastovicka. Private Communication.

[59] Emil Kalman, Rudolph. A new approach to linear filtering and prediction problems. *Transactions of the ASME–Journal of Basic Engineering*, 82(Series D):35–45, 1960.

[60] Doris Eckstein. Messung der Longitudinalen Strukturfunktion $F_L(x, Q^2)$ mit dem HERA-Experiment H1. DESY-THESIS-2002-00.

[61] Carrie-Anne Johnson. A Measurement of Diffractive Proton Structure Function $F_2^{D(3)}$ at Low Q^2 at the H1 Experiment at HERA. H1 Thesis 04/02.

[62] C. Adloff et al. Deep Inclusive ep Inelastic Scattering at Low x and Determination of α_s. *Eur. Phys. J.*, C21:33–61, 2001.

[63] Mikhail Kapichine. Measurement of Semi-Inclusive Diffractive Deep-Inelastic Scattering with a Leading Proton at HERA. July 2001. Proceedings of the 31st Intl. Conference on High Energy Physics, Amsterdam (ICHEP 2002).

[64] Paul Thompson. Open Charm Production in Inclusive and Diffractive Deep-Inelastic Scattering at HERA. H1 Thesis 06/99.

[65] S. Aid et al. Elastic and Inelastic Photoproduction of J/ψ Mesons at HERA. *Nucl. Phys. B*, 472:3–31, 1996.

[66] C. Adloff et al. Diffraction Dissociation in Photoproduction at HERA. *Z. Phys.*, C74:221–236, 1997.

[67] H1 Collaboration. Measurement of the Cross-section for Diffractive Deep Inelastic Scattering at High Q^2. International Conference on High Energy Physics, ICHEP04, August 2004.

[68] T. Affolder et al. Diffractive dijet production at $s^{1/2} = 630$-GeV and 1800-GeV at the Fermilab Tevatron. *Phys. Rev. Lett.*, 88:151802, 2002.